2016

Application of New Materials and Innovative Detailing for Reinforced Concrete Structures

Ishtiaque Ahmed Tuhin
South Dakota State University

APPLICATION OF NEW MATERIALS AND INNOVATIVE DETAILING FOR REINFORCED CONCRETE STRUCTURES

BY

ISHTIAQUE AHMED TUHIN

A thesis submitted in partial fulfillment of the requirements for the

Master of Science

Major in Civil Engineering

South Dakota State University

2016

APPLICATION OF NEW MATERIALS AND INNOVATIVE DETAILING FOR REINFORCED CONCRETE STRUCTURES

This thesis is approved as a creditable and independent investigation by a candidate for the Master of Science in Civil Engineering Degree and is acceptable for meeting the thesis requirements for this degree. Acceptance of this thesis does not imply that the conclusions reached by the candidates are necessarily the conclusions of the major department.

Mostafa Tazarv, Ph.D., P.E.
Thesis Advisor
Civil and Environmental Engineering Date

Nadim Wehbe, Ph.D., P.E.
Head
Civil and Environmental Engineering Date

Kinchel C. Doerner, Ph.D.
Dean, Graduate School Date

ACKNOWLEDGEMENTS

I would like to thank my fellow graduate research assistants Zachary Charles Carnahan, Lucas Michael Bohn, Abdullah Bakri Boudaqa, Michael James Mingo, and Abdullah Al Hashib for their assistance throughout this research. Advice and support of the J. Lohr Structures Lab Manager, Mr. Zachary Gutzmer, are highly appreciated.

I would like to recognize Dr. Mostafa Tazarv, who was my advisor for this research. I found this project, which he proposed to me, very interesting and challenging yet extremely rewarding. His valuable insight knowledge, help, and advice throughout the course of the project made the process a lot smoother. He was so helpful and always encouraged me to learn new things, which are unforgettable steps in my academic arena.

I am also very thankful to Dr. Nadim Wehbe, who was my academic advisor for more than a year. He secured my funding and allocated fund for my research. He gave us a lot of important instructions during our research. They, along with Dr. Allen Jones, Dr. Suzethe Burckhard, Dr. Mohammand Seyed Ardakani, and Dr. Junwon Seo have been superb instructors during my graduate studies at SDSU. I am also thankful to Zachery Gutzmer and Dr. Jonathan Wood to guide me during my TA duty at SDSU.

I would like to thank Steve Decker, Vice President of Business Development, LINE-X, LLC for donating material for my research. I also would like to thank Melissa Bommarito, Associated Steel Corporation for donating high strength steel shafts for my research.

Finally, I would like to thank my family members and friends for their unforgettable support and encouragement throughout my graduate study at SDSU.

TABLE OF CONTENTS

LIST OF FIGURES

LIST OF TABLES

ABSTRACT

APPLICATION OF NEW MATERIALS AND INNOVATIVE DETAILING FOR REINFORCED CONCRETE STRUCTURES

ISHTIAQUE AHMED TUHIN

2016

Confinement enhances mechanical properties of concrete sections specifically its strain capacity thus results is higher displacement capacity for reinforced concrete members. Even though the behavior of concrete confined with external jackets has been extensively investigated in previous studies, the use of rubber-based material as an external confinement is new, and was investigated for the first time in the present study. Thirty concrete cylinders were tested under uniaxial compression to investigate mechanical properties of rubber confined concrete. It was found that rubber does not increase the strength of confined concrete. However, the strain capacity of rubber confined concrete was more than 10%, equal to or higher than reinforcing steel bar tensile strain capacity. This unique property may make this type of confinement a viable retrofit or rehabilitation method to increase the ductility of low ductile members and structures in high seismic regions.

Repair of ductile components is often inevitable under strong earthquakes mainly because of concrete failure, significant yielding of reinforcement, or large residual lateral deformations. In this case, the structure needs to be demolished and reconstructed as the repair of reinforced concrete (RC) structures is complex when longitudinal reinforcement of ductile member fractures. External reinforcing bars are capable to increase energy dissipation of rocking columns and frames. Deformed

reinforcing steel bars without any reduction of the section enclosed in steel pipes was proposed as external energy dissipaters, entitled as buckling restrained reinforcement (BRR) in the present study. The test results showed that the compressive strain of BRR at the peak stress can exceed 5%, which will be sufficient in most practical cases since the strain of compressive reinforcement in a concrete section is usually controlled by the core concrete strains.

Experimental and analytical investigations were carried out on RC beam-column specimen under cyclic loading. A nine-story RC building was analyzed and designed as special moment resisting frame (SMRF). A half-scale exterior beam-column joint of the first floor of the prototype frame was tested to investigate the seismic behavior of the specimen. The test result showed that the column longitudinal and transverse reinforcement did not yield under the cyclic loading and the damage of column was insignificant. Almost all cracks were formed in the beam and more cracks were observed after drift ratio of 1.46%. The beam longitudinal reinforcing bars yielded then fractured at a high drift ratio (3.5%). The beam-column specimen showed 75% higher lateral drift capacity than the ASCE allowable drift ratio, which was 2% for this building. The test results confirmed that the modern seismic design codes ensure large displacement capacities for SMRF without any premature failure.

CHAPTER 1. INTRODUCTION

Experimental and analytical studies on three different topics were carried out in the present study to investigate the feasibility of new materials and innovative detailing for reinforced concrete structures to improve their seismic performance. A brief description of the topics covered in this study and the objectives are discussed herein.

1.1. Project Description

1.1.1. Rubber Confined Concrete

Confinement enhances mechanical properties of concrete specifically its strain capacity thus results is higher ductility for confined sections. Mechanical properties of conventional concrete confined with a rubber-based material were investigated in this study. Eighteen conventional concrete cylinders were rubber at the age of 28 days. Rubber coating of a concrete sample includes three steps: (1) cleaning the surface of concrete samples, (2) spraying a prime coat and allowing 12 hours of curing, and (3) spraying the rubber at different thickness. Ready mix concrete target strength of 5000 psi at 28 days was used in this experimental study. All specimens were tested under uniaxial compressive load to investigate the mechanical properties and to establish stress-strain relationship of rubber confined concrete.

1.1.2. Buckling Restrained Reinforcement

Reinforced concrete (RC) bridges and buildings are currently designed to exhibit large displacement capacities during earthquake excitation through yielding of reinforcement. External reinforcing bars have been used in previous studies to increase energy dissipation of rocking columns and frames. With some modification, this might be used as longitudinal reinforcement of RC sections thus RC structures can be repaired in a few hours after an event without the need of total replacement of the structure. Feasibility and performance of a new type of external energy dissipater, which is referred to as "buckling restrained reinforcement (BRR)" was investigated in this study. A series of BRR specimens were constructed and tested under monotonic and cyclic axial compressive loading to failure. Two different sizes of deformed steel bars, No. 4 and No. 8, were used in this experimental investigation. Steel tubes with different geometry were used to prevent buckling of reinforcement and were filled with non-shrink grout.

1.1.3. Behavior of Modern Beam-Column Connection

Several studies have investigated the seismic performance of moment resisting frames (SMRF). However, none of these studies successfully included the actual boundary conditions in their experimental setup. Furthermore, experimental data on the performance of SMRFs designed with current codes is limited.

A nine-story SMRF RC building located in a high seismic region (Los Angeles, US) was designed following current codes. One exterior beam-column joint of the first floor of the building was selected to investigate the seismic performance of the joint in through experiment. A new setup was designed to include the actual

boundary condition, which allows both columns and beams to sway. The half-scale beam-column specimen was tested to failure under simulated earthquake cyclic loading.

1.2. Research Objectives and Scopes

1.2.1. Rubber Confined Concrete

The main goal of this study was to investigate the stress-strain behavior of conventional concrete confined with a new rubber-based material. Stress-strain relationship was established for this type of confinement to be used in the repair, retrofit, or rehabilitation of low-ductile or substandard bridge columns.

1.2.2. Buckling Restrained Reinforcement

The main objective of this study was to experimentally investigate the feasibility and performance of conventional reinforcing steel bars as an external energy dissipater instead of dog-bone mild steel or aluminum bars. The application of conventional reinforcement as external energy dissipater will save time and money compared to dog-bone energy dissipaters due to machining.

1.2.3. Behavior of Modern Beam-Column Connection

The main goal of this experimental study was to (1) simulate the actual boundary conditions of beam-column specimens in experiments, and (2) investigate the seismic performance of special moment-resisting beam-column joints designed based on the current codes.

1.3. Document Organization

This study included multiple experimental and analytical studies to assess the feasibility of new materials or detailing for reinforced concrete buildings and bridges subjected to seismic loading. The thesis includes six chapters. Chapter 1 presents a brief description of the work done and the scope of each study. Chapter 2 presents the experimental investigation of rubber confined concrete to observe their mechanical properties and stress-strain relationship. Chapter 3 presents experimental investigation of external energy dissipaters to observe their compressive behavior and anti-buckling efficiency. Chapter 4 presents the experimental results of external beam-column connection, which was selected from analyzed nine story reinforced concrete building. Chapter 5 presents the OpenSees model of conventional steel confined prototype bridge column provides rubber as external jacket. Also presents the OpenSees model of exterior beam-column connection. Chapter 6 presents the exclusive conclusions of behavior of rubber confined concrete, buckling restrained reinforcement, and external beam-column joint.

CHAPTER 2. RUBBER CONFINED CONCRETE

2.1. Introduction

Concrete can be confined by using transverse reinforcement inside the section or external jacketing usually made of concrete, steel, or fiber reinforced polymer (FRP). Confinement enhances mechanical properties of concrete specifically its strain capacity thus results is higher ductility for confined sections. Mechanical properties of conventional concrete confined with a new rubber-based material, Line-X, are investigated in this chapter. Since, rubber will be sprayed to concrete after casting, the confined concrete may refer to as “rubber-coated concrete” in this study.

2.2. Research Objectives

Even though the behavior of FRP-confined concrete has been extensively investigated, the use of rubber as an external confinement was new, and was investigated for the first time in the present study. The main goal of this experimental study was to investigate the behavior of conventional concrete confined with a new rubber-based material. Mechanical properties of the rubber coated concrete was established and a stress-strain material model was proposed.

2.3. Properties of Rubber

The coating used in the present study (Fig. 2-1) consisted of an outer shell made with a layer of rubber named PX-3350, and a bed layer of LINE-X XPM to bond rubber (PX-3350) to concrete.

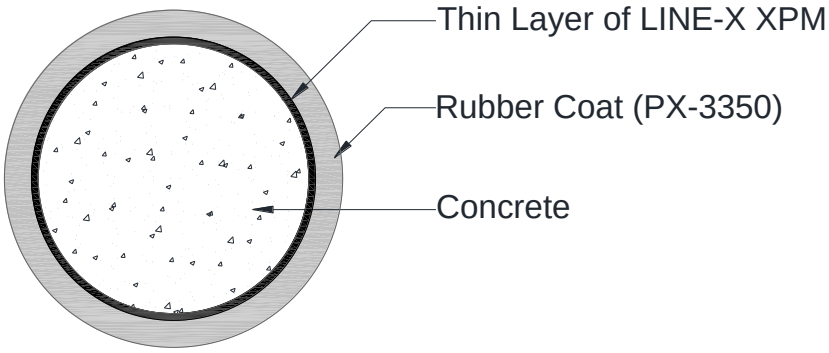

Figure 2-1. Top view of rubber-coated concrete sample

PX-3350 is a protective and durable elastomer that has been used for various applications (e.g. protect car beds, floors, concrete walls against abrasion, impact, and corrosion). PX-3350 is made with two components: 100% high performance aromatic polyurea as hardener, and 100% of Zero Volatile Organic Compounds (VOC) as resin. The two components are sprayed on a surface with high pressure for proper mixing and best polymerization results. In addition to providing protection, this material is moisture insensitive because of its pure polyurea chemistry. PX-3350 offers good adhesion properties to properly prepared substrates. PX-3350 also exhibits good resistance against chemical and moisture. The typical chemical and physical properties of this rubber composite are presented in Table 2-1. This material shows fast reactivity and cure time without any catalyst. This type of elastomer is usually used for blast mitigation, high performance protective coating applications, and high chemical resistance applications (LINE-X Franchise Development Company, 2016).

Table 2-1. Typical chemical and physical properties of PX-3350 (Technical data sheet – PX-3350, 2016)

Properties	Typical Value
Mix Ratio (by volume) *	1A:1B
Viscosity (cPS) @ 77°F	1000 ± 100 (A) & 370 ± 100 (B)
Material Density @ 77°F	9.50 lbs/gal (A) & 8.40 lbs/gal (B)
Elongation	82 %
Flexural Strength	2630 *psi*
Modulus of Elasticity	56000 *psi*
Tear Strength	497 *lbs/in.*
Tensile Strength	3432 *psi*
Volume Resistance	$2.3X10^{14}$ *ohm cm.*
Friction Coefficient	0.305 (static)

*A = Hardener; B = Resin

LINE-X XPM is a coat with high concentration of resin (usually referred to as high solid coat) used to bond polyurethane or polyurea elastomer to the substrate. It also provides a clean surface for the rubber coat (PX-3350). The typical properties of LINE-X XPM are presented in Table 2-2.

Table 2-2. Typical properties of LINE-X XPM (Technical data sheet- LINEX- X XPM, 2016)

Properties	Typical value
Solids by volume	65 % ± 2
Volatile Organic Compounds	0.83 *lb/gal*
Theoretical Coverage (DFT)	1040 ft^2/gal
Number of Coats	1
Mix Ratio (by volume)	0.6 “A” : 1.0 “B”
Shelf Life @ 60 -90°F	Part A-6 mos. Part B-12 mos.
Adhesion	ASTM C297 (1750 – 1910 *psi*)
Salt Spray Test	ASTM B117 (3,000 *hours*)
Pot life @ 90°F	1 ½ *hours*
Surface dry @ 70 -89°F	6 -10 *hours*

2.4. Unconfined and Confined Concrete

The concrete axial stress and strain capacities can be increased by applying compressive stress in the directions transverse to the axial load direction. Concrete confinement can be improved by jacketing or wrapping a section with either fiber reinforced polymer (FRP), steel, or concrete or by providing closely-spaced transverse reinforcement (e.g. hoops, spirals, and ties) in the section. In past, extensive studies

have been conducted to establish the stress-strain behavior of unconfined and confined concretes under uniaxial compressive loading.

The complete stress-strain relationship has been developed in previous studies for different confinement methods usually using basic properties of conventional concrete such as the compressive strength (f_c'), the strain at the peak stress (ε_o), and the modulus of elasticity of concrete (E_c). Previous studies (Nanni and Bradford, 1995; Samaan et al., 1998; Spoelstra and Monti, 1999; Wu et al., 2006; Jiang and Wu, 2012) concluded that the compressive stress-strain behavior of concrete mainly depends on the degree of confinement and the type of confining materials. It has been reported that for a section sufficiently confined with FRP, the confining pressure constantly increases resulting in a constant increase in stresses until FRP ruptures (Fig. 2-2). However, stress is sustained in steel-confined sections even after the yielding of reinforcing steel bars reaches (Wu and Wei, 2014). Several stress-strain models have been developed for various type of confinement. A brief review of the most cited concrete confinement models is presented herein.

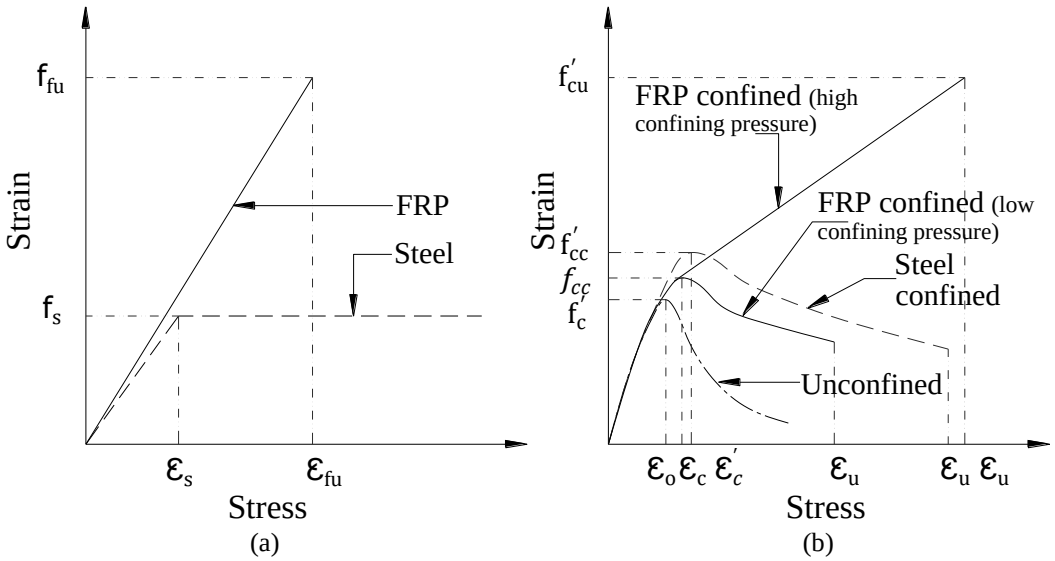

Figure 2-2. Typical stress-strain curves: (a) confining materials (b) confined concrete

2.4.1. Steel-Confined Model by Kent and Park (1971)

Kent and Park (1971) developed a stress-strain relationship (Fig. 2-3) for both unconfined and steel-confined concrete based on the Hognestad's model (Hognested, 1951). Kent's model better represents the post-peak behavior of confined concrete compared to the Hognestad's model. The relationship for unconfined concrete up to peak stress is:

$$f_c = f_c' \left[\frac{2\varepsilon_c}{\varepsilon_o} - \left(\frac{\varepsilon_c}{\varepsilon_o}\right)^2\right] \quad (2.1)$$

where, f_c' is the compressive strength of unconfined concrete, ε_o is the strain at the peak stress, f_c is the concrete stress at different strain (ε_c).

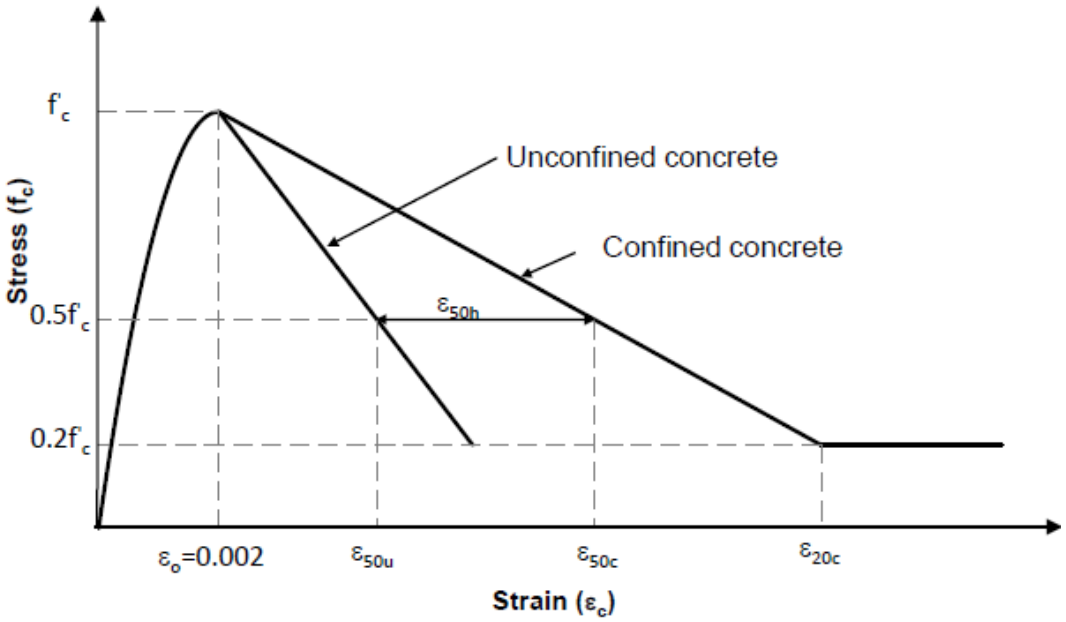

Figure 2-3. Stress-strain relationship for unconfined and steel-confined concrete (Kent and Park, 1971)

The post-peak branch was assumed to be a straight line with a slope that was a function of the concrete compressive strength:

$$f_c = f_c' \left[-Z(\varepsilon_c - \varepsilon_o)\right] \quad (2.2)$$

where, Z is the slope of straight line, to be calculated using Eq. 2.3; ε_{50u} is the strain corresponding to the stress equal to 50% of peak stress for unconfined concrete calculated using Eq. 2.4.

$$Z = \frac{0.5}{\varepsilon_{50u} - \varepsilon_o} \tag{2.3}$$

$$\varepsilon_{50u} = \frac{3 + 0.002 f_c'}{f_c' - 1000} \quad (f_c' \ in \ psi) \tag{2.4}$$

For confined concrete, it was assumed that the ascending branch of stress-strain model was the same as that for unconfined concrete but the post-peak branch was modified based on an empirical equation (Eq. 2.5).

$$f_c = f_c' \left[- Z(\varepsilon_c - \varepsilon_o) \right] \tag{2.5}$$

$$Z = \frac{0.5}{\varepsilon_{50h} + \varepsilon_{50u} - \varepsilon_o} \tag{2.6}$$

$$\varepsilon_{50h} = \varepsilon_{50c} - \varepsilon_{50u} = \frac{3}{4} \rho_s \sqrt{\frac{b''}{s}} \tag{2.7}$$

$$\varepsilon_{50u} = \frac{3 + 0.002 f_c'}{f_c' - 1000} \quad (f_c' \ in \ psi) \tag{2.8}$$

where ε_{50c} and ε_{50u} are the strains corresponding to the stress equal to 50% of peak stress for confined and unconfined concrete, respectively, b'' is the diameter of the core concrete (area inside the stirrups), s is the stirrup spacing, and ρ_s is the stirrup volumetric ratio.

2.4.2. Steel-Confined Model by Popovics (1973)

Popovics (1973) proposed a simple equation for the stress-strain behavior of both unconfined and steel-confined concrete using only three parameters ($f_c', \varepsilon_o, and\ E_c$).

$$\frac{f_c}{f_c'} = \frac{n\frac{\varepsilon_c}{\varepsilon_o}}{(n-1) + \left(\frac{\varepsilon_c}{\varepsilon_o}\right)^n} \tag{2.9}$$

where, f_c' is the compressive strength of unconfined concrete, ε_o is the strain at peak stress, and $E_c$is the modulus elasticity of concrete.

The power "*n*" can be expressed as a function of the concrete compressive strength. For normal-weight concrete, *n* is

$$n = 0.4 \times 10^{-3} f_c' + 1.0 \tag{2.10}$$

2.4.3. Steel-Confined Model by Mander et al. (1988)

Mander et al. (1988) proposed an equation to represent the stress-strain relationship of both unconfined and steel-confined concrete as

$$f_c = \frac{f_c' X r}{r - 1 + X^r} \tag{2.11}$$

where, f_c' is the concrete stress at peak. The term *X* and *r* are defined as

$$X = \frac{\varepsilon_o}{\varepsilon_c} \tag{2.12}$$

$$r = \frac{E_c}{E_c - \left(\frac{f_c'}{\varepsilon_c}\right)} \tag{2.13}$$

where, ε_c is the strain corresponds to a concrete stress and $E_c$is the modulus elasticity of concrete defined as

$$E_c = 57000\sqrt{f_c'} \quad (f_c' \; in \; psi)$$

2.4.4. FRP-Confined Model by Lim and Ozbakkaloglu (2014)

Lim and Ozbakkaloglu (2014) proposed a stress-strain relationship (Fig. 2-4) for the FRP-confined concrete sections:

$$f_c = \frac{f_{cc}' \left(\frac{\varepsilon_{co}}{\varepsilon_c}\right) r}{r - 1 + \left(\frac{\varepsilon_{co}}{\varepsilon_c}\right)^r} \qquad if \; 0 \leq \varepsilon_c \leq \varepsilon_o \tag{2.14}$$

$$f_c = f_{cc}' - \frac{(f_{cc}' - f_r')}{1 + \frac{0.45}{\left(\frac{\varepsilon_c - \varepsilon_{co}}{\varepsilon_f - \varepsilon_{co}}\right)^{-2}}} \qquad if \; \varepsilon_c > \varepsilon_{co} \tag{2.15}$$

where, f_{cc}' is the compressive strength of confined concrete, ε_{co} is the strain at peak stress, f_r' is the residual strength of the confined concrete, ε_f is the strain at the beginning of the residual strength, and r and E_c :

$$r = \frac{E_c}{E_c - \left(\frac{f_{cc}'}{\varepsilon_{co}}\right)} \tag{2.16}$$

$$E_c = 44000\sqrt{f_c'} \quad (f_c' \; in \; psi) \tag{2.17}$$

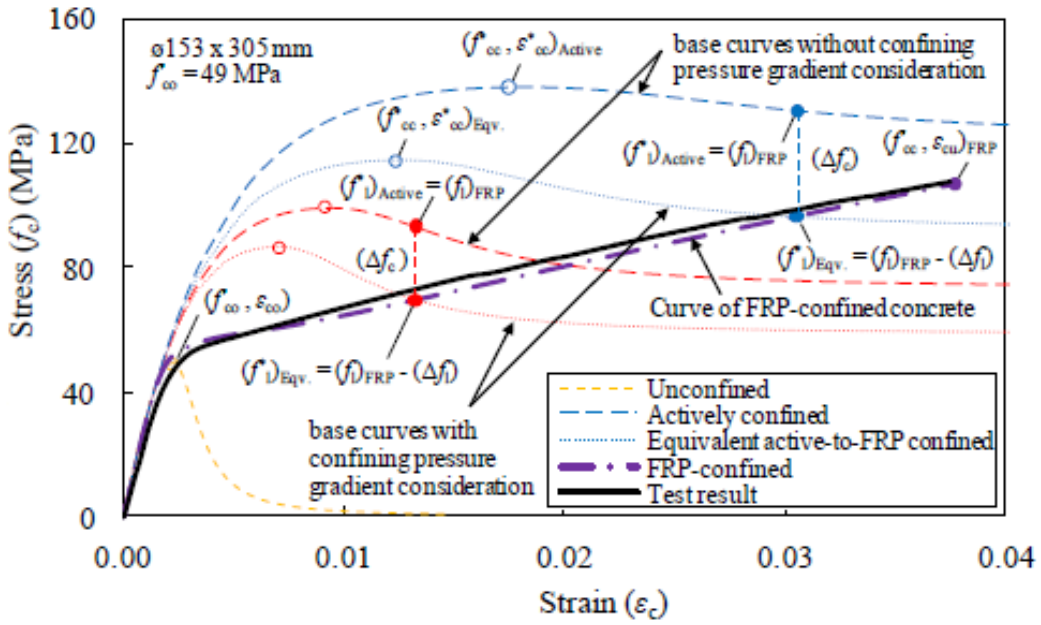

Figure 2-4. Stress-strain relationship of FRP-confined normal strength concrete using actively confined concrete model (Lim and Ozbakkaloglu, 2014)

2.5. Experimental Program

More than 30 concrete cylinders were casted and tested in the Concrete and Materials Laboratory at South Dakota State University in the present study to investigate the confinement of rubber confined concrete.

2.5.1. Test Matrix

A series of compressive tests were conducted for conventional and rubber-coated concrete specimens (Table 2-3) to investigate the mechanical properties of rubber confined concrete. A total of 30 concrete cylinders (6 by 12 *in.*) were casted (Fig. 2-5) according to ASTM C192-12 (2012)

Table 2-3. Test matrix for conventional and rubber confined concrete

Specimen	No. of Specimens	Specimen ID[(a)]	Specimen Size	Materials Properties
C	12	C1 to C12	6 by 12 *in.* Cylinder	Ready Mix Concrete with a strength of 5000 *psi*, Rubber Coat: PX-3350
LC-C-3	6	LCC3-1 to LCC3-6	6 by 12 *in.* Cylinder	
LC-C-6	6	LCC3-1 to LCC3-6	6 by 12 *in.* Cylinder	
LC-C-9	6	LCC3-1 to LCC3-6	6 by 12 *in.* Cylinder	

[(a)] LCC3=LC-C-3-1: "LC" refers to rubber coated, "C" refers to conventional unconfined concrete, "3" is the thickness of the rubber coat in mm, and 1 is the specimen number.

Figure 2-5. Casting of concrete cylinders

2.5.1.1. Reference Specimens

Of 30, 12 unconfined concrete specimens were tested as reference models. Ready mix concrete was used in this study in which Type II cement and two different types of admixture (WRDA 82 and MIRA 110) were used to achieve a compressive strength of 5000 *psi* (34.5 *MPa*). The slump of concrete was measured as 3.5 in. (88.9 *mm*) according to ASTM Standard C143 (2012).

2.5.1.2. Rubber Confined Specimens

Eighteen concrete cylinders were sprayed with rubber at the age of 28 days. Two steps were followed to complete coating: First, concrete surface was cleaned then and sprayed with the base layer, LINE-X XPM, then rubber, PX-3350, was sprayed (Fig. 2-1). Note that before applying the base layer, the concrete specimens were prepared with two different methods. In the first method, which was used in 16

samples, the concrete was simply cleaned ensuring that samples were free from any dust or loose concrete materials. In the second method, the concrete surface roughened by a hand grinder (Fig.2-6).

Rubber coating of a concrete sample generally included three steps: (1) preparing (for the case that the concrete surface was roughened as shown in Fig. 2-6) and cleaning the concrete surface, (2) spraying a base layer and allowing 12 hours of curing (Fig. 2-7), and (3) spraying the rubber (Fig. 2-8) using a high pressure (2000 psi) plural component spray gun. The rubber coat started to dry within 3 to 5 seconds. The entire coating process for 18 cylinders took approximately three hours. The thickness of rubber was measured during and after spraying (Fig. 2-9). Figure 2-10 shows the completed rubber-coated concrete specimens.

Figure 2-6. Concrete surface preparation for two specimens

Figure 2-7. Thin layer of base coat on concrete

Figure 2-8. Spraying rubber on concrete specimens

Figure 2-9. Rubber thickness measurement

Figure 2-10. Rubber-coated concrete specimens

The thickness of the rubber coat was constantly measured by the manufacturer to achieve the nominal thicknesses. However, the actual thickness of the rubber varied from 0.05 (1.3 *mm*) to 0.25 *in.* (6.6 *mm*), which was measured after the testing of the specimens, indicating that the manufacturer current method of measuring the thickness needs to be enhanced for structural applications since the actual thickness was 54% lower than the nominal thickness on average. After completion of the coating process, rubber coated concrete specimens were placed in the laboratory with standard room temperature.

2.5.2. Testing Procedure

The test samples were prepared according to ASTM Standard C617-12 (2012). The preparation included capping all specimens with high-strength Sulphur compound in order to provide full contact between the specimens and the head of loading platens.

(a) Complete test Setup

(b) Close-up of uncoated sample

(c) Close-up of coated Sample

Figure 2-11. Test setup for concrete compressive testing

Instron 400RD hydraulic compression testing machine (Fig. 2-11) was used to measure the compressive behavior of the test specimens. ASTM Standard C39-12 (2012) could not be directly used for the testing of the specimens since a slow-rate displacement-based loading protocol was needed to measure the full stress-strain relationship. The test was initiated with a displacement rate of 0.01 *in./min* (0.25 *mm/min*). When the displacement reached 0.20 *in.* (5.1 *mm*), which is approximately

equal to 1.25% strain in the concrete, the displacement-rate was increased to 0.1 *in./min* (2.54 *mm/min*).

A load cell was used to measure the forces thus stresses and an eight-inch extensometer with an accuracy of 10^{-6} *in./in*. and a 0.1-*in.* (2.54 *mm*) stroke was used to measure the strains of the concrete samples. The readings were recorded until failure. For rubber confined concrete, the extensometer was removed after reaching the extensometer limit. Subsequently, strains measured from head displacements were calibrated and used to obtain the complete stress-strain relationship (Fig. 2-12). The calibration of strains based on the head displacement readings was done by shifting the curve (Fig. 2-12b) to match the strain at the peak stress from the extensometer readings. For conventional concrete, the extensometer was removed when peak stress dropped approximately 70% of peak stress to avoid the damage of extensometer.

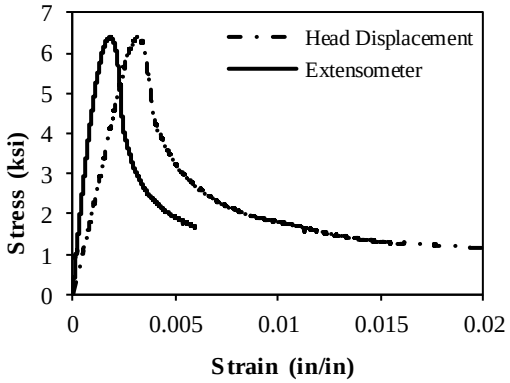

(a) Stress-strain relationships based on extensometer and head measurement

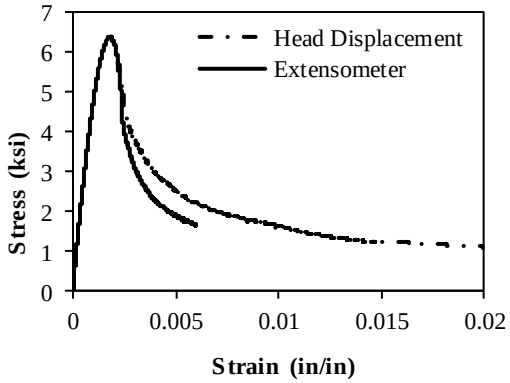

(b) Adjustment of stress-strain relationship

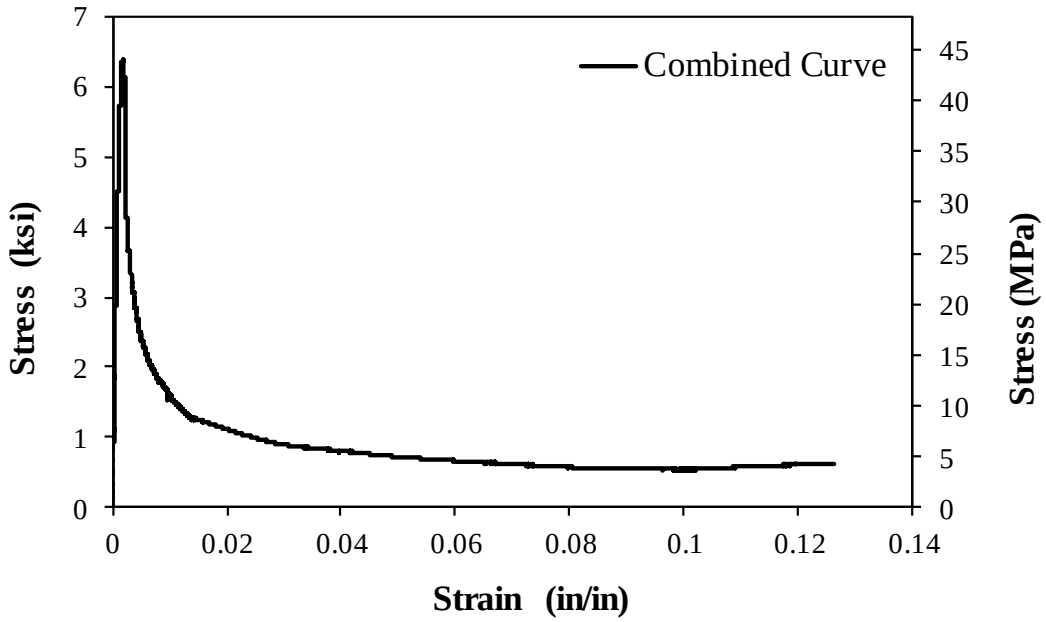

(c) Final stress-strain curve for rubber confined concrete

Figure 2-12. Complete stress-strain relationship

2.6. Experimental Results

2.6.1. Unconfined Concrete

A total of 12 uncoated concrete cylinders were tested at different ages to measure either only the compressive strength or the complete stress-strain behavior as reference for unconfined concrete.

2.6.1.1. Observed Damage

Previous experimental studies (Van Mier,1984; Torrenti et al.,1993) showed that concrete may fail under compression by cracking in either diagonal or parallel to the loading direction as shown in Fig. 2-13. It is reposted that the degradation of the concrete strength and stiffness subjected to uniaxial compression is because of cracking and splitting.

Figure 2-14 shows the failure mode of unconfined concrete specimens at different ages. Cracks were developed in many samples in the direction of the applied load. However, some samples failed near the ends with diagonal splitting.

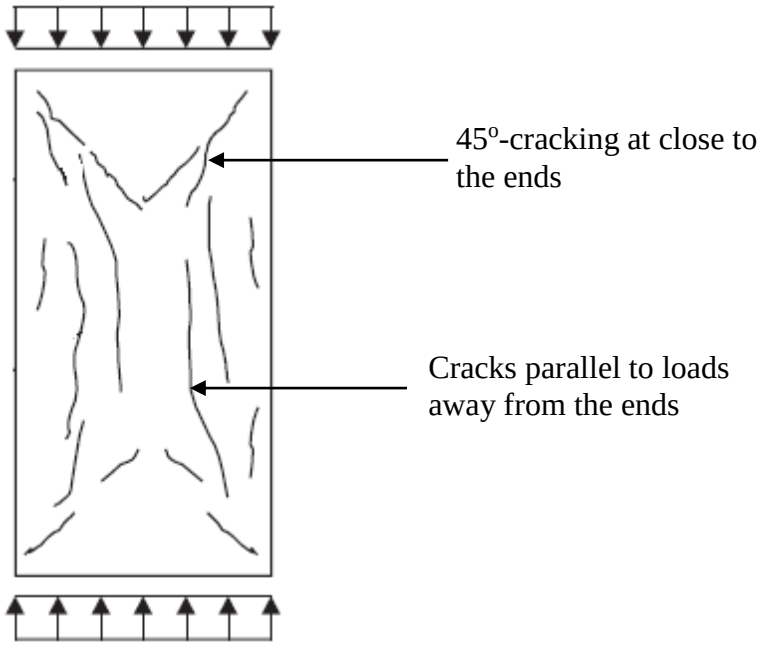

Figure 2-13. Typical crack patterns for normal concrete cylinders subjected to uniaxial loads

(a) 28 days (b) 45 days

(c) 45 days (d) 72 days

Figure 2-14. Failure of unconfined concrete specimens at different ages

2.6.1.2. Mechanical Properties

Table 2-4 presents the strength of unconfined concrete specimens. Three samples were tested for each specimen. Only the average of the test data was reported.

Table 2-4. Compressive strength of unconfined concrete

Specimen ID	Age (Days)	Compressive Strength, f_c' (*psi*)
C-1	28	5955
C-2	45	6045
C-3	72	6105
C-4	92	6510
C-5	133	6610

Note: Three samples were tested for each specimen. Only the average of the test data was reported.

2.6.1.3. Full Stress-Strain Relationship

Full stress-strain relationships of the unconfined concrete specimens were measured using the testing method described in the previous section. Figure 2-15 shows a sample of the measured stress-strain relationship for specimen C3. Included in the figure is the calculated stress-strain relationship based on the Mander's model (Mander et al., 1988) for unconfined concrete. It can be seen that the unconfined concrete residual strength at strains greater than 0.005 *in./in*. was negligible.

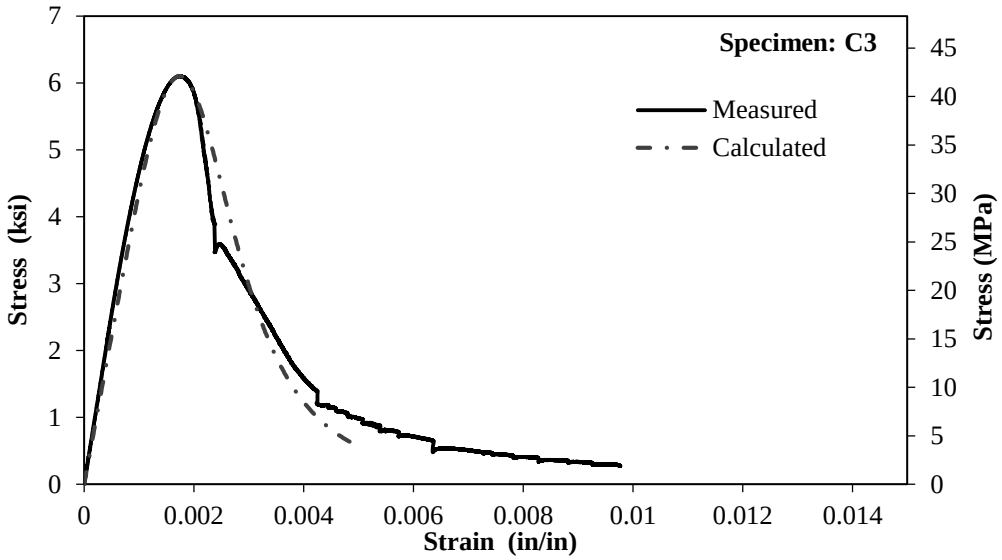

Figure 2-15. Measured and calculated stress-strain relationships for unconfined concrete

2.6.3. Rubber Confined Concrete

A total of 18 rubber confined concrete specimens with different coat thicknesses (Table 2-3) were tested to determine the mechanical properties and to observe the stress-strain behavior.

2.6.3.1. Observed Damage

Figure 2-16 shows the damage state of a rubber confine concrete specimen at different strains level. Figure 2-17 shows the failure of rubber confined concrete samples at different rubber coat thickness. All rubber confined concrete samples failed at very large strains (exceeding 10%, which is in the range of strain capacity of steel reinforcement) by the rupture of the rubber in the direction of applied axial load. Table 2-5 presents the mode of failure and the measured mechanical properties for rubber confined concrete samples.

(a) Damage at maximum stress (strain 0.001791in./in.)

(b) Damage at post peak stage (strain 0.01 in./in.)

(c) Damage before failure (strain 0.09 in./in)

Figure 2-16. Damage state of rubber confined concrete


(a) Failure of rubber [t=0.125 in. (3 mm)]

(a) Failure of rubber [t=0.25 in. (6 mm)]

(a) Failure of rubber [t=0.375 in. (9 mm)]

Figure 2-17. Failure of rubber confined concrete with different thicknesses

Table 2-5. Summary of test results for rubber confined concrete specimens

Spec. ID	Actual Thickness, t $(in.)$	Compressive Strength, $f_c'(ksi)$	Residual Strength, f_r' (ksi)	Ultimate Strain, $\varepsilon_{cu}(in./in.)$	Failure mode
LCC3-1	0.04	5.04	1.107	0.01847	Rubber rupture approximately at the middle of the specimens
LCC3-2	0.05	5.80	0.339	0.11142	
LCC3-3	0.02	6.37	0.833	0.00765	
LCC3-4	0.05	6.17	0.474	0.14631	
LCC3-5	0.07	6.56	0.678	0.03823	Rubber rupture close to the ends of specimens
LCC3-6	0.05	6.61	0.585	0.08819	
LCC6-1	0.06	6.38	0.614	0.12646	Rubber rupture approximately at the middle of the specimens
LCC6-2	0.06	6.67	0.547	0.05839	
LCC6-3	0.09	6.58	0.651	0.09910	
LCC6-4	0.10	6.15	0.572	0.10003	
LCC6-5	0.10	5.85	0.506	0.07219	
LCC6-6	0.08	5.75	0.802	0.20589	
LCC9-1	0.19	6.40	1.211	0.20861	Rubber did not rupture since the test was stopped to avoid damage of the setup
LCC9-2	0.21	5.22	1.162	0.21197	
LCC9-3	0.22	6.69	1.101	0.17824	
LCC9-4	0.20	6.07	1.019	0.09469	
LCC9-5	0.26	6.32	1.219	0.11955	
LCC9-6	0.21	5.95	1.115	0.07368	

In the specimens with a thick layer of rubber, the text and reading was stopped to avoid damage of displacement head (Fig. 2-18). In these cases, the specimens was adjusted and pushed to failure using a high displacement rate (Fig. 2-19). When the specimens failed, samples of the rubber at the location of rupture were collected to

measure the thickness. The average of the measured (actual) thicknesses of the samples was presented in Table 2-5. Figure 2-20 shows the failure of all rubber confined concrete specimens.

Figure 2-21 and Figure 2-22 show that the rubber confinement appears different at different strain capacity. It was observed that concrete was bulging inside the samples, the rubber-coat was deviated from their original condition, but the rubber-coat was capable to hold the concrete until to achieve very large strain capacity, exceed the strain capacity of steel, especially, when the thickness of rubber coat was greater than 0.08 *in.* (2 *mm*), Fig. 2-21. It was also observed that the higher thickness of rubber-coat showed extreme strain capacity, Fig. 2-22, the machine was stopped before failure of specimens as the head reached its maximum displacement limit, Table 2-5.


(a) Before Stopping the Test (b) Extracting Rubber to determine thickness

Figure 2-18. Damage of confined concrete with a thick layer of rubber


(a) Before Stopping the Test (b) Manual Failure

Figure 2-19. Failure of rubber confined concrete at 18% strain


(i) LCC3-1


(ii) LCC3-2


(iii) LCC3-3


(iv) LCC3-4


(v) LCC3-5


(vi) LCC3-6


(vii) LCC6-1


(viii) LCC6-2


(ix) LCC6-3


(x) LCC6-4


(xi) LCC6-5


(xii) LCC6-6


(xiij) LCC9-1


(xiv) LCC9-2


(xv) LCC9-3


(xvi) LCC9-4


(xvii) LCC9-5


(xviii) LCC9-6

Figure 2-20. Failure of all rubber confined concrete specimens


Strain 0.0013 *in/in*


Strain 0.0058 *in/in*


Strain 0.0018 *in/in*


Strain 0.0103 *in/in*


Strain 0.0216 *in/in*


Strain 0.0473 *in/in*


Strain 0.1068 *in/in*


Strain 0.1213 *in/in*


Strain 0.1463 *in/in*

Figure 2-21. Strain capacity of rubber confined concrete at different stages during uniaxial compression test: Specimen LCC3-4


Strain 0.0007 *in/in*


Strain 0.0031 *in/in*


Strain 0.0048 *in/in*


Strain 0.0144 *in/in*


Strain 0.0371 *in/in*


Strain 0.1023 *in/in*


Strain 0.1274 *in/in*


Strain 0.1744 *in/in*


Strain 0.1971 *in/in*


Strain 0.2171 *in/in*


Strain 0.2197 *in/in*


Machine was stopped

Figure 2-22. Strain capacity of rubber confined concrete at different stages during uniaxial compression test: Specimen LCC9-2

2.6.3.2. Mechanical Properties

Table 2-6 presents a summary of measured mechanical properties for rubber confined concrete. Even though sections well-confined with steel for FRP generally exhibit relatively large compressive strength, rubber confined sections do not show significant increase in the compressive strength mainly because of the low strength and stiffness of the rubber. However, it was found that the strain capacity of a rubber confined concrete exceeds that of a steel bar (more than 10% strain). This is a unique property that may avoid core concrete failure in any RC section and ensure reinforcement fracture. This is especially important for the repair or retrofit of RC bridges and buildings with low ductility.

Table 2-6. Compressive strength of rubber coated concrete cylinder specimens (6" X 12") with different thickness and at different ages

Spec. ID	Age (days)	Actual Thickness, t $(in.)$	Compressive Strength, $f_c'(ksi)$	Strain at Peak Stress, $\varepsilon(ksi)$	Residual Strength, f_r' (ksi)	Ultimate Strain, $\varepsilon_{cu}(in./in.)$
LCC3-1	72	0.04	5.04	0.0014	1.11	0.0185
LCC3-2		0.05	5.8	0.0018	0.34	0.1114
LCC3-3	76	0.02	6.37	0.0017	0.83	0.0076
LCC3-4		0.05	6.17	0.0018	0.47	0.1463
LCC3-5		0.07	6.56	0.0017	0.68	0.0382
LCC3-6	133	0.05	6.61	0.0018	0.59	0.0882
LCC6-1	92	0.06	6.38	0.0018	0.61	0.1265
LCC6-2		0.06	6.67	0.0019	0.55	0.0584
LCC6-3		0.09	6.58	0.0019	0.65	0.0991
LCC6-4	133	0.10	6.15	0.0017	0.57	0.1000
LCC6-5		0.10	5.85	0.0015	0.51	0.0722
LCC6-6		0.08	5.75	0.0015	0.80	0.2059
LCC9-1	133	0.19	6.4	0.0018	1.21	0.2086
LCC9-2	94	0.21	5.22	0.0015	1.16	0.2120
LCC9-3		0.22	6.69	0.0017	1.10	0.1782
LCC9-4	133	0.20	6.07	0.0018	1.02	0.0947
LCC9-5		0.26	6.32	0.0017	1.22	0.1195
LCC9-6		0.21	5.95	0.0019	1.12	0.0737

2.6.3.3. Full Stress-Strain Relationship

Figure 2-23 shows a sample of full stress-strain relationship for a rubber-confined concrete specimen. It can be seen that the peak stress and its corresponding strain for rubber coated concrete are approximately the same as those for uncoated conventional concrete. Since this behavior was also seen for different thicknesses of the rubber (Fig. 2-24 to Fig. 2-26), it was be inferred that this type of confinement does not improve the peak stress as well as the strain at the peak stress. The residual strength of the rubber coated concrete is higher than unconfined concrete but lower than that seen in other confining methods (e.g. steel reinforcement, jacketing). Nevertheless, rubber-confined concrete exhibits more than 10% strain capacity (Fig. 2-24 to Fig. 2-26), which is comparable to that of reinforcing steel bars. This unique behavior will improve displacement capacity of low-confined concrete sections (e.g. bridge columns, beams in old buildings) by eliminating the core concrete failure and by allowing the reinforcement to reach their ultimate capacities.

Of 18 rubber coated concrete specimens, the concrete surface of two specimens (LCC3-6 and LCC9-5) were made as roughened by grinding (described in previous section) before provide a base layer concrete surface. This technique was applied to observe the bonding behavior between concrete and rubber coat compared two all other specimens. The stress-strain response of these two specimens was same compared to other specimens, which indicate that roughened concrete surface does not improve the structural behavior of rubber confined concrete.

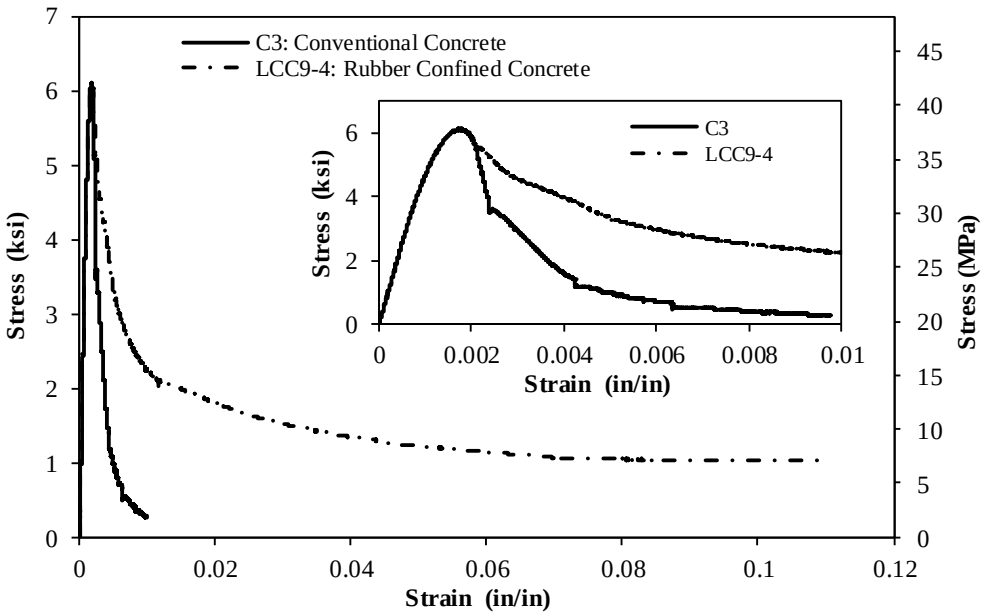

Figure 2-23. Complete stress-strain relationship for conventional and rubber confined concrete

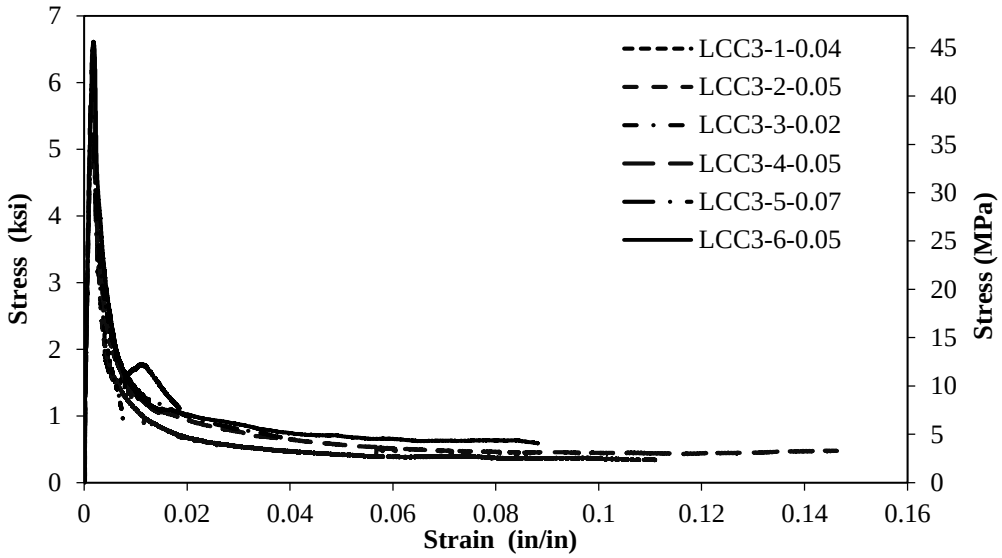

Figure 2-24. Stress-strain relationships for rubber confined concrete specimens with 3-mm nominal thickness

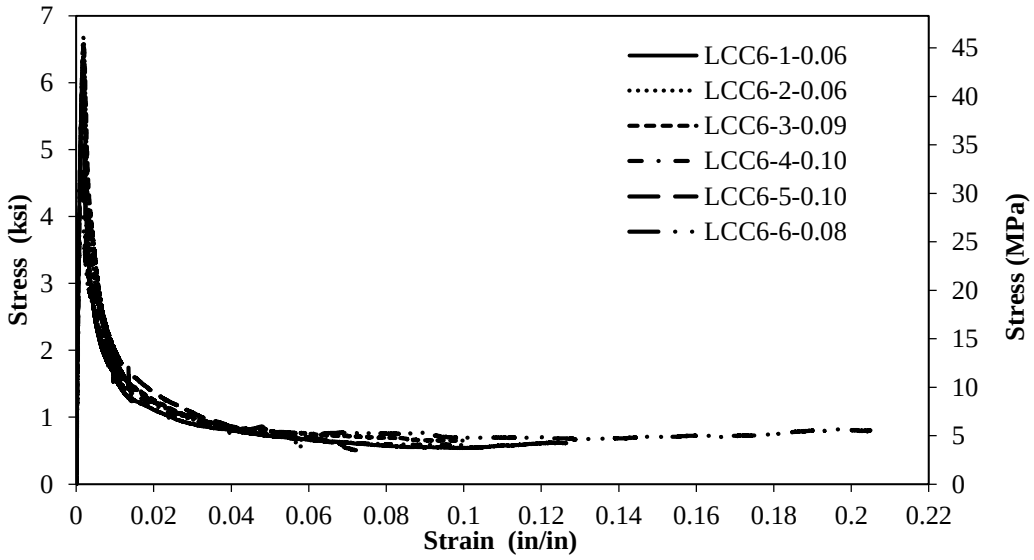

Figure 2-25. Stress-strain relationships for rubber confined concrete specimens with 6-mm nominal thickness

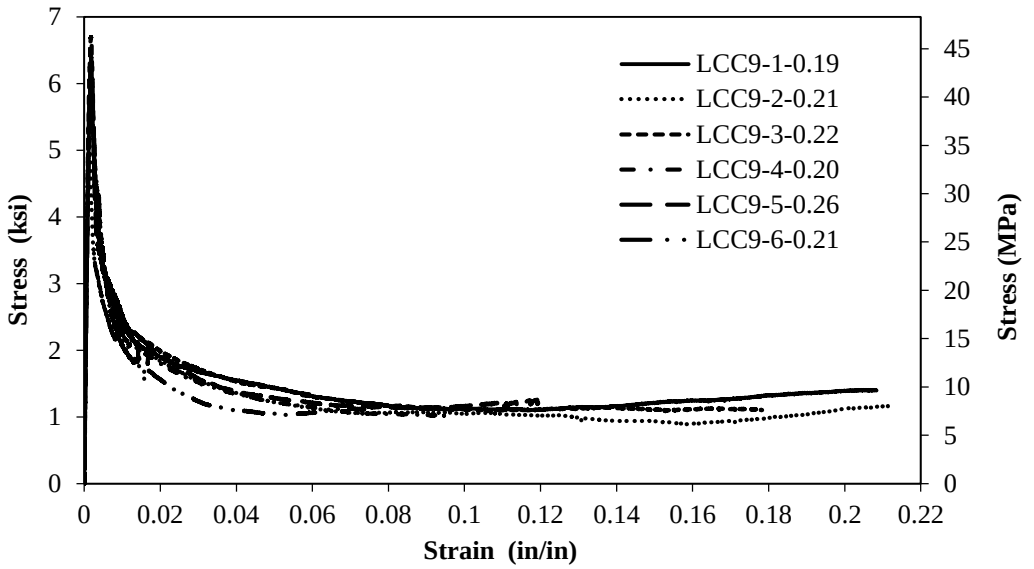

Figure 2-26. Stress-strain relationship for rubber confined concrete specimens with 9-mm nominal thickness

2.7. Stress-Strain Model for Rubber-Confined Concrete

2.7.1. Introduction

Complete stress-strain relationship for confined concrete is necessary for displacement-based design of ductile members such as bridge columns and building beams and columns. A stress-strain material model was developed for rubber confined concrete based on the experimental data. First, a somewhat complex stress-strain material model is presented followed by a simplified version, which allows the analysis of rubber confined sections using most commercial finite element packages without any further upgrade.

2.7.2. Proposed Stress-Strain Models

Two stress-strain material models for rubber confined concrete were developed based on experimental results (Fig. 2-27 and 2-28). The model shown in Fig. 2-27, represents the behavior of rubber confined concrete using nonlinear relationships. However, lines were used to simulate the post-peak behavior of rubber confined concrete in the simplified model (Fig. 2-28).

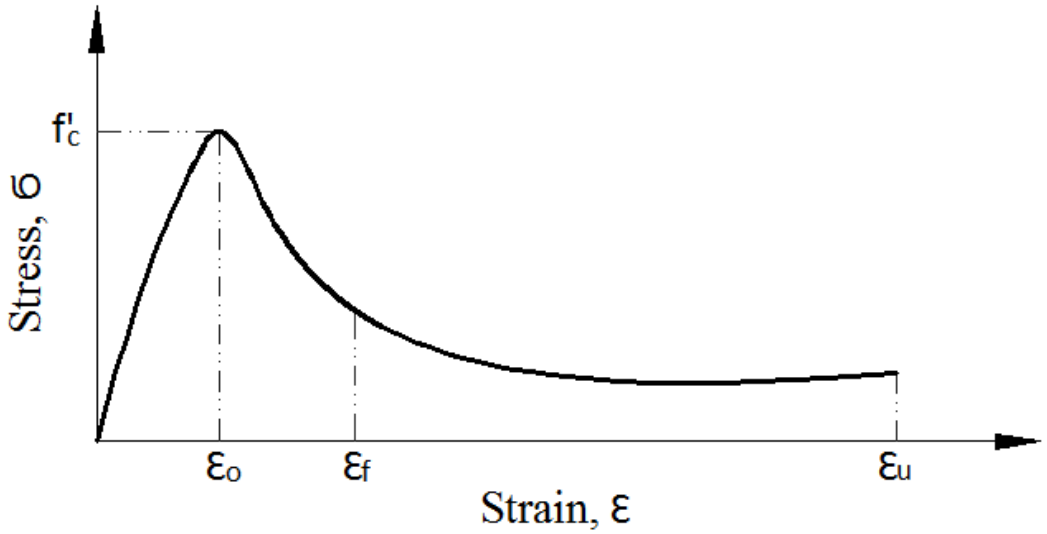

Figure 2-27. Nonlinear stress-strain relationship for rubber confined concrete

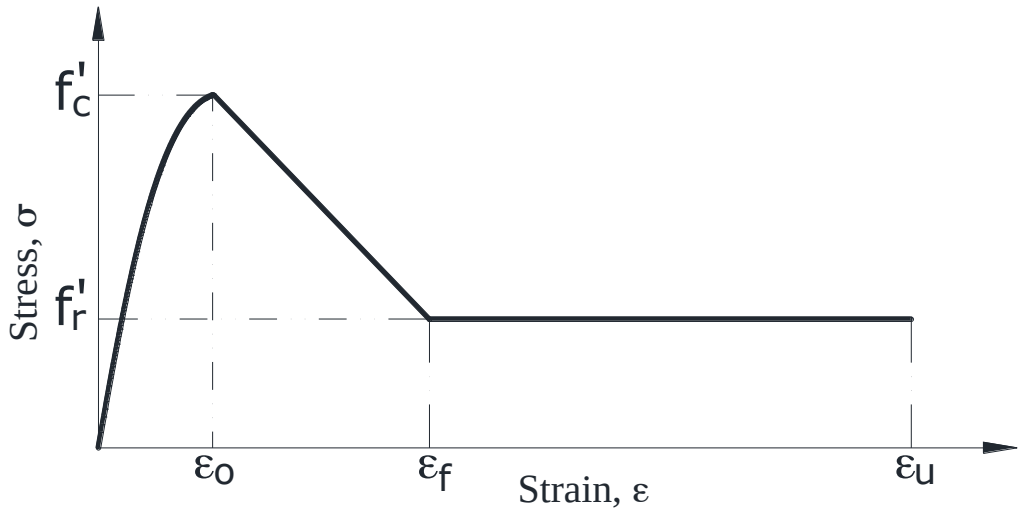

Figure 2-28. Simplified stress-strain relationship for rubber confined concrete

The critical points of the models are:

f_c' = the compressive strength of unconfined concrete,

ε_o = the strain at peak stress,

f_r' = the residual strength of rubber confined concrete,

ε_f = the strain at the initiation of the plateau,

ε_u = the ultimate strain of rubber confined concrete,

t = the thickness of rubber.

A summary of derivation of equations that are need to obtain the critical parameters of the rubber confined concrete models is presented herein. Note that since rubber does not increase the compressive strength, no equation was developed for this parameter.

2.7.3. Confining Pressure

Concrete expands laterally when it is subjected to axial compression. This expansion can be confined using a jacket (e.g. FRP) or transverse reinforcement. The lateral confining pressure may be assumed constant for a steel-confined concrete

section after the reinforcement yielding. However, the confining pressure provided by an FRP jacket, increases due to linear-elastic behavior of FRP.

For rubber confined concrete, the confining pressure is assumed to be uniformly distributed around the circumference of the section as schematically shown in Fig. 2-29 thus:

$$f_l = \frac{2E_f \varepsilon_{fu} t}{D} \tag{2.18}$$

where, f_l is the confining pressure, E_f is the modulus of elasticity of rubber, ε_{fu} is the tensile strain capacity of rubber, t is the thickness of rubber, and D is the diameter of concrete cylinder.

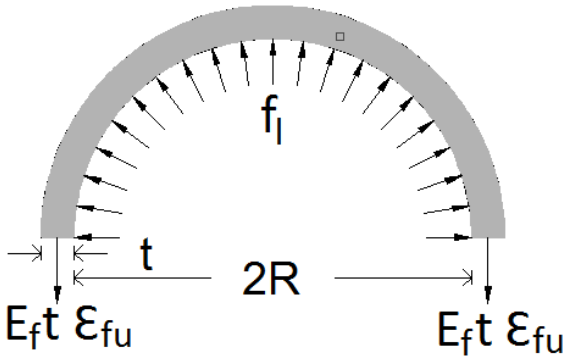

Figure 2-29. Confining pressure for rubber confined concrete

2.7.4. Residual Strength

Confined concrete usually exhibits residual strength after reaching the peak stress. The test results of rubber confined concrete specimens show that the thickness of the rubber affects the residual strength since thicker rubber increases the concrete confining pressure. Fig. 2-30 shows the normalized residual strength $\left(\frac{f_r'}{f_c'}\right)$ versus the normalized confining pressure $\left(\frac{f_l}{f_c'}\right)$ for all specimens. A regression analysis was

carried out to establish a relationship between the residual strength and the confining pressure, which includes the effect of the rubber thickness (Eq. 2.18).

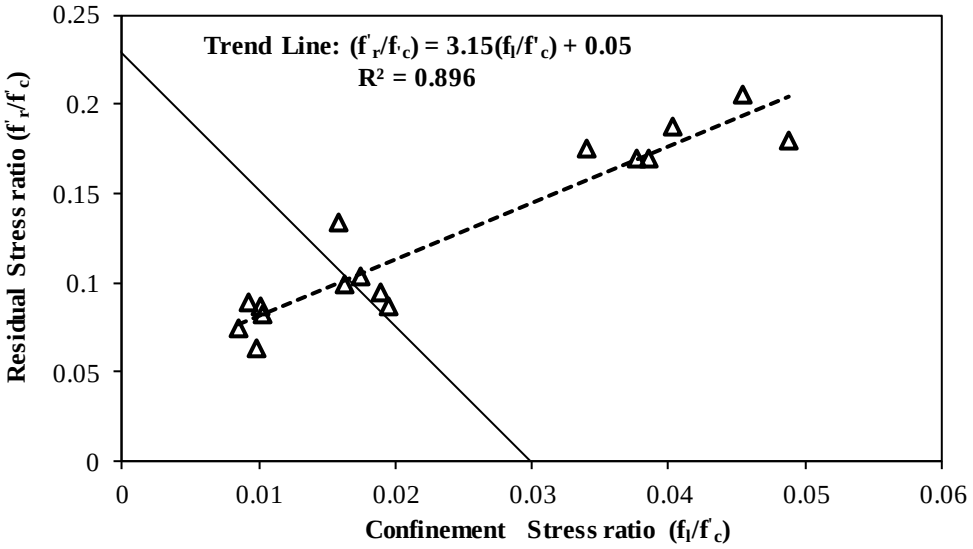

Figure 2-30. Residual strength vs. confining pressure for rubber confined concrete

Based on the statistical analysis, the residual strength of a rubber confined concrete section can be calculated:

$$f_r' = f_c' \left[3.15\left(\frac{f_l}{f_c'}\right) + 0.05\right] \qquad (2.19)$$

where, f_r' is the residual strength for a rubber confined concrete section, f_l' is the confining pressure, and f_c' is the compressive strength of the unconfined concrete.

2.7.5. Ultimate Strain

Previous studies have shown that the ultimate strain of a steel-confined section depends on the confining pressure and the strain at the peak stress of transverse reinforcement. The same method can be used for the rubber confined section concrete. However, the strain capacity of 13 out of 18 rubber confined specimens in which the rubber thickness was 0.05 *in.* (1.27 *mm*) or greater was more than 10%

(Fig. 2-31), which is comparable to that of reinforcing steel bars. The ultimate strain in other specimens where lower since the actual thickness of the rubber at the failure location was insufficient and was 50% lower than the nominal thickness. Overall, it can be assumed that the ultimate strain of a rubber confined concrete section is 10%.

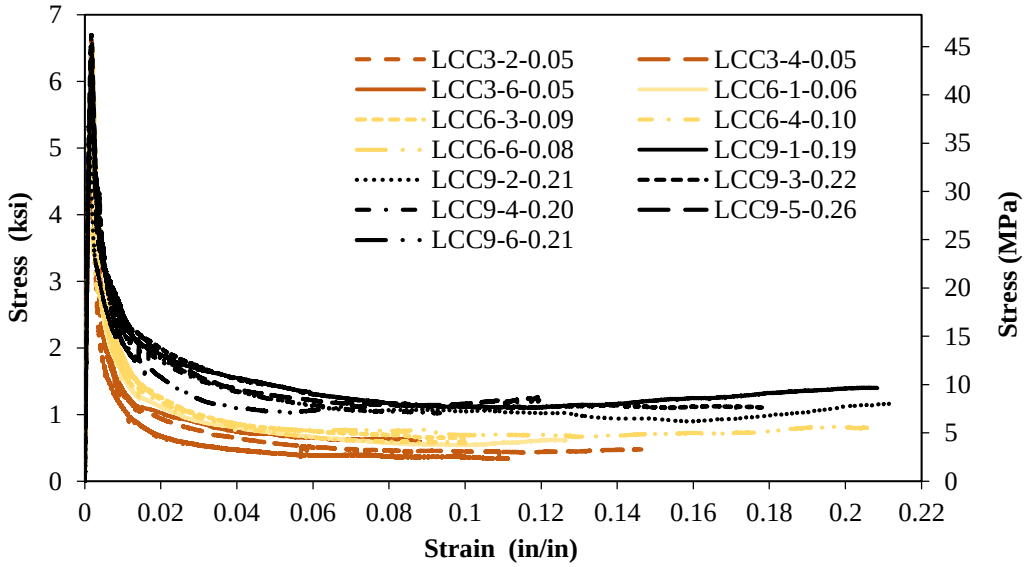

Figure 2-31. Stress-strain relationships for 13 rubber confined concrete specimens with a minimum rubber thickness of 0.05 in. (1.2 mm)

2.7.6. Strain Corresponding to Initiation of Residual Strength

It was necessary to determine the strain at the beginning of the residual stress plateau for the development of stress-strain relationships. The experimental results showed that the post-peak stress behavior of a rubber confined concrete section depends on the thickness of the rubber (Fig 2-31). The strain at the initiation of the residual stress plateau was calculated based on the experimental results using a statistical analysis (Fig. 2-32). First, the stress at 100, 75, 50, and 25% of the peak stress on the descending branch of the test data was normalized to the peak stress $\left(\frac{f_l}{f_c'}\right)$ for all 18 specimens. Only the average less one standard deviation of the stresses at each stress level was used for the further analysis. Subsequently, strains

corresponding to 100, 75, 50, and 25% of the peak stresses were normalized to the strain at the peak stress $\left(\frac{\varepsilon_c}{\varepsilon_o}\right)$ then the average less one standard deviation of these strains at each stress level was obtained. The normalized strains were plotted against the normalized stresses as shown in Fig. 2-32. Finally, a curve was fitted to the dataset and the strain at the initiation of the residual stress plateau (ε_f) was obtained as:

$$\varepsilon_f = \varepsilon_o \left[-2.263 \ln\left(\frac{f_r'}{f_c'}\right) + 0.786\right] \qquad 2.20$$

All parameters were defined in the previous section.

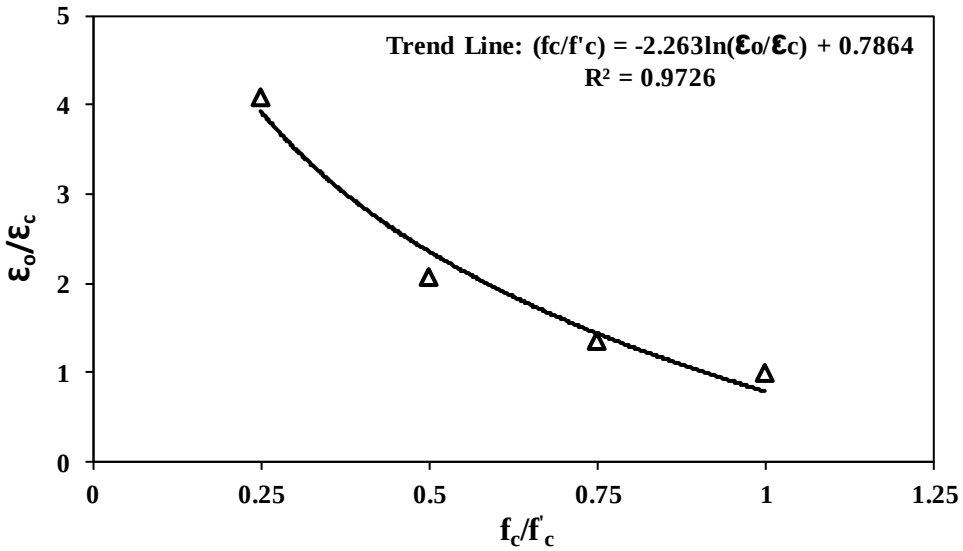

Figure 2-32. Post-peak stress-strain relationship for 18 rubber confined concrete specimens

2.7.7. Nonlinear Stress-Strain Model

Complete stress-strain relationship (Fig. 2.27) for a rubber confined concrete section can be expressed using two equations in which the initial behavior up to the peak stress follows the Popovics's model (Popovics, 1973):

$$f_c = \frac{f_c' \left(\frac{\varepsilon_c}{\varepsilon_o}\right) r}{r - 1 + \left(\frac{\varepsilon_c}{\varepsilon_o}\right)^r} \quad if \ 0 \leq \varepsilon_c \leq \varepsilon_o \qquad 2.21$$

where.

$$r = \frac{E_c}{E_c - \left(\frac{f_c'}{\varepsilon_0}\right)} \qquad (2.22)$$

$$E_c = 57000 \sqrt{f_c'} \ \ (psi) \qquad (2.23)$$

The descending branch can be expressed by an equation (Eq. 2.24) which was originally developed by Lim and Ozbakkaloglu (2014). This equation was modified to best fit the post-peak behavior of rubber confined concrete sections

$$f_c = f_c' - \frac{(f_c' - f_r')}{1 + \frac{0.45}{\left(\frac{\varepsilon_c - \varepsilon_o}{\varepsilon_f - \varepsilon_o}\right)^{1.45}}} \quad if \ \varepsilon_c > \varepsilon_o \qquad (2.24)$$

All parameters where defined in the previous sections.

The measured stress-strain relationships of four rubber confined concrete specimens were compared with the calculated stress-strain relationships using the proposed nonlinear model (Fig. 2-33 to 2-36). It can be seen that the proposed nonlinear model reproduced the measured data with a reasonable accuracy.

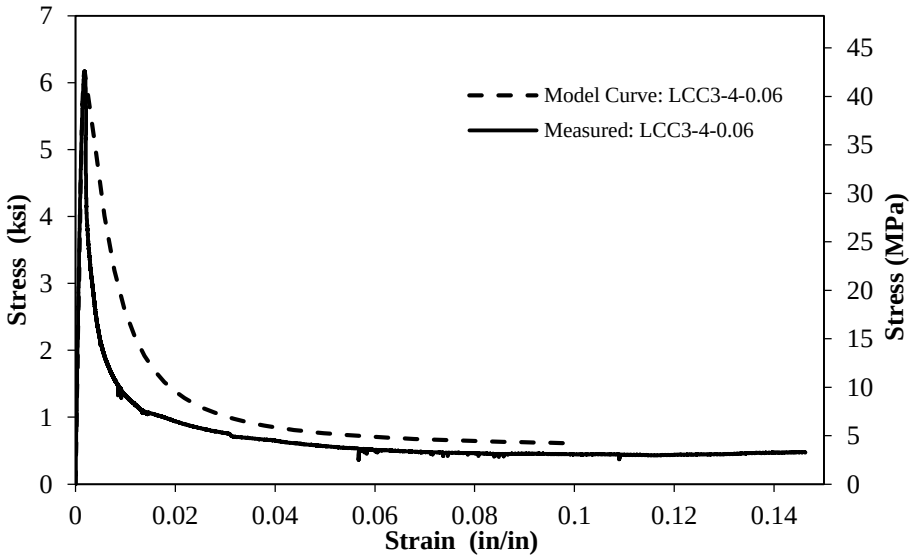

Figure 2-33. Measured and calculated (nonlinear model) stress-strain relationships for rubber confined concrete for specimen LCC3-4

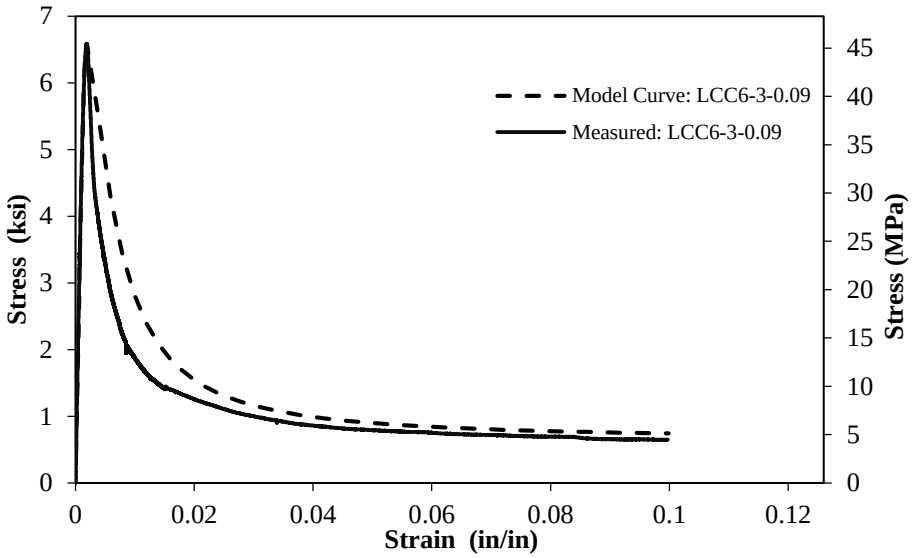

Figure 2-34. Measured and calculated (nonlinear model) stress-strain relationships for rubber confined concrete for specimen LCC6-3

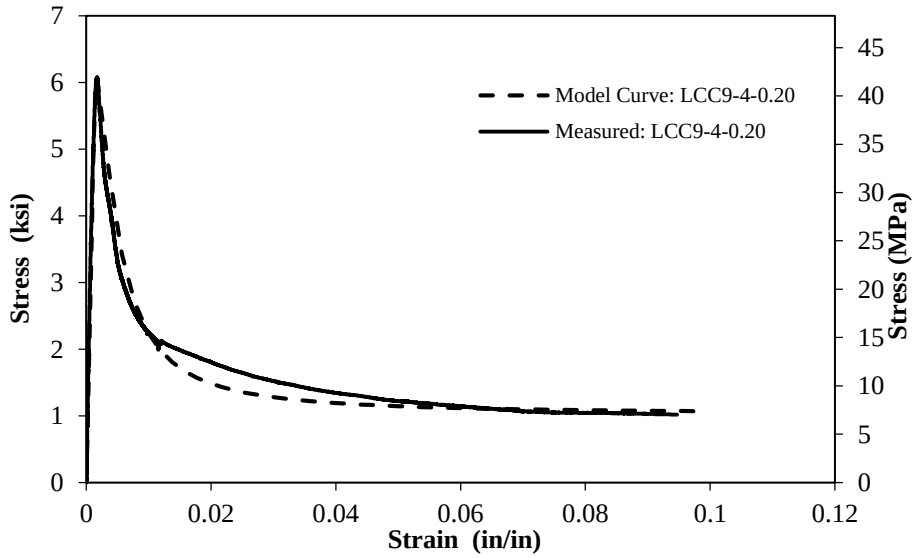

Figure 2-35. Measured and calculated (nonlinear model) stress-strain relationships for rubber confined concrete for specimen LCC9-4

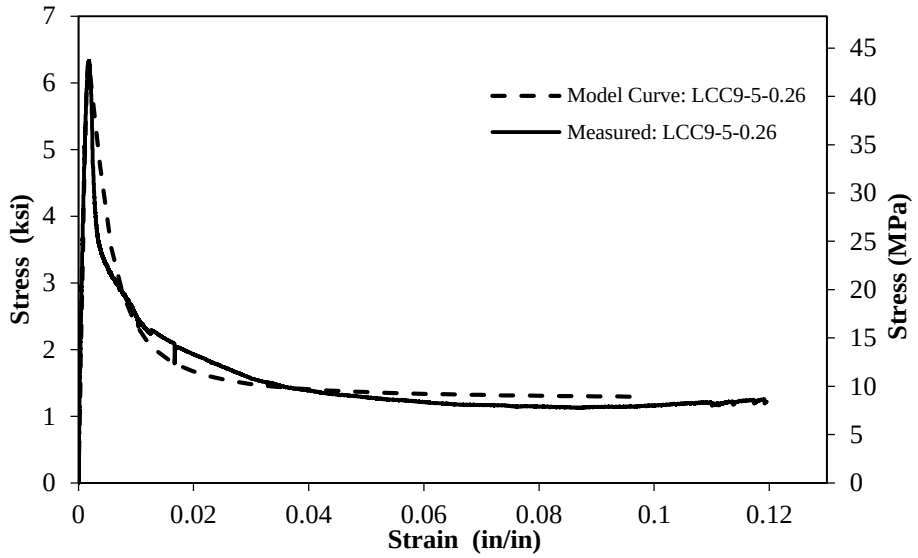

Figure 2-36. Measured and calculated (nonlinear model) stress-strain relationships for rubber confined concrete for specimen LCC9-5

2.7.8. Simplified Stress-Strain Model

A simple stress-strain model (Fig. 2-28) was developed for rubber confined concrete sections to further help engineers in the modeling of RC members with this type of confinement. The ascending branch of the stress-strain relationship can be expressed using Popovics's model (Popovics, 1973).

$$f_c = \frac{f_c' \, x \, r}{r - 1 + x^r} \tag{2.25}$$

where

$$x = \frac{\varepsilon_o}{\varepsilon_c} \tag{2.26}$$

$$r = \frac{E_c}{E_c - \left(\frac{f_c'}{\varepsilon_0}\right)} \tag{2.27}$$

$$E_c = 57000 \sqrt{f_c'} \ \ (psi) \tag{2.28}$$

The descending branch was assumed to be a straight line connecting the peak stress point to the initiation of the residual stress.

$$f_c = \ f_c' - M(\varepsilon_c - \ \varepsilon_o) \tag{2.29}$$

where, M is the slope of straight line to be calculated:

$$M = \frac{(f_c' - f_r')}{(\varepsilon_f - \ \varepsilon_o)} \tag{2.30}$$

All parameters where defined in the previous section.

The graphical representation of the simplified complete stress-strain relationship of rubber confined concrete was shown in Fig. 2-28, which was developed using proposed equation (Eq. 2.25 and Eq. 2.29). This proposed simplified model shows good contribution with experimental data of each rubber coated concrete. Figure 2-37 to 2-40 shows the comparison stress-strain relationship of rubber coated concrete based on experimental data and proposed simplified model.

The measured stress-strain relationships of four rubber confined concrete specimens were compared with proposed simplified model (Fig. 2-37 to Fig. 2-240).

It can be observed that the proposed simplified model produced confinement properties of measured test data with a good accuracy. So, it can be concluded that it is possible to develop the stress-strain relationship of rubber confinement concrete with knowing the properties of rubber, such as, thickness, modulus of elasticity, and the tensile strength of rubber.

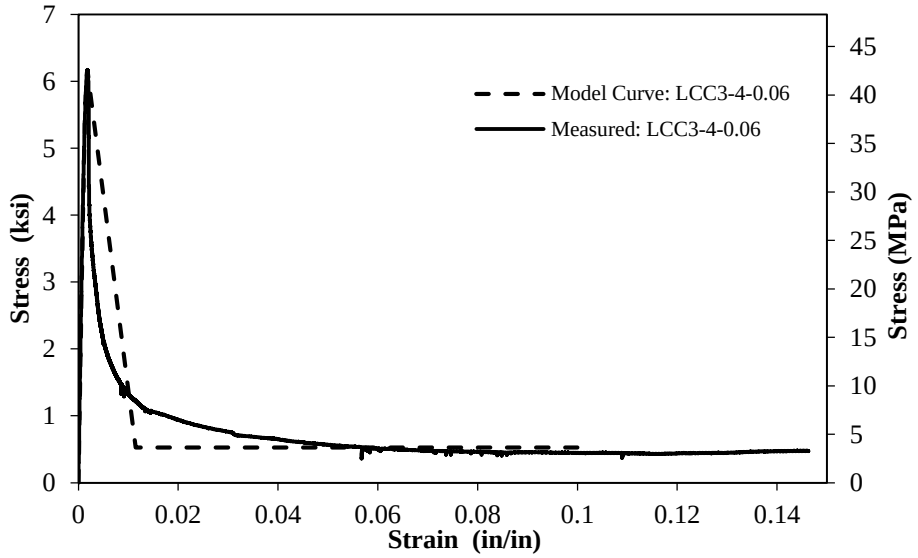

Figure 2-37. Measured and calculated (nonlinear model) stress-strain relationships for rubber confined concrete for specimen LCC3-4

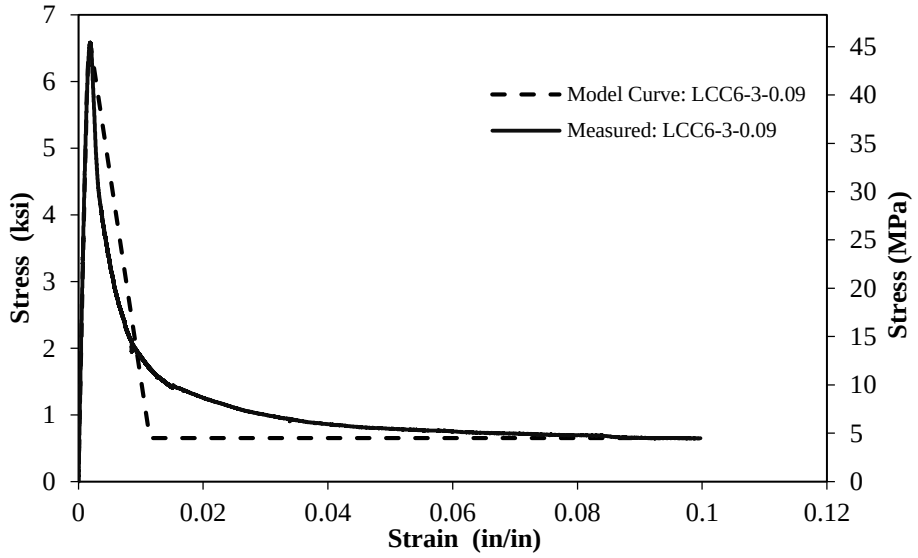

Figure 2-38. Measured and calculated (nonlinear model) stress-strain relationships for rubber confined concrete for specimen LCC6-3

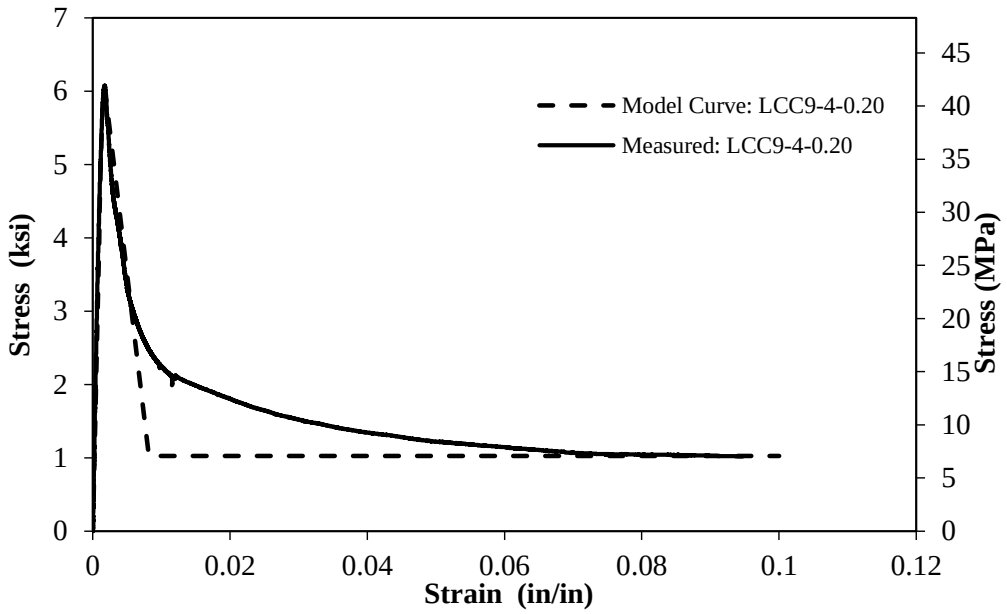

Figure 2-39. Measured and calculated (nonlinear model) stress-strain relationships for rubber confined concrete for specimen LCC9-4

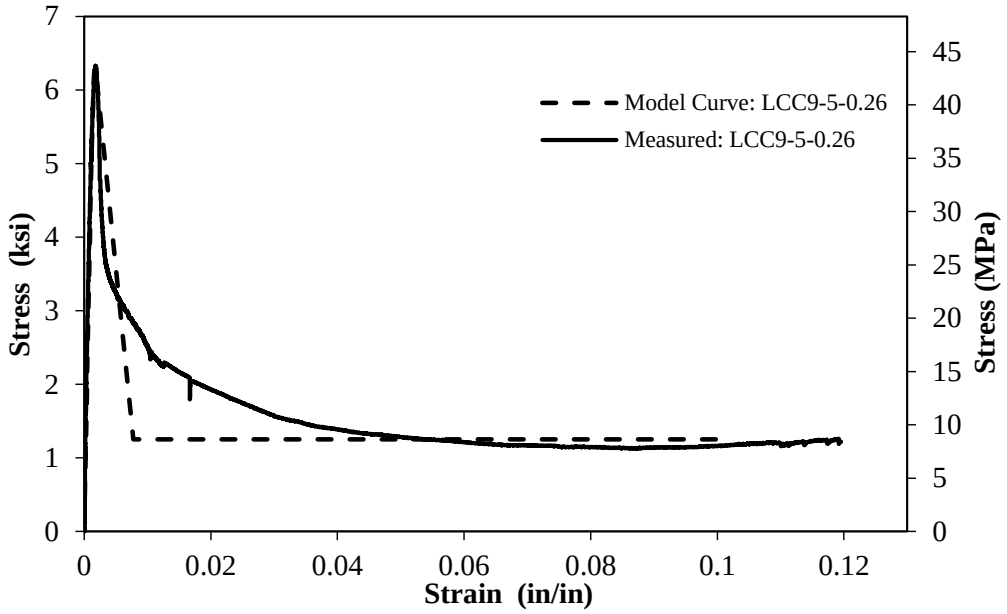

Figure 2-40. Measured and calculated (nonlinear model) stress-strain relationships for rubber confined concrete for specimen LCC9-5

2.8. Comparison with other Confinements

A reinforced concrete bridge column was selected to compare the confinement effect of the rubber with different confinement methods (Table 2-7 and Fig. 2-41). The column section was confined with a 0.5-*in.* (12.7- *mm*) thick rubber, 0.25-*in.* (6.35- *mm*) thick FRP wrap, or No. 6 spirals at 4-*in.* (101.6- *mm*) pitch, each method at a time. Engineered cementitious composite (ECC) is a type of fiber-reinforced concrete with 4% tensile strain capacity and low damage under extreme loading. Steel-confined ECC was also included in the analysis. The geometry of bridge column and the material properties are presented in Table 2.7.

Table 2-7. Column geometry and material properties

Properties	Value
Column Diameter (*in.*)	48
Column Height (*in.*)	16
Longitudinal Reinforcement	No. 9
Diameter of Longitudinal Reinforcement (*in.*)	1.128
Total Number of Longitudinal Reinforcement	22
Transverse Reinforcement	No. 6
Diameter of Transverse Reinforcement (*in.*)	0.75
Type of Transverse Reinforcement	Spiral
Pitch (*in.*)	4
Concrete Cover (*in.*)	2
Concrete/ECC Compressive Strength (*psi*)	6
Yield Strength of Steel (*ksi*)	60
Thickness of FRP, t_{frp} (*in.*)	0.25
Tensile Strength of FRP(*ksi*)	150
Modulus of Elasticity of FRP (*ksi*)	11900
Thickness of Rubber, t (*in.*)	0.50
Tensile Strength of Rubber (*psi*)	3432
Modulus of Elasticity of Rubber (*psi*)	56000

The confined properties of the section were calculated using Mander's model (Mander et al., 1988) for the steel confined concrete, Motaref's model (Motaref

Sarira, 2011) for the steel confined ECC, Lam and Tang's model (Lam & Teng, 2003) for the FRP confined concrete, and the present study for the rubber confined concrete (Fig. 2-41). The calculated mechanical properties are presented in Table 2-8. It can be seen that the peak stress and the residual strength are significantly higher for the steel and FRP confined concrete sections compared to those of the steel confined ECC and the rubber confined concrete sections. The residual strength for the steel confined ECC section is comparable to that of the rubber confined concrete section. Nevertheless, the rubber confined concrete section exhibits a strain capacity that is substantially higher than any other types of confinement method. This unique property may make this type of confinement a viable retrofit or rehabilitation method to increase the ductility of low ductile members and structure in high seismic regions. Further analytical and experimental studies are needed to show the robustness of rubber confined concrete sections for seismic or other applications.

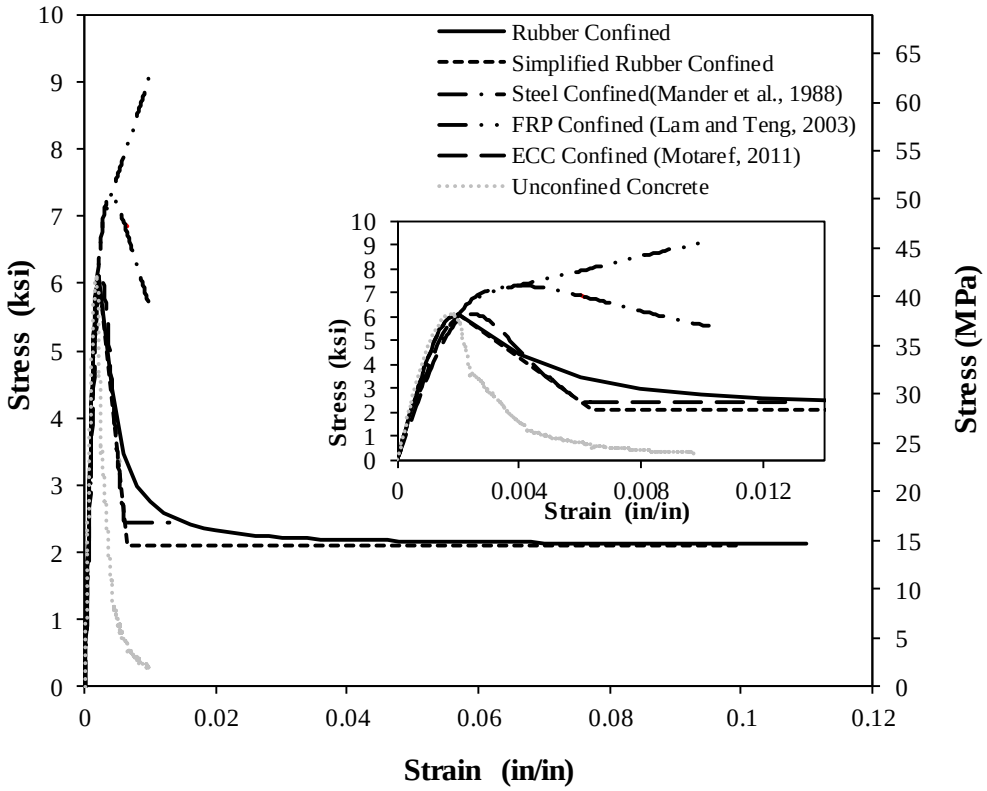

Figure 2-41. Stress-strain relationship of concrete by various confinement methods

Table 2-8. Properties of bridge column with various confinement methods

Ref.	Confining Materials	Compressive Strength, f_c' (*ksi*)	Compressive Strength of Confined Concrete, f_{cc}' (*ksi*)	Strain at Peak Stress, ε_o (*in./in.*)	Residual Strength, f_r' (*ksi*)	Strain at ultimate Stress, ε_{cu} (*in./in.*)
Present study	Rubber thickness 0.50 *in.*	6.00	6.00	0.002	2.11	0.10
Mander, et al., 1988	Steel confined #6 bar @ 4 *in.* pitch	6.00	7.85	0.00509	6.33	0.01383
Lam and Teng, 2003	FRP confined Thickness 0.25 *in.*	6.00	6.00	0.002		0.01
Motaref et al., 2011	ECC confined #6 bar @ 4 *in.* pitch	6.00	6.76	0.00336	2.71	0.01542
	Unconfined	6.00	-	0.001844		0.005

2.9. Summary and Conclusions

The main objectives of the present study was to investigate stress-strain relationship of rubber confined concrete. Total of 18 rubber confined concrete cylinders were tested under uniaxial compressive loads. The mechanical properties including stress-strain response of the rubber confined concrete was observed. Based on the experimental investigation, the following conclusions can be drawn:

- The peak stress and the corresponding strain of peak stress rubber confined concrete were approximately same, even it was same for different thickness of rubber coat.
- The residual strength of rubber confined concrete was lower than other confining materials such as steel confinement or FRP-confined concrete. However, rubber confined concrete exhibits very large strain capacity exceeding the strain capacity of reinforcing steel bar in tension.

- The average residual strength of rubber confined concrete was approximately 10 to 25% of unconfined concrete stress when thickness of rubber was varied 0.05 *in.* (1.3 *mm*) to 0.26 *in.* (*6.6 mm*). Based on past studies, it has been evaluated that the residual strength, 20 to 30% of the compressive strength of unconfined concrete, are capable to avoid catastrophic damage in seismic area, which suggest that this new rubber based confining material might be useful in seismic area.
- The proposed material model for rubber confined concrete can accurately simulate this material behavior
- Displacement ductility capacity of low-ductile bridge columns can be doubled using rubber confinement as external jacket.

Overall, it was confirmed that the strain capacity of rubber confined concrete can exceed 10%. This unique behavior of will improve displacement capacity of low-ductile concrete sections by eliminating the core concrete failure and allowing the reinforcement to reach their ultimate capacities.

2.10. References

1. ASTM Standard C39-12 (2012). "standard test method for compressive strength of cylinder concrete specimens," ASTM International , West Conshohocken, PA.
2. ASTM Standard C143 (2012). "standard test method for slump of hydraulic-cement concrete," ASTM International , West Conshohocken, PA. doi:10.1520/C0143_C0143M-12

3. ASTM Standard C617-12 (2012). "standard practice for capping cylindrical concrete specimens," ASTM International , West Conshohocken, PA.
4. Hognested, E. (1951). "A study of combined bending and axial laod in reinforced concrete memebrs; a report of an investigation conducted by the engineering experiment station," University of Illinois, Under auspices of the engineering foundation, through the reinforced concrete research council.
5. Jiang, J.-F., and Wu, Y.-F. (2012). "Identification of material parameters for Drucker–Prager plasticity model for FRP confined circular concrete columns," International Journal of Solids and Structures, 49(3), 445-456.
6. Kent, D. C., and Park, R. (1971) "Flexural members with confined concrete," Journal of the Structural Division.
7. Lam, L., and Teng, J. (2003). "Design-oriented stress–strain model for FRP-confined concrete," Construction and Building Materials, 17(6), 471-489.
8. Lim, J., and Ozbakkaloglu, T. (2014). "An accurate stress-strain model for FRP-confined concrete based on a novel approach," 23rd Australasian conference on the mechanics of structures and materials.
9. LINE-X Franchise Development Company (2016). "Technical data sheet - PX3350," LINE-X LLC, 1862 Sparkman drive, Huntsville, AL 35816.
10. LINE-X Franchise Development Company (2016). "Technical data sheet - LINE-X XPM," LINE-X LLC, 1862 Sparkman drive, Huntsville, AL 35816
11. Mander, J., Priestley, M., and Park, R. (1988). "Observed stress-strain behavior of confined concrete," Journal of structural engineering, 114(8), 1827-1849.
12. Motaref Sarira, S. M. S., and Sanders David H. (2011). "Seismic response of precast bridge columns with energy dissipating joints," Center for Civil

engineering Earthquake Research, Department of Civil and Environmental Engineering, University of Nevada, Reno, Nevada, Report No. CCEER-11-02, May 2011.

13. Nanni, A., and Bradford, N. M. (1995). "FRP jacketed concrete under uniaxial compression," Construction and Building Materials, 9(2), 115-124.
14. Popovics, S. (1973). "A numerical approach to the complete stress-strain curve of concrete," Cement and concrete research, 3(5), 583-599.
15. Samaan, M., Mirmiran, A., and Shahawy, M. (1998). "Model of concrete confined by fiber composites," Journal of structural engineering, 124(9), 1025-1031.
16. Spoelstra, M. R., and Monti, G. (1999). "FRP-confined concrete model," Journal of composites for construction, 3(3), 143-150.
17. Torrenti, J., Benaija, E., and Boulay, C. (1993). "Influence of boundary conditions on strain softening in concrete compression test," Journal of engineering mechanics, 119(12), 2369-2384.
18. Van Mier, J. G. M. (1984). "Strain-softening of concrete under multiaxial loading conditions," Technische Hogeschool Eindhoven.
19. Wu, Y.-F., Liu, T., and Oehlers, D. J. (2006). "Fundamental principles that govern retrofitting of reinforced concrete columns by steel and FRP jacketing," Advances in Structural Engineering, 9(4), 507-533.
20. Wu, Y.-F., and Wei, Y. (2014). "General stress-strain model for steel-and FRP-confined concrete," Journal of composites for construction, 19(4), 04014069.

CHAPTER 3. BUCKLING RESTRAINED REINFORCEMENT

3.1. Introduction

Reinforced concrete (RC) bridges and buildings are currently designed to exhibit large displacement capacities in high seismic region through yielding of reinforcements. However, repair of ductile components is often inevitable under strong earthquakes mainly because of concrete failure, significant yielding of reinforcement, or large residual lateral deformations. Repair of RC structures is extremely difficult or impractical when longitudinal reinforcement of ductile members fractures. In this case, the structure needs to be demolished and reconstructed.

External steel bars has been proposed in previous studies to mainly increase energy dissipation of rocking columns and frames. With some modification in construction detailing, external energy dissipaters might be used as longitudinal reinforcement of RC sections. With proposed detailing, damaged reinforcement can be simply replaced after earthquakes. Therefore, RC structures can be repaired in a few hours after an event without the need of total replacement of the structure. Feasibility and performance of a new type of external energy dissipater, which is

referred to as “buckling restrained reinforcement (BRR)” in the present study, are investigated in this chapter.

3.2. Research Objectives

Dog-bone mild steel or aluminum bars encased in steel tubes were used in previous studies to enhance the energy dissipation of rocking structures. Conventional deformed steel bars without any reduction of the section enclosed in steel pipes were proposed in the present study as external energy dissipaters. The use of original reinforcement in BRR will save time and money compared to dog-bone energy dissipaters due to machining. The main objective of this study was to experimentally investigate the feasibility and performance of conventional reinforcing steel bars in BRR.

3.3. Buckling Restrained Reinforcement (BRR)

A non-conventional type of structural system, rocking, allows structural members to rock and return to its original position after an event incorporating post-tensioning tendons. When an internal or external energy dissipater is added to rocking elements to enhance energy dissipation and to reduce displacements, it is called “hybrid rocking members. Figure 3-1a shows the hysteretic behavior for a conventional ductile column in which loops are fat because of large energy dissipation through yielding of reinforcement with significant residual displacements. A simple rocking system (no energy dissipater) shown in Fig. 3-1b exhibit self-centering behavior but minimal energy dissipation and excessive lateral displacements under earthquakes. A hybrid rocking column (Fig. 3-1c) with flag-shape hysteresis exhibits self-centering behavior and displacements that can meet the current code deformation requirements.

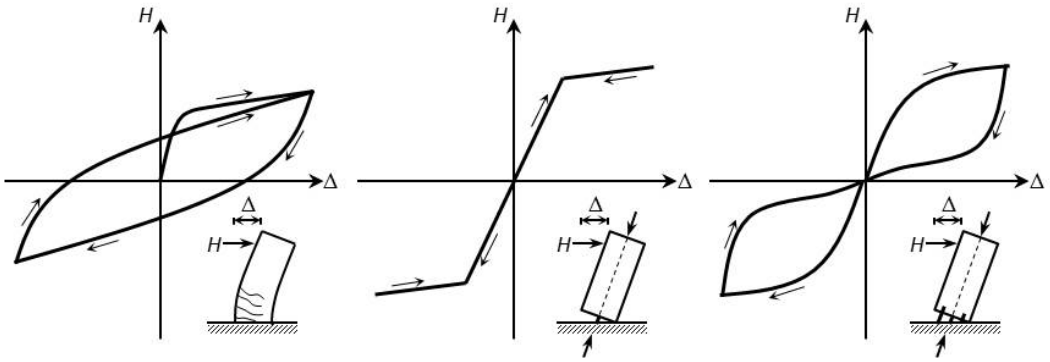

(a) Conventional Detailing (b) Simple Rocking (c) Hybrid Rocking

Figure 3-1. Hysteretic behavior of concrete columns (Guerrini et al., 2015)

In hybrid rocking columns (or structures in general), energy can be dissipated using internal (e.g. longitudinal reinforcement as shown in Fig. 3.2a) or external devices (Fig. 3-2b). External dissipaters provide an additional benefit of possible replacement after severe events, if damaged.

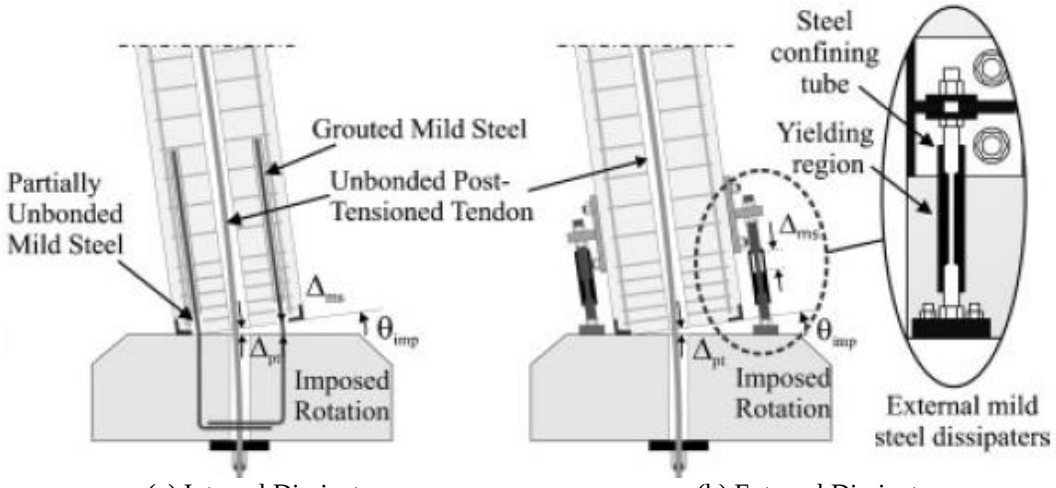

(a) Internal Dissipater (b) External Dissipater

Figure 3-2. Energy dissipaters for rocking systems (Marriott et al., 2011)

3.4. Past Research on External Energy Dissipaters

3.4.1. Introduction

Dog-bone mild steel or aluminum bars enclosed in steel tubes (Fig. 3-2) were used in previous studies as external energy dissipaters to reduce deformation of rocking components during earthquake excitation. Tubes were filled with either a

grout or epoxy, or were not filled. Reinforcement are enclosed in tubes to prevent buckling. In conventional reinforced concrete structures, concrete surrounding the reinforcement prevents buckling. Capacities of this device mainly depends on the bar properties and their geometry. With a proper design, buckling of the tube/grout/reinforcement will be the main failure mode of the external energy dissipaters. Sometimes fracture may occurred in dog-bone bars after many cycles because of low effective slenderness ratio (25.7) of fuse bar (Sarti et al., 2016). However, the failure mechanism can be controlled by changing the slenderness ratio of dog-bone bars, lengths, and dog-bone bar diameter verse that of the unreduced bar.

3.4.2. External Energy Dissipaters

A limited number of dog-bone shape external energy dissipaters were tested in previous studies (Guerrini et al., 2014; Marriott et al., 2009; Mashal et al., 2014; Mesa and Dario, 2010; Sarti et al., 2016; White and Palermo, 2016) mainly for hybrid rocking columns. A brief review of all past studies are discussed herein.

3.4.2.1. Study by Marriot et al. (2009)

Marriott et al. (2009) used twelve external energy dissipaters in hybrid bridge piers. Three different fuse lengths of 75, 75, and 115 *mm* by following fuse diameters of 13.5, 10.0, and 8.0 *mm*, respectively were used to prepare the dissipaters. Fuse is referred to the portion of the external energy dissipater in which section was reduced. A 34-*mm* long steel tube with a wall thickness of 2 *mm*, was used to enclose reinforcement. Subsequently, tube was filled with epoxy. Prior to their installation within bridge pier, the individual dissipaters were tested subjected to cyclic, axial, tension-compression tests to observe their cyclic energy dissipation and stability. This test was conducted particularly to investigate the anti-buckling system. The

dissipater was capable to provide a large amount of energy dissipation. Moreover, pinching was not observed during test and the response was very stable, indicating that large inelastic cycles can be achieved without buckling of reinforcement. It was also reported that when the bar is under large compressive deformation, the gap between the grout and the unreduced portion of the bar (Fig. 3-3b) was closed resulting in higher stiffness in compression than that in tension.

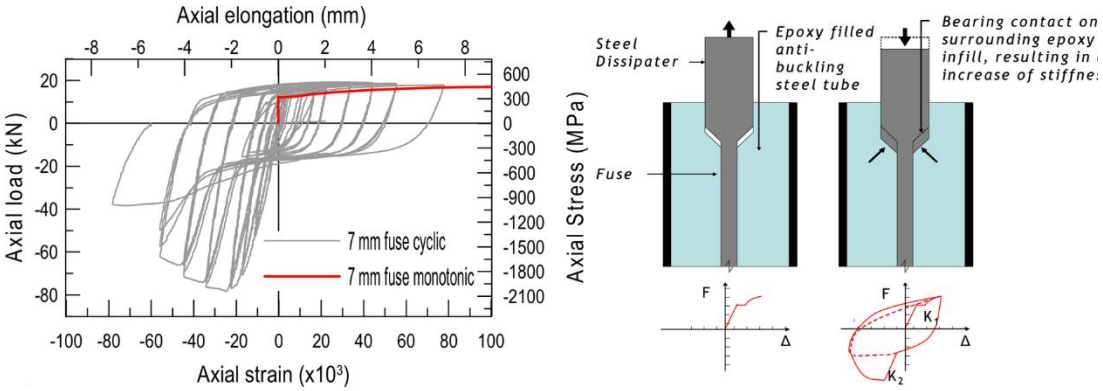

(a) Cyclic and monotonic behavior of dissipater (b) Compression behavior of dissipater

Figure 3-3. Cyclic behavior of external energy dissipater (Mesa and Dario, 2010)

3.4.2.2. Study by Mesa and Dario (2010)

Mesa and Dario (2010) tested three different types of external energy dissipaters similar to those shown in Fig. 3-3 with diameters of 7, 10, 13 *mm* and a fuse length of 90 *mm*. A steel tube with external diameter of 34 *mm* and a wall thickness of 3 *mm*, was used as confining tube. Figure 3-4 shows the stress-strain / force-displacement response for the 7 mm and 8 mm fuses incorporate with an unbonded length of 150 *mm*. The test was carried out for the monotonic uniaxial and cyclic loading. The dissipater failed at an elongation of 14 *mm* and 16 *mm* corresponding to a 9% and 11% of the axial strain for 7-*mm* and 8-*mm* fuses, respectively. The dissipaters show a reduction of the yield plateau under cyclic loading and increase of the yield strength due to strain rate effects under monotonic

and cyclic loading. Both dissipaters were failed at similar elongation, which is concluded that the level of elongation mainly controlled by the unbonded length of dissipaters.

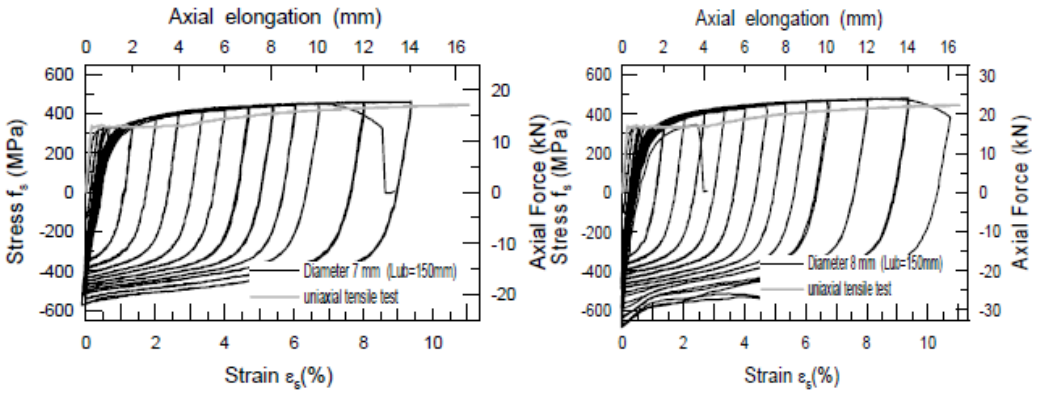

Figure 3-4. Stress-strain and force displacement relationship of the external dissipaters (Mesa and Dario, 2010)

3.4.2.3. Study by Mashal et al. (2014)

Mashal et al. (2014) investigated the seismic performance of hybrid rocking bridge columns using fuse-type external energy dissipaters. However, detailing and test results for the dissipaters were not published because of patenting. However, they experimentally showed that hybrid rocking bridge columns with external dissipaters exhibited no damage and zero residual displacements up to 3% drift ratio, where test was stopped.

3.4.2.4. Study by Guerrini et al. (2014)

Guerrini et al. (2014) incorporated buckling restrained energy dissipaters in a column test. Dog-bone hot-rolled A576 Grade 1018 steel bars with the yield strength of 331 *MPa*, ultimate strength of 190 *MPa*, and a strain of 23% at the peak stress were used as external energy dissipaters. The machined portion of the bars was enclosed by a steel tube and grouted to prevent buckling (Fig. 3-5). The bars were lubricated

inside tubes to minimize the friction between steel bars and grout, and mastic tape was used at the tapered portion of the bars to minimize the bearing and to provide a gap between the bar and the filler material. The stress-strain hysteresis of one of the external dissipaters is shown in Fig. 3-6. It was reported that due to partial composite action between the bar, filling material, and steel tube, the peak compressive stress was larger than the peak tensile stress.

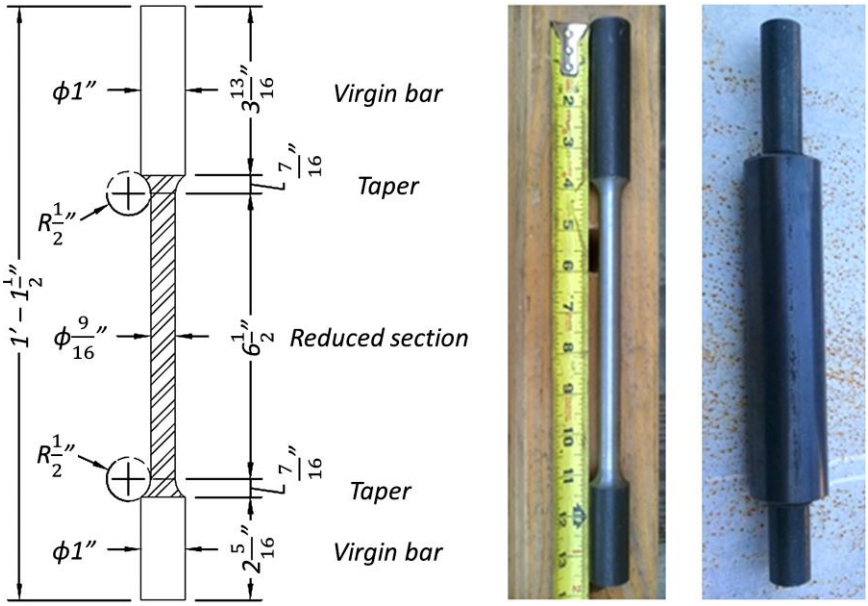

Figure 3-5. Geometric configuration for buckling restrained energy dissipaters (Guerrini et al., 2014)

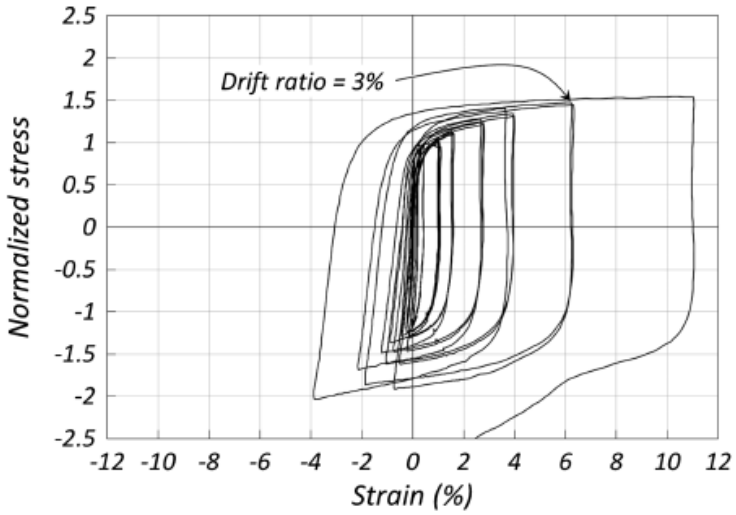

Figure 3-6. Hysteretic behavior of buckling restrained energy dissipaters (Guerrini et al., 2014)

3.4.2.5. Study by Guo et al. (2015)

Goo et al. (2015) carried out an experimental study on hybrid rocking bridge piers externally reinforced with aluminum energy dissipaters. Each bar had a diameter of 25 *mm* and the diameter was machined down to 15 *mm* at the middle of bar. The fuse length was 100 *mm* for all of test specimens but one, which had a fuse length of 200 *mm*. This energy dissipater was not individually tested under direct axial loads but was used in bridge column tests (Fig. 3-7). It was found that aluminum energy dissipaters are a viable type of energy dissipater.

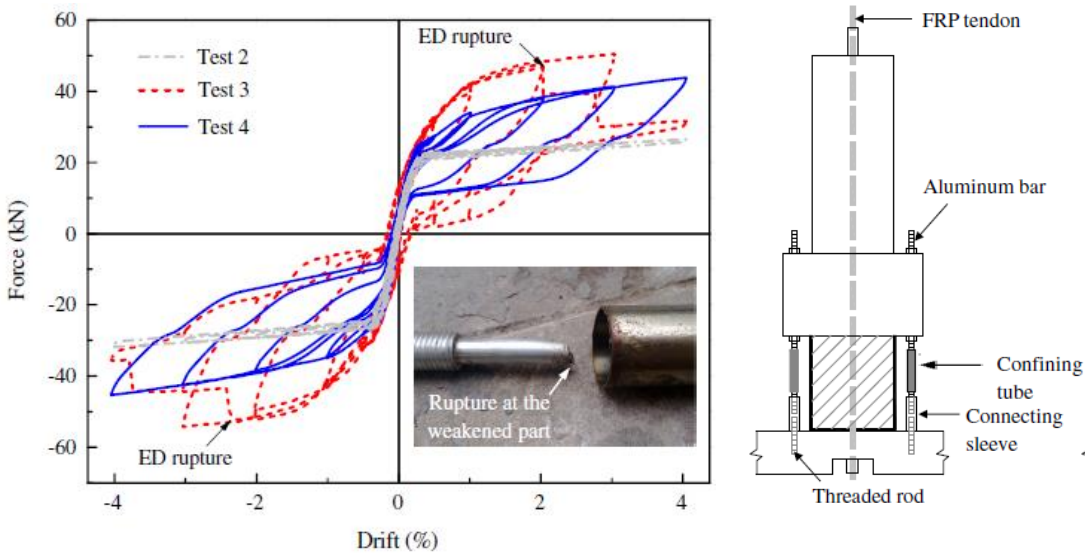

(a) Hysteretic behavior (b) Bridge pier with dissipater

Figure 3-7. Hysteretic behavior of external energy dissipaters constructed with aluminum bar (Guo et al., 2015)

3.4.2.6. Study by White and Palermo (2016)

White and (2016) used external energy dissipater in hybrid rocking bridge column to observe the structural behavior of bridge pier through experimental investigation. These dissipaters were fabricated using 30-mm Grade 300 steel bars machined down to a diameter of 24 *mm* at the middle as shown in Fig. 3-8. Two cross sections were proposed for the reduced portion of the bar: circular and grooved.

Grooved sections provide higher radius of gyration compared to circular sections resulting in a better resistant against buckling. This study did not provides test results for individual energy dissipaters.

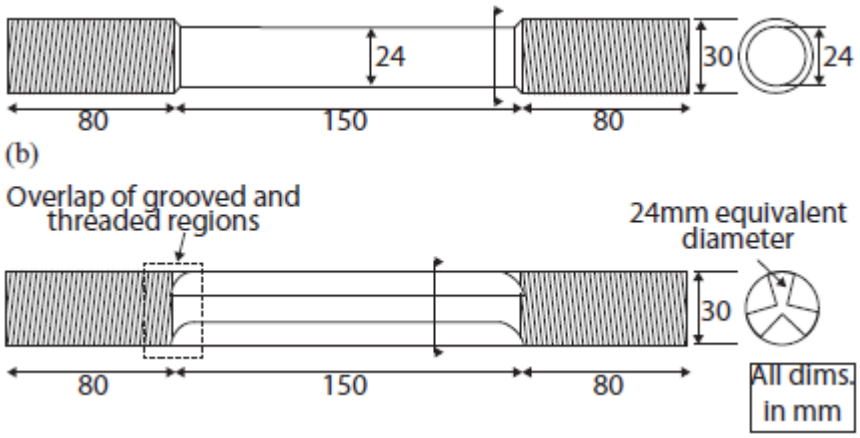

Figure 3-8. Geometric configuration of external energy dissipaters (White & Palermo, 2016)

3.4.2.7. Study by Sarti et al. (2016)

Sarti et al. (2016) tested six dog-bone buckling-restrained mild steel dissipaters for different geometric parameters (Fig. 3-9). Grade 300 steel bars with the yield strength of 300 *MPa* and AS/NZS 1163 grade C250L0 tubes were used to form dissipaters. Either grout or epoxy was used to fill the tubes. This test was conducted to investigate the failure mechanism of dissipater's based on their geometric configuration. It has been observed that the dissipaters showed a significant improvement of stiffness under negative displacement, which is indicated that the external energy dissipaters are very good in compression. Axial testing of these dissipaters showed that stable hysteresis loops can be achieved with the average strain capacity of 6%. Two different failure modes were observed: (1) low-cycle fatigue in specimens with low effective slenderness ratio (25.7) by bar fracturing in the reduced-diameter portion of the dissipater, and (2) buckling of tube. The effective

slenderness ratio is defined by an equation, which is depend on the fuse length, area and second of moment of inertia of fuse bar and confining tube. The device showed higher forces in compression when the tube buckled due to composite action of the tube/grout/bar system in compression. It was also observed the filling materials, grout or epoxy, do not affect the overall behavior of the dissipaters. Based on an analytical study, a fuse slenderness ratio of 60 or lower was recommended.

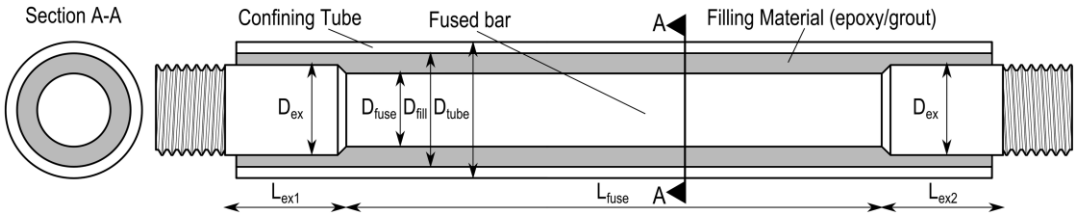

Figure 3-9. Geometric configuration for dog-bone energy dissipaters (Sarti et al., 2016)

3.4.3. Use of External Energy Dissipaters in Concrete Elements

The performance of hybrid rocking concrete elements (post-tensioning tendons and a type of energy dissipater) has been investigated in previous studies. The main focus of recent studies has been on the development of hybrid rocking elements (mainly columns) with the use of external energy dissipaters to control displacement demands of the member in high seismic region. A brief review of recent studies with external energy dissipaters in presented herein.

3.4.3.1. Study by Guerrini et al. (2014)

Guerrini et al. (2014) tested one dual-shell cantilever hybrid rocking bridge column incorporated with external energy dissipaters. The column was designed for a target drift ratio of 3%. The drift ratio is defined as the ratio of the column tip lateral displacement to the column length. Six external buckling-restrained energy dissipaters were mounted to control displacements. The energy dissipaters were

design not to fracture at the target drift ratio and the post-tensioning bars were expected to remain elastic. An axial load of 63 *kips* were applied to the column using two vertical hollow hydraulic jacks. Subsequently, the column was tested under, subjected to quasi-static reversed cyclic loading. Buckling of the external energy dissipaters were observed at 3% drift ratio. One dissipater fractured at the first cycle 7.5% drift ratio and two dissipaters fractured under subsequent cycles. The test was stopped at 10% drift ratio. Figure 3-10 shows the hysteretic behavior of dual-shell hybrid rocking bridge column mounted by external energy dissipaters.

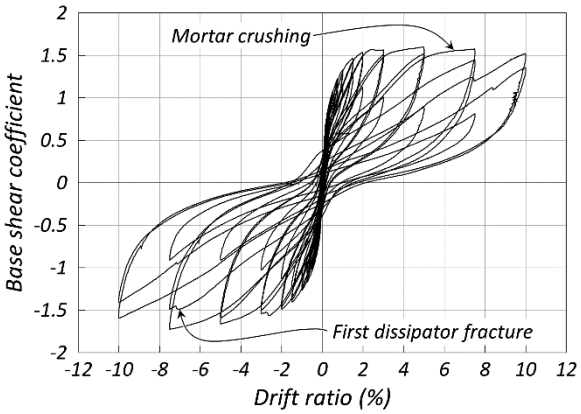

(a) Hysteretic lateral force-displacement response

(b) Bridge column incorporate with external energy dissipater

Figure 3-10. Structural behavior of dual-shell hybrid rocking bridge column under reverse cyclic loading (Guerrini et al., 2014)

3.4.3.2. Study by Marriott et al. (2009)

Marriott et al. (2009) tested one conventional RC bridge column as well as one hybrid rocking bridge column reinforced with eight external energy dissipaters. Both columns were tested under pseudo-dynamic loading protocols. The axial load for both columns was 300 *kN*. The test results confirmed satisfactory performance for external energy dissipaters and the post-tensioning tendons up to 3.5 % of drift ratio where the test was stopped. The hybrid rocking column exhibited good energy

dissipation and re-centering characteristics. Since the column plastic hinge region was jacketed with steel tube, the column damage was insignificant.

3.4.3.3. Study by Marriott et al. (2011)

Marriott et al. (2011) tested bridge columns with the same detailing as those described in the previous study (Marriott et al., 2009) but subjected to biaxial loading. For the conventional bridge column, concrete spalling was observed at 2% drift ratio, first reinforced buckled at 2.5% drift ratio followed by strength degradation and bar fracture at higher drift ratios. On the other hand, the hybrid bridge column exhibited minimal damage and stiffness and strength degradation up to 2.5% drift ratio at which one dissipater ruptured.

3.4.3.4. Study by Guo et al. (2015)

Guo et al. (2015) tested three 1/3-scale hybrid bridge columns reinforced with external energy dissipaters under cyclic loading. Aluminum bars instead of mild steel bars were used in external energy dissipaters because of their lower costs and better corrosion resistance. Minimal damage was observed in the hybrid rocking columns at 4% drift ratio while the conventional RC specimen significantly damaged with large residual drifts at 2.25% peak drift ratio. Even though a few of the dissipaters ruptured at large drift cycles, the column exhibited large energy dissipation.

3.4.3.5. Study by Mashal et al. (2014)

Mashal et al. (2014) tested low-damage hybrid rocking two-column bents under cyclic loading. External energy dissipaters were used to control displacements. Steel jacket was used to confine the columns and to attach the dissipaters. Total 390 kN axial loads were applied on column head during test. The test results confirmed

low damage, high energy dissipation, and low residual displacement up to 3.5 drift ratio where the test was stopped. Figure 3-11 shows the structural behavior of ABC low-damage and high-damage bridge column under cyclic loading mounted with external energy dissipater. There was no damage observed in bent after testing the specimen.

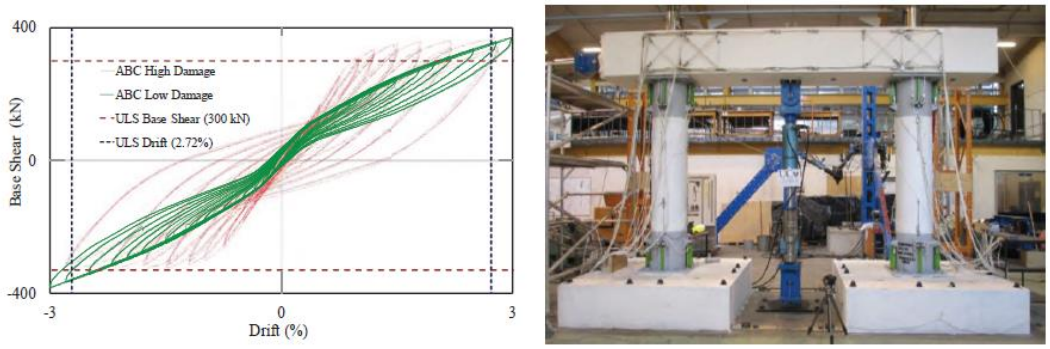

(a) Force – displacement response (b) bent after testing

Figure 3.11. Force-displacement relationship of ABC low-damage and high-damage bridge piers (Mashal et al., 2014)

3.4. Experimental Program

3.4.1. Introduction

Dog-bone energy dissipates showed promising performance in the previous studies as discussed in the previous section. In an attempt to avoid bar machining, straight un-reduced reinforcing steel bars, which is referred to as buckling restrained reinforcement (BRR) in this chapter, were recommended as external energy dissipaters (Fig. 3-12). To investigate the feasibility and performance of BRR, nine buckling specimens were tested in the Lohr Structures Laboratory at South Dakota State University under axial compressive loading. Detailing, testing procedure, and a summary of the BRR test results are presented in this section.

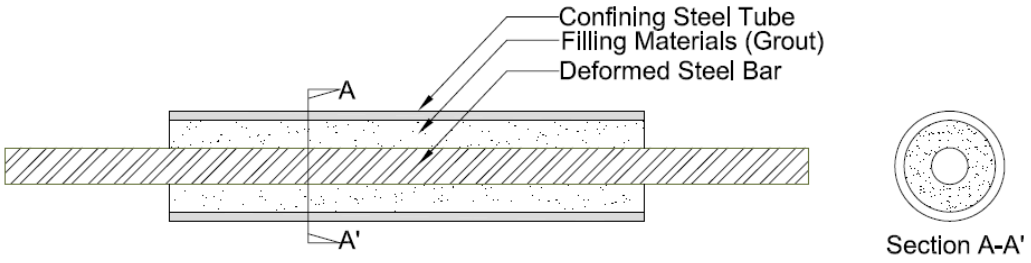

Figure 3-12. Geometric configuration of Buckling Restrained Reinforcement

3.4.2. Test Matrix

A total of 16 specimens (Table 3-1) including four reference deformed bars, three deformed bars restrained with steel nuts, and nine buckling restrained reinforcement (BRR) were constructed and tested under monotonic and cyclic axial compressive loading to failure. Two different sizes of deformed steel bar, No. 4 and No. 8, were used in this experimental investigation. Steel tubes with different geometry were used to prevent buckling of reinforcement and were filled with non-shrink grout. Note that reinforcing steel bars were not machined.

Table 3-1. Test matrix for Buckling Restrained Reinforcement

Specimen ID	Reinforcing Steel Bar		Steel Tube			Filling Material	Load
	Size (No.)	Length (*in.*)	O.D. (*in.*)	Gage	Length (*in.*)		
No4-BL11.00d	4	11.00					Monotonic
No4-BL10.94d	4	11.00					Monotonic
No8-BL16.91d	8	16.96					Monotonic
No8-BL10.25d	8	10.25					Monotonic
No4-BL11.00d-Nuts-G0.875	4	11.00					Monotonic
No4-BL11.00d-Nuts-G0.42	4	11.00					Monotonic
No4-BL11.00d-Nuts-G0.20	4	11.00					Monotonic
No4-BL11.00d-TL5.0s-TG18-G2.00	4	11.00	1 ¼	18 GA	5	Grout	Monotonic
No4-BL10.94d-TL5.0s-TG16-G1.94	4	10.94	1 ¼	16 GA	5	Grout	Monotonic
No4-BL12.28d-TL7.5s-TG16-G0.50	4	12.06	1 ¼	16 GA	7.5	Grout	Monotonic
No4-BL12.20d-TL7.5s-TG14-G0.50	4	12.20	1 ¼	14 GA	7.5	Grout	Monotonic
No4-BL14.81d-TL7.5s-TG14-G0.50	4	14.81	1 ¼	14 GA	10	Grout	Monotonic
No4-BL14.81d-TL7.5s-TG13-G0.50	4	14.81	1 ¼	13 GA	10	Grout	Cyclic
No8-BL14.56d-TL10.0s-TG13-G0.50	8	14.56	2 ¼	13 GA	10	Grout	Monotonic
No8-BL17.00d-TL10.0s-TG11-G1.00	8	17.00	2 ¼	11 GA	10	Grout	Monotonic
No8-BL19.62d-TL15.0s-TG11-G0.50	8	19.62	2 ¼	11 GA	15	Grout	Monotonic

Example of Specimen Identification: No4-BL10.94d-TL5.0s-TG16-G0.5
No4: No. 4 Reinforcing Bar
BL10.94d: Length of Reinforcing Bar = 10.94 in.; Bar Type d= Deformed, p= Plain
TL5.0s: Length of Tube = 5.0 in.; Tube Type s= steel, a=Aluminum
TG16: Tube Gage = 16
G0.5: Total Gap = 0.5 in.

3.4.3. Material Properties

3.4.3.1. Steel Tube

Tubes enclosing reinforcing bars were made of Grade 1026, carbon steel. Two different tubes diameters with different wall thickness (Table 3-1) were considered to investigate the behavior of BRR. The mechanical properties of steel tube are presented in Table 3-2.

Table 3-2. Mechanical properties of steel tube in BRR

	Yield Strength (*psi*)	Ultimate Tensile Strength (*psi*)	Elongation (%)	Hardness (HRB)
Min	66,000	75,000	10.00	80.00
Max	73,546	86,524	20.00	91.00

3.4.3.2. Reinforcing Steel Bar

ASTM A706, Grade 60, deformed steel bars were used in BRR. Two different diameters and various lengths were included to optimize the performance of BRR. The expected mechanical properties of reinforcing steel bars according to AASHTO Seismic Guide Specifications are presented in Table 3-3. Measured strengths are presented in the following sections.

Table 3-3. Mechanical properties of reinforcing steel bars

Property of ASTM A706	Value
Grade	60
Yield Stress, f_y (*ksi*)	60
Modulus of Elasticity, E_s (*ksi*)	29000
Expected Yield Stress, f_{ye} (*ksi*)	68
Ultimate Tensile Strength, f_u (*ksi*)	95
Expected Yield Strain, ε_{ye} (*in.*)	0.0023
Ultimate Strain, ε_u (*in./in.*)	0.09

3.4.3.3. Non-Shrink Grout

Conventional non-shrink fine-aggregate high-flow grout (1428 HP) was used to fill the gap between reinforcing bars and steel tubes. This main purpose of using

the grout is to increase the moment of inertia of the device and to enhance durability of reinforcement. The grout use was a non-metallic, mineral-based precision grout designed to have high initial and ultimate strengths. The expected compressive strength provided by the manufacturer is presented in Table 3-4.

Table 3-4. Strength of non-shrink grout at different conditions.

Age	Condition		
	Plastic	Flowable	Fluid
1 day	6,500 *psi*	5,500 *psi*	4,500 *psi*
3 days	8,000 *psi*	7,000 *psi*	6,000 *psi*
7 days	10,000 *psi*	9,000 *psi*	8,000 *psi*
28 days	14,000 *psi*	12,000 *psi*	10,000 *psi*

3.4.4. Construction of Buckling Restrained Reinforcement (BRR)

Buckling restrained reinforcement (BRR) were fabricated at the Lohr Structures Laboratory at South Dakota State University (Fig. 3-12 and Fig. 3-13). The test specimens were assembled and installed on a vertical support. The bottom of specimens were sealed by a duct tape to prevent grout leak. Figure 3-14 shows the specimens after pouring the non-shrink grout from the top. The test specimens were removed after 28 days and placed in lab at room temperature.

Figure 3-13. Construction of BRR specimens

Figure 3-14. BRR specimens after pouring non-shrink grout

3.4.5 Test set up and Loading Protocol

Three ASTM A36 steel plates each with a thickness of 1 *in.* (25 *mm*) connected with four post-tensioning rods were utilized in a self-reacting compressive setup (Fig. 3-15 and 3-16). Steel cups at the center of the two steel plates were to

hold the specimens and to ensure that the specimen are secure during the compressive test. A hydraulic hallow-core jack was used to apply compressive monotonic and cyclic loads and was controlled with a manual oil pump. The average displacement rate was 0.0052 *in./sec* (0.13 *mm/sec*). Four load cells and three string potentiometers were used to measure forces and displacements of BRR, respectively.

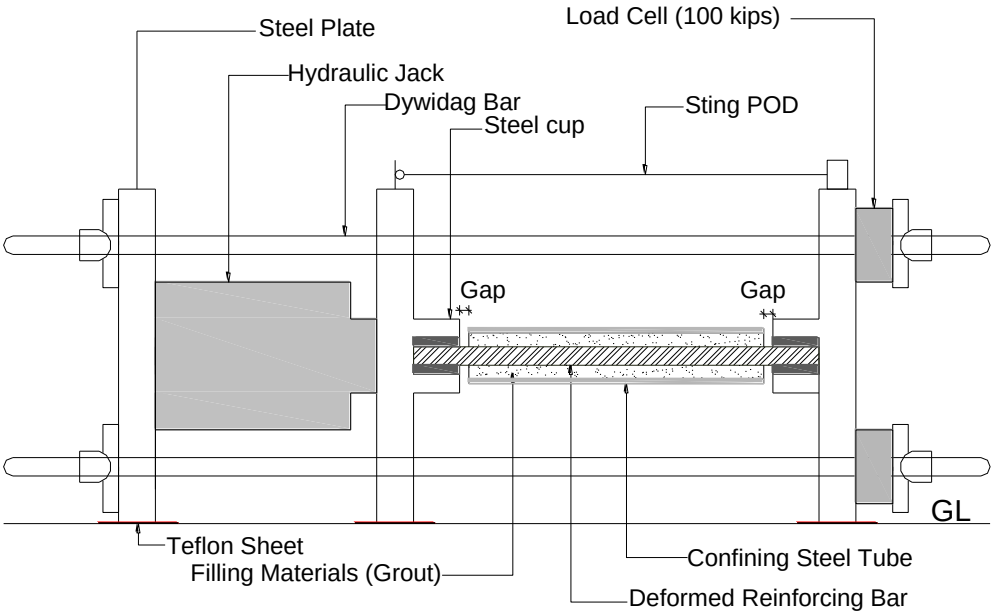

Figure 3-15. Schematic Elevation view of BRR test setup

Figure3-16. Photograph of BRR test setup

3.5. Experimental Results

The main objective of this research was to investigate the mechanical properties and the failure mechanism of BRR. A summary of test data is presented herein.

3.5.1. Material Properties

The compressive strength of 2-*in.* (51- *mm*) grout cubes tested according to ASTM Standard C39-12 (2012) at different ages is presented in Table 3-5.

Table 3-5. Measured compressive strength of non-shrink grout

Age (days)	Compressive Strength, f'_{cg} (*psi*)
7	6,210
14	7,750
28	9,850
50	10,180

Note: Three samples were tested. Only the average strength was reported.

3.5.2 Performance of Buckling Restrained Reinforcement

3.5.2.1. Failure Mechanism

Figure 3-17a shows the failure of a reference No. 4 deformed bar with a total length of 11 in. (22 times the bar diameter) under compression in which the No. 4 bar buckled at a 23.45 *ksi* (161.7 *MPa*) compressive stress. In an attempt to improve the buckling resistance of bars, No. 4 bars were enclosed in conventional steel nuts (Fig. 3-17b to 3-17d). The only variable was the total gap between the nuts and the face of the steel caps in the axial direction. Three gaps were $1.75d_b$, $0.85d_b$, and $0.4d_b$ (d_b is the diameter of the bar). The compressive behavior of a BRR will be the same as that of a conventional steel bar before the gap closure. It was found that a reinforcing steel bar can fully resist against buckling and the compressive strength can exceed the

yield strength of the bar if the total gap does not exceed $0.5d_b$. Bar buckling at small stresses was observed when the gap was higher (Fig. 3-17b and Fig. 3-17c).

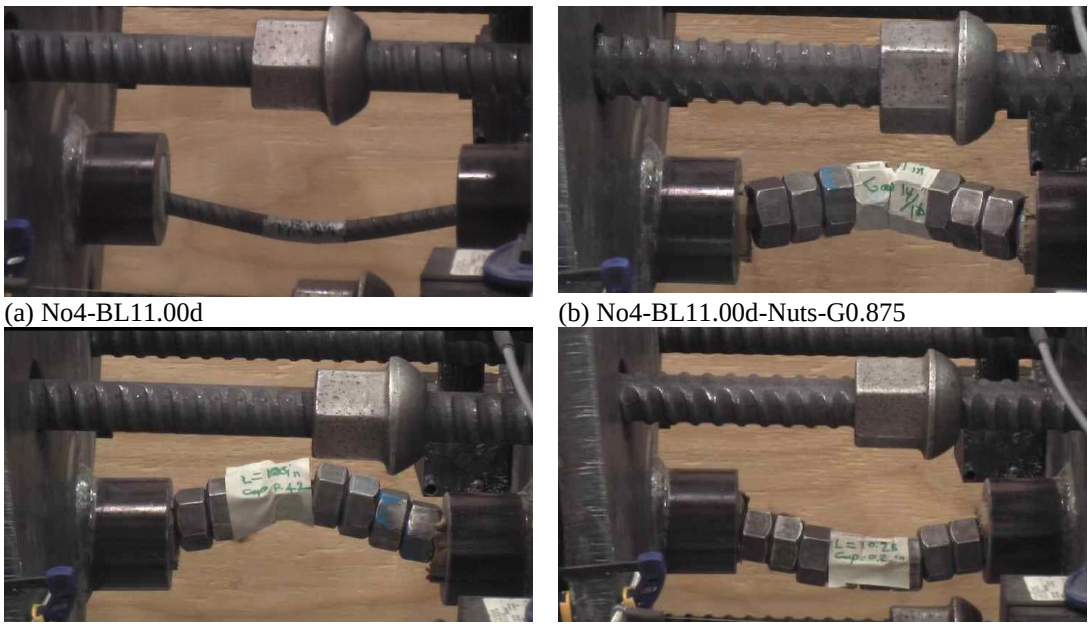

(a) No4-BL11.00d (b) No4-BL11.00d-Nuts-G0.875

(c) No4-BL11.00d-Nuts-G0.42 (d) No4-BL11.00d-Nuts-G0.20

Figure 3-17. Failure of deformed reinforcing bars with and without steel nuts

Figure 3-18 shows the failure mode of the nine BRR specimens under compressive loads. For No. 4 BRRs, the device buckled at very large stresses [200 *ksi* (1379 *MPa*)] when the total axial gap between the tube and the cup was not more than $0.5d_b$. Similar to No. 4 BRRs, No. 8 BRRs showed large compressive stresses before failure when the total axial gap was $0.5d_b$.

(a) No4-BL11.00d-TL5.0s-TG18-G3.0

(b) No4-BL10.94d-TL5.0s-TG16-G2.94

(c) No4-BL12.20d-TL7.5s-TG14-G0.5

(d) No4-BL12.28d-TL7.5s-TG16-G0.29

(e) No4-BL14.81d-TL7.5s-TG13-G0.5

(f) No4-BL14.81d-TL7.5s-TG14-G0.5

(g) No8-BL17.00d-TL10.0s-TG11-G1.0

(h) No8-BL14.56d-TL10.0s-TG13-G0.5

(i) No8-BL19.62d-TL15.0s-TG11-G0.5

Figure 3-18. Failure of BRR specimens

3.5.2.2. Stress-Strain Relationship

Figure 3-19 shows the stress-strain relationship of unrestrained deformed steel bars under monotonic compressive loads. The measured peak stresses are presented in Table 3-6. It can be seen that unrestrained steel bars will buckle under low compressive stresses.

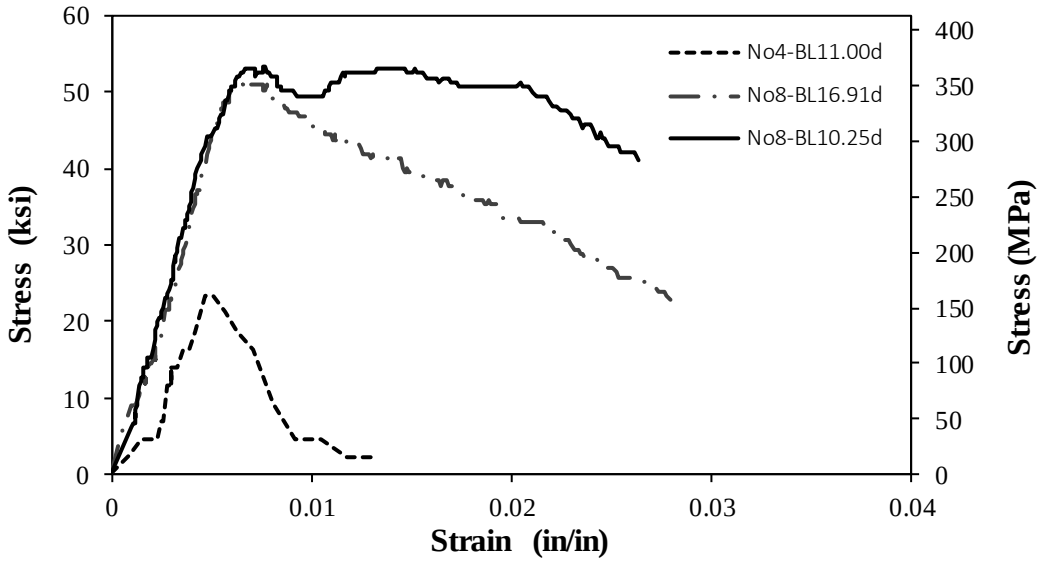

Figure 3-19. Stress-strain relationship for deformed reinforcing bars

Table 3-6. Stress-strain characteristics of deformed reinforcing bars under compressive loads

Specimen ID	Unrestrained Length to Diameter (*in.*)	Peak Stress (*ksi*)	Peak Strain (*in./in.*)
No4-BL11.00d	14	23.45	0.005
No4-BL10.94d	13.88	21.06	0.003
No8-BL16.91d	12.91	51.48	0.007
No8-BL10.25d	6.25	53.19	0.008

Figure 3-20 shows the compressive stress-strain relationship of reinforcing steel bars restrained against buckling with steel nuts. Table 3-7 presents the peak values. It can be seen that large stresses even greater than the ultimate compressive strength of the bar can be achieved when the total axial gap between the nuts and the steel cup was less than 0.5 times the bar diameter. The stress was higher than the

reinforcement ultimate strength since the gap was closed and the nuts were engaged in compression. The strain at the peak stress was approximately 3%.

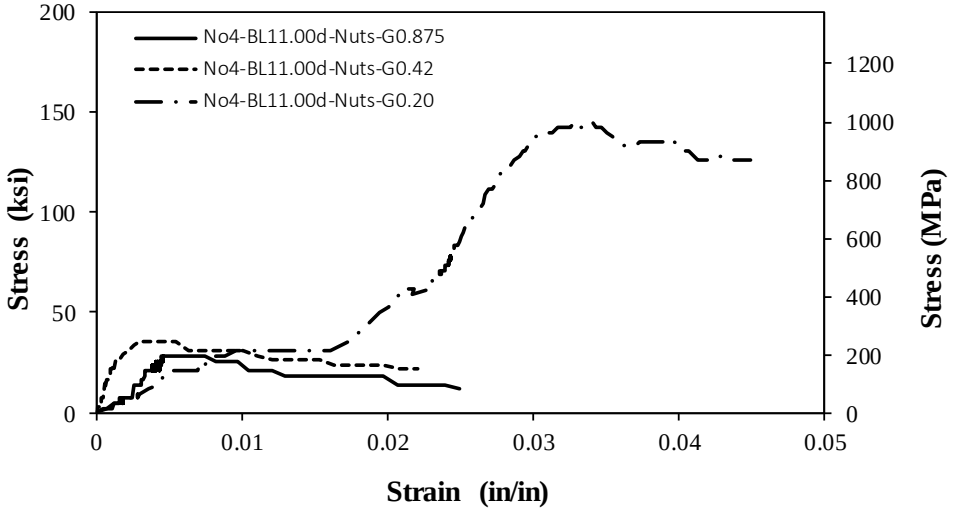

Figure 3-20. Stress-strain relationship of deformed reinforcing bars with nuts

Table 3-7. Stress-strain characteristics of deformed reinforcing bars enclosed in nuts

Specimen ID	Axial Gap	Peak Stress (*ksi*)	Peak Strain (*in./in.*)
No4-BL11.00d	$14d_b$	23.45	0.005
No4-BL11.00d-Nuts-G0.875	$1.75d_b$	28.14	0.005
No4-BL11.00d-Nuts-G0.42	$0.85d_b$	40.46	0.034
No4-BL11.00d-Nuts-G0.20	$0.4d_b$	144.71	0.034

Figure 3-21 shows stress-strain relationships of all BRR specimens. Table 3-8 presents a summary of the test results. It can be seen that with proper detailing (e.g. total axial gap, tube diameter and wall thickness), it is possible to achieve large stress and strain capacities for the proposed buckling restrained reinforcement. The compressive stress of BRR can exceed the ultimate strength of the bar because of the contribution of the tube/grout after the gap closure. The compressive strain at the peak stress can exceed 5%, which will be sufficient in most practical cases since the strain of compressive reinforcement in a concrete section is usually controlled by the core concrete strains. The core concrete strain capacity even in a highly confined section does not exceed 5%.

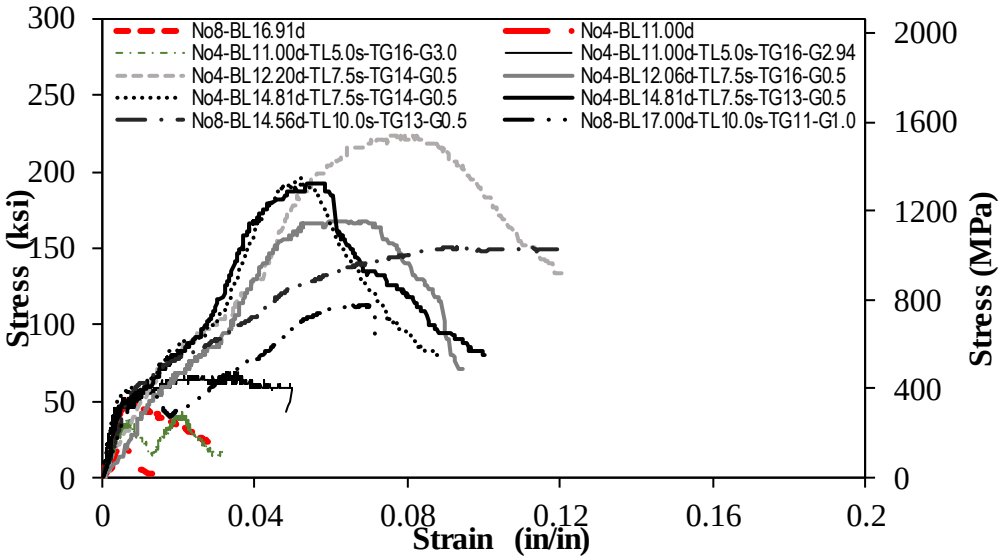

Figure 3-21. Stress-strain response of all BRR devices

Table 3-8. Stress-strain characteristics of BRR

Specimen ID	Axial Gap	Peak Stress (*ksi*)	Peak Strain (*in./in.*)
No4-BL11.00d-TL5.0s-TG18-G3.0	$6.00d_b$	42.46	0.021
No4-BL11.00d-TL5.0s-TG16-G2.94	$5.88d_b$	68.61	0.033
No4-BL12.28d-TL7.5s-TG16-G0.5	$1.00d_b$	168.03	0.062
No4-BL12.20d-TL7.5s-TG14-G0.5	$1.00d_b$	222.97	0.078
No4-BL14.81d-TL7.5s-TG14-G0.5	$0.50d_b$	196.24	0.052
No4-BL14.81d-TL7.5s-TG13-G0.5	$0.50d_b$	191.63	0.056
No8-BL14.56d-TL10.0s-TG13-G0.5	$0.50d_b$	150.04	0.113
No8-BL17.00d-TL10.0s-TG11-G1.0	$0.50d_b$	112.20	0.064

Figure 3-22 shows the stress-strain relationship of three BRRs with different gaps. It can be seen that the total axial gap is a critical parameter to control the behavior of BRR, and should not exceed 0.5 times the bar diameter.

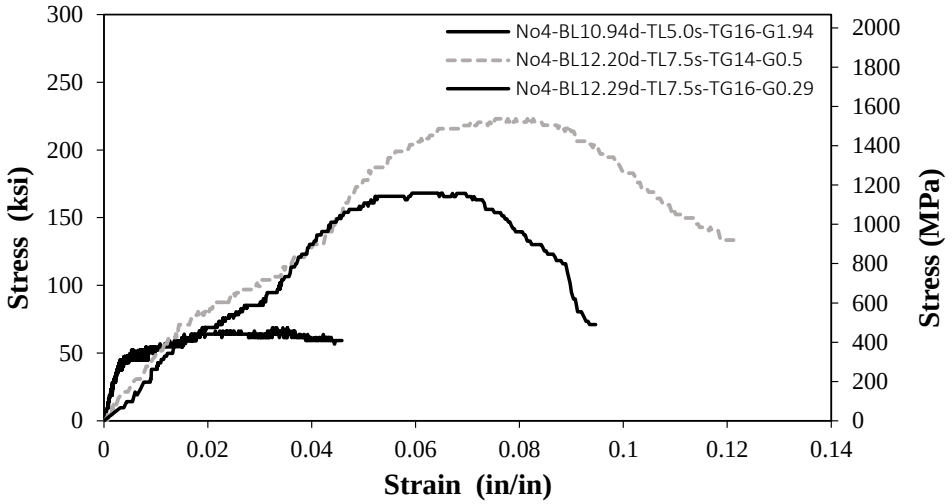

Figure 3-22. Stress-strain relationship of buckling restrained reinforcement (BRR) devices with different unsupported length

Furthermore, it was observed that the overall length of BRR also plays a significant role in a way that shorter BRR with the same tube properties exhibit higher compressive stress and strain capacities as shown in Fig. 3-23. Figure 3-24 shows the stress-strain relationship of two BRRs with the same properties but two different thickness for tubes. It can be seen that the tube thickness has insignificant effect on the BRR performance if tubes are designed properly.

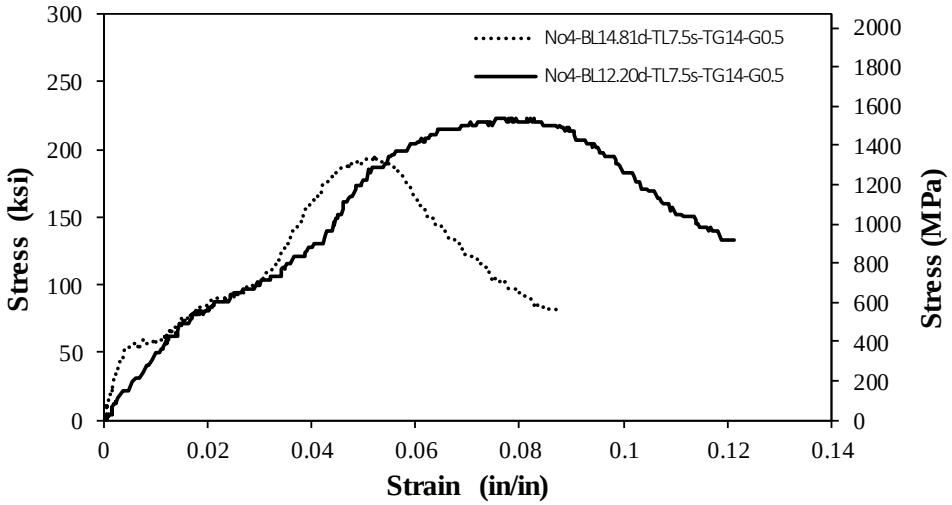

Figure 3-23. Stress-strain relationship of buckling restrained reinforcement (BRR) with different overall length of deformed bars

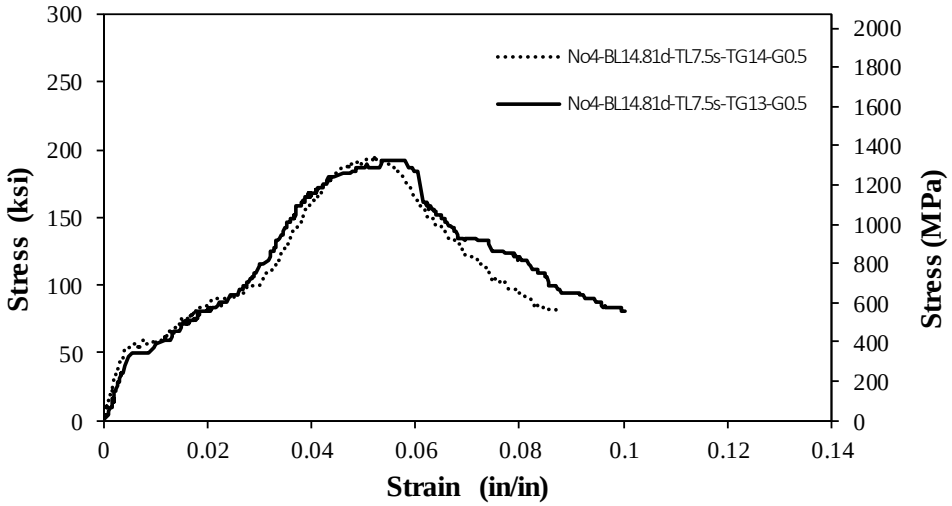

Figure 3-24. Stress-strain relationship of buckling restrained reinforcement (BRR) with different thickness of tube

Only one No. 4 BRR was tested under cyclic loading to failure as shown in Fig. 3-25. The test results confirmed that BRR can exhibit larger compressive stress and strain capacities under cyclic loads without low-cycle fatigue.

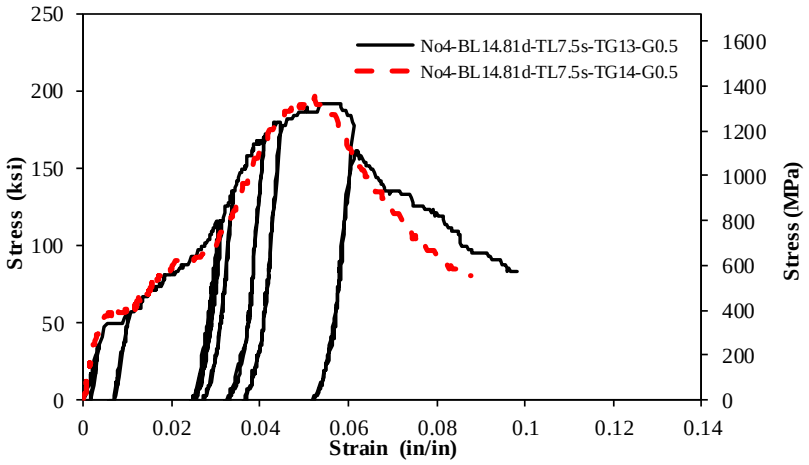

(a) Stress-strain response of BRR device

(b) BRR device at failure

Figure 3-25. Behavior of buckling restrained reinforcement (BRR) device due to cyclic loading

3.6. Summary and Conclusions

All previous studies focused on the performance of dog-bone energy dissipaters to be used in hybrid rocking columns. In an attempt to minimize

machining and cost, the use of conventional deformed reinforcing bars without section reduction, which was referred to as buckling restrained reinforcement (BRR), was proposed as external energy dissipaters. Total eight buckling restrained reinforcement (BRR) specimens tested under monotonic compressive loads to observe their structural behavior. One BRR specimen was also tested under cyclic loading. Based on the experimental investigation, the following conclusions can be drawn:

- The axial gap between the tube and the support plays a significant role to control the compressive behavior of BRR. It was observed that the compressive strength of BRR exceeds the ultimate strength of reinforcing bars if the gap does not exceed $0.5d_b$.
- BRR can sustain a very large compressive stresses before buckling when the axial gap is less than $0.5d_b$. For example, a BRR with No.4 reinforcing steel bar showed 200 *ksi* (1379 *MPa*) compressive strength when the total axial gap between the tube and the support was $0.5d_b$.
- The compressive strain of BRR at the peak stress exceeded 5%, which will be sufficient in most practical cases since the strain of compressive reinforcement in a concrete section is usually controlled by the core concrete strains.
- Short BRRs show larger compressive stresses and strain capacities with the same tube properties than longer BRRs.
- BRRs with thicker tubes were achieved higher stresses and strain capacities compared to those with thinner tubes.

3.7 References

1. ASTM Standard C39-12 (2012). "Standard test method for compressive strength of cylinder concrete specimens," ASTM International, West Conshohocken, PA.
2. Guerrini, G., Restrepo, J. I., Massari, M., and Vervelidis, A. (2014). "Seismic behaviorof posttensioned self-centering precast concrete dual-shell steel columns," Journal of structural engineering, 141(4), 04014115.
3. Guerrini, G., Restrepo, J., Vervelidis, A., Massari,M. (2015). “Self-Centering Precast Concrete Dual-Steel-Shell Columns for Accelerated Bridge Construction: Seismic Performance, Analysis, and Design,” PEER Report No. 2015/13, Pacific Earthquake Engineering Research Center, Headquarters at the University of California, Berkeley
4. Guo, T., Cao, Z., Xu, Z., and Lu, S. (2015). "Cyclic load tests on self-centering concrete pier with external dissipators and enhanced durability," Journal of structural engineering, 142(1), 04015088.
5. Marriott, D., Pampanin, S., and Palermo, A. (2009). "Quasi-static and pseudo-dynamic testing of unbonded post-tensioned rocking bridge piers with external replaceable dissipaters," Earthquake Engineering & Structural Dynamics, 38(3), 331-354.
6. Marriott, D., Pampanin, S., and Palermo, A. (2011). "Biaxial testing of unbonded post-tensioned rocking bridge piers with external replacable dissipaters. Earthquake Engineering & Structural Dynamics," 40(15), 1723-1741.
7. Mashal, M., Palermo, A., and Chegini, Z. (2014). "Quasi-static cyclic tests of half-scale fully precast bridge bents incorporating emulative and posttensioned

low damage solutions," Paper presented at the 2nd European Conf. of Earthquake Engineering and Seismology, Turkish Earthquake Foundation, Istanbul, Turkey.

8. Mesa, A., and Dario, A. (2010). "Developments of Advanced Solutions for Seismic Resisting Precast Concrete Frames," PhD thesis, University of Canterbury, Christchurch, New Zealand.
9. Palermo, A., and Pampanin, S. (2008). "Enhanced seismic performance of hybrid bridge systems: Comparison with traditional monolithic solutions," Journal of Earthquake Engineering, 12(8), 1267-1295.
10. Sarti, F., Palermo, A., and Pampanin, S. (2016). "Fuse-Type External Replaceable Dissipaters: Experimental Program and Numerical Modeling," Journal of structural engineering, 04016134.
11. White, S., and Palermo, A. (2016). "Quasi-Static Testing of Posttensioned Nonemulative Column-Footing Connections for Bridge Piers," Journal of Bridge Engineering, 21(6), 04016025.

CHAPTER 4. BEHAVIOR OF MODERN BEAM-COLUMN CONNECTIONS

4.1. Introduction

Reinforced concrete (RC) buildings need to be designed for large lateral displacement capacities in high seismic regions. Seismic detailing and special provisions by current building codes ensure collapse prevention. For special moment-resisting frames, current codes are as based on a design philosophy of "strong columns, weak beams" in which all plasticity is concentrated on beams and columns and the beam-column joints should experience minimal damage. The performance of an exterior beam-column (BC) joint designed based on the current code (ACI 318, 2014), was experimentally investigated in this chapter to evaluate the design philosophy.

First, a nine story special RC building was designed for a high seismic region. A half-scale beam-column specimen was design and constructed based on one of the exterior joints of the first story of the prototype model. A new test setup was designed to include the actual boundary conditions. Then, the specimen was tested under a cyclic loading protocol to simulate seismic effects. Finally, the performance of the specimen was evaluated.

4.2. Research Objectives

Several studies have investigated the performance of BC joints (Pauly and Park, 1970; Ehsani and Wight, 1995; Scott, 1996; Li et al. 2009; Tsonos, 2009). However, none of them successfully modeled the boundary conditions in their experiments. The main goal of this study was to investigate the seismic performance of a modern BC joint including actual boundary conditions.

4.3. Past Studies on Beam-Column Joint

The behavior of external beam-column joint under cyclic loading has been extensively investigated experimentally in the past few decades, which were mainly focused on joint shear detailing. The summary of selected previous studies is reported herein.

4.3.1. Study by Paulay and Park (1978)

Paulay and Park (1978) tested an interior-beam column joint of a ductile reinforced concrete frame under reversed cyclic loading. This study concluded that the shear resistance of the concrete in the joint is because of the contribution of the joint diagonal struts. Due to forming the plastic hinge in the beam, the joint remained elastic, and the shear was completely carried by the concrete as there was no degradation in the shear force in the elastic region. The study also concluded that the diameter of the beam longitudinal bars should not be excessive to avoid the bond failure in the joint.

4.3.2. Study by Durrani and Wight (1985)

Durrani and Wight (1985) tested an interior beam-column joint under a cyclic loading. It was reported that the joint shear stresses had significant effect on the

strength and stiffness of bean-column connection at high ductility levels (greater than 2). At lower ductilities, the effect of the transverse reinforcement of the joint was more significant. It was observed that joint shear deformations, bars slippage, and the pinching of hysteretic loops were mostly affected by the joint shear stresses. Moderate amount of reinforcement with a low joint shear stress tends to be a better design option than a heavily reinforced joint with high shear stresses. This study was also concluded that the minimum column to beam flexural strength ratio of 1.5 is suitable for the seismic design.

4.3.3. Study by Ehsani and Wight (1985)

Ehsani and Wight (1985) tested six exterior beam-column connections under cyclic loading. The test variable were varied the column – beam flexural capacity, the joint shear stresses, and the transverse reinforcement in the joint. The study concluded that larger column to beam flexural strength ratios significantly improve the behavior of beam-column connections. The column to beam flexural strength ratio of 1.4 and higher prevents the formation of plastic hinges in the joint region. A significant improvement in the behavior was observed for joints with a shear stress of $12\sqrt{f_c'}$ (psi) or lower. The study also concluded that additional transverse reinforcement in the joint enhances the overall behavior of the connection.

4.3.4. Study by Ehsani et al. (1987)

Ehsani et al. (1987) tested four exterior beam-column connections under cyclic loading. Both normal strength concrete (NSC) and high strength concrete (HSC) were incorporated. This study concluded that RC joints with HSC exhibit sufficient ductility and show similar ductile hysteretic response compared to RC

frames with NSC in the joint region. Specimens with high column to beam flexural strength ratios and low joint shear stresses showed large displacement capacities.

4.3.5. Study by Fujii and Morita (1991)

Fujii and Morita (1991) tested eight, 1/3-scale exterior and interior beam-column connections. The strength of reinforcing bars in beams, column axial loads, and the joint transverse reinforcement were varied in these tests. It was concluded that 200% increase in the column axial load [30 (133.4) to 90 *kips* (400.3 *kN*)] by did not improve of the shear strength of the interior joints, but it was improved by 10% in exterior joints. Furthermore, it was also observed that increasing the joint shear reinforcement ratio from 0.41 to 1.15% by volume had insignificant effect on the overall behavior

4.3.6. Study by Joh et al. (1991)

Joh et al. (1991) tested two series of beam-column joints in RC frames. This study concluded that joint heavily reinforced with transverse bars showed minimal bond-slip effects. This study suggested that bond deterioration of beam reinforcement in the joint may be prevented significantly by relocation the plastic hinges away from the column face.

4.3.7. Study by Scott (1996)

Scott (1996) tested 17 exterior beam-column connections subjected to both monotonic and cyclic loading. Test variables were the beam depth, the beam tension steel percentage, reinforcement details of beam tension steel, and the column load. The study used three different seismic detailing of beam reinforcement: beam

reinforcement bent up or down into the column and beam reinforcement bent into U-bar. The study compared the theoretical moment capacities with those from the test. It was found that the performance of joints with reinforcement bent-down and U-bar detailing was better that those with the bars-bent-up detailing. In case of seismic loading, the bond deteriorated in the connection due to the large strain increments from each loading cycle as well as concrete spalling away from the reinforcement.

4.3.8. Study by Hwang et al. (2005)

Hwang et al. (2005) tested an exterior beam-column connection under earthquake type loading to investigate the effect of joint hoops on the shear strength. It was concluded that the joint hoops act as tension ties and constrain the crack width. The hoop reinforcement in joint up to 12 *in.* (304.8 *mm*) of spacing has no significant influence to the performance of joints. This study also concluded that the intermediate longitudinal bar of beams passing through the joint cannot be considered as alternative to horizontal joint hoops due to their participation in beam flexure behavior.

4.3.9. Study by Tsonos (2007)

Tsonos (2007) tested four half-scale exterior beam-column connections subjected to a large number of inelastic cycles. This study followed weak beam-strong column design philosophy based on Eurocode, Greek code, and ACI318-05 code. This study reported excessive damage in the joint region in two beam-column connections as they performed poorly under reversed cyclic lateral deformations. These two connections exhibited shear failure during the early stages of cyclic

loading. This happened because the calculated joint shear stress was higher than the joint ultimate strength.

4.3.10. Study by Walsh et al. (2016)

Walsh et al. (2016) performed an experimental study on BC joints extracted from a building damaged in 2016 Christchurch earthquake. Three precast RC moment-resisting frame specimens were extracted and tested under cyclic loading. It was found that the precast RC beams with shear ductile detailing had lower displacement capacity compared to those of conventionally detailed beams.

4.4. Experimental Setup for Past Studies

The review of the previous experimental studies revealed that none of these studies modeled the actual boundary condition of a beam-column joint the test in which column and beam can both rotate and sway (Fig. 4-1). Many of the studies installed an actuator at the end of beam to apply the cyclic load to the test specimen. A handful of studies (Tsonos, 2009; Durrani, 1995; Carlos et al., 2001) applied actual lateral load to the tip of the column but failed to allow the beam to sway with the column. Li et al., (2009) used ideal test setup condition for lightly reinforced beam-column joints under cyclic loading but they did not apply axial load at column head (Fig. 4-5). However, this study did not allow the beam for horizontal movement. Figure 4-6 shows the ideal condition for exterior beam-column connection.

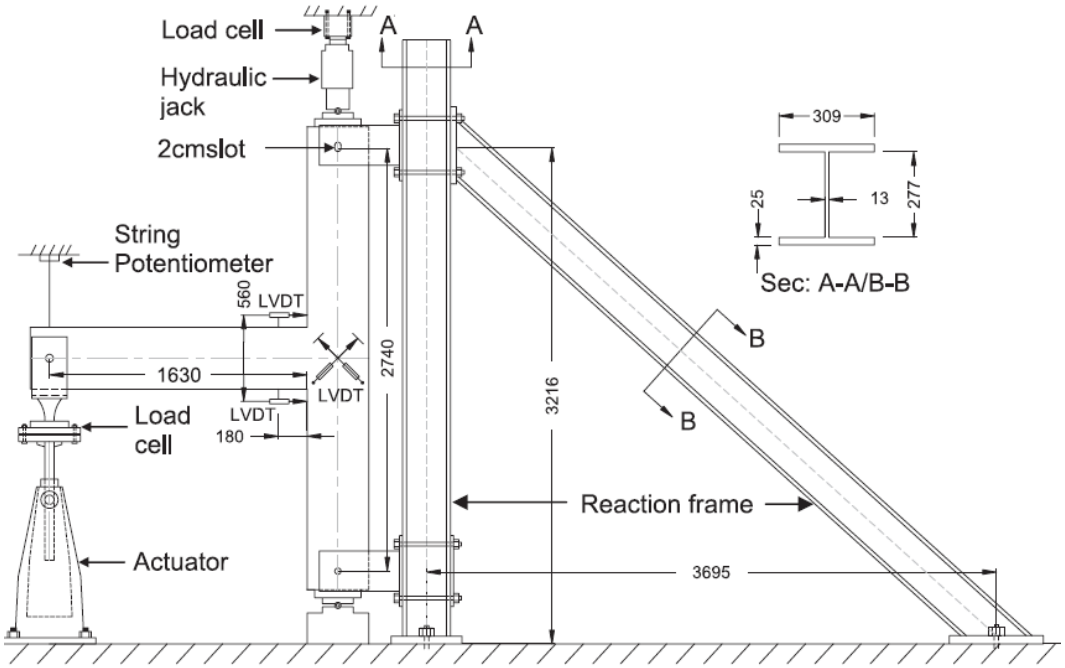

Figure 4-1. Test setup for exterior beam-column connection (Youssef et al., 2008)

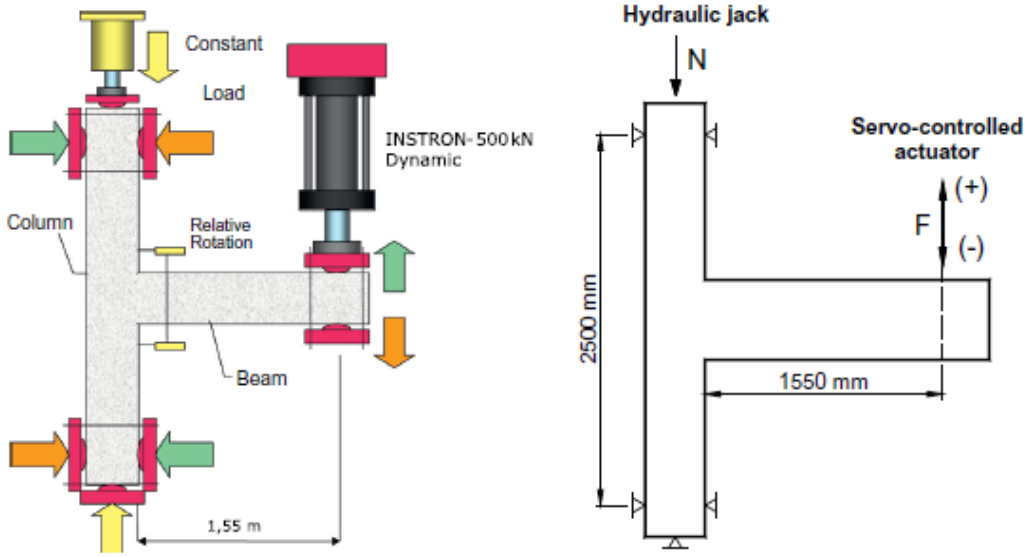

Figure 4-2. Applied load and static equilibrium for exterior beam-column connection (Alva et al. 2013)

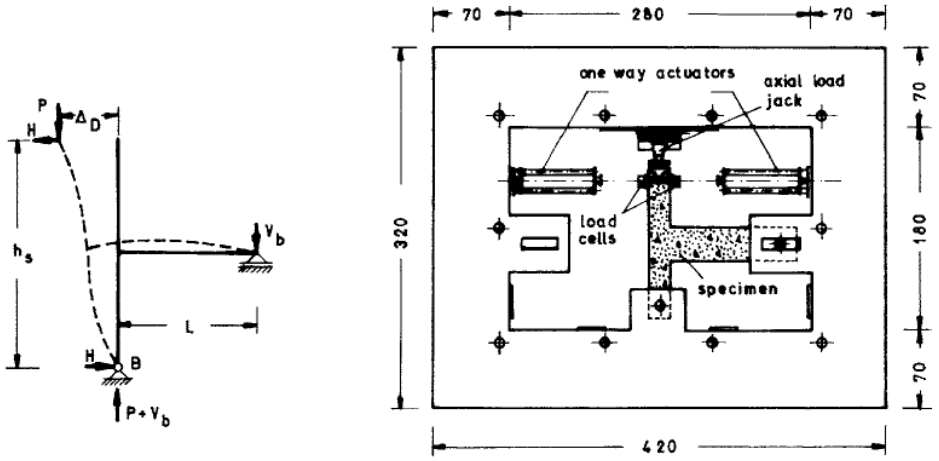

Figure 4-3. Test setup for exterior beam-column connection (Tsonos, 1999)

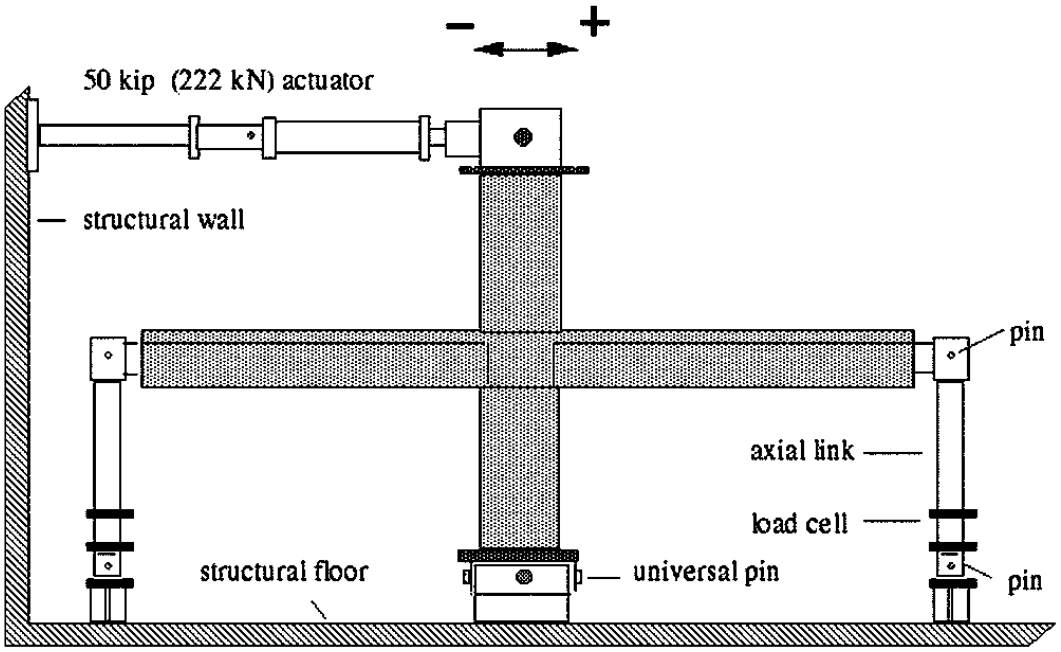

Figure 4-4. Experimental setup for interior beam-column connection (Quintero-Febres, 2001)

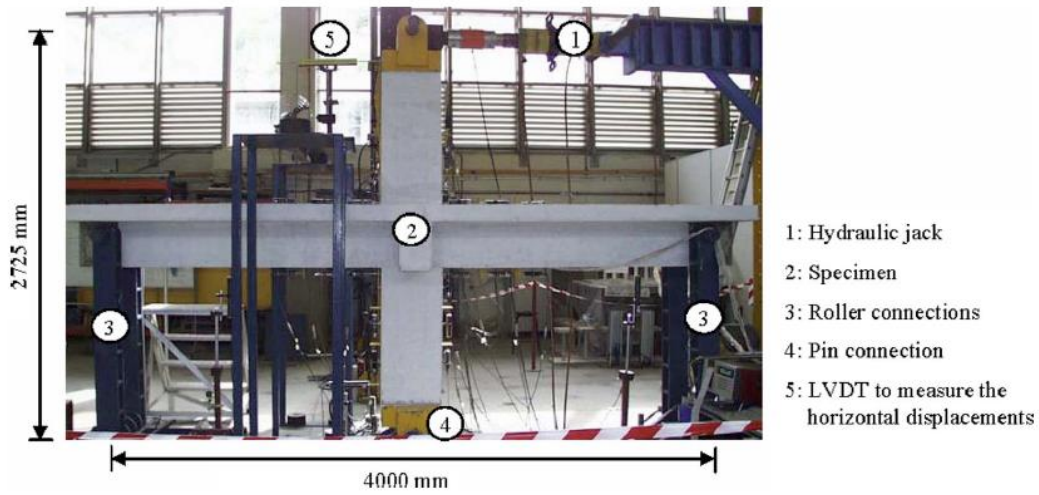

Figure 4-5. Test setup for interior beam-column connection (Li et at., 2009)

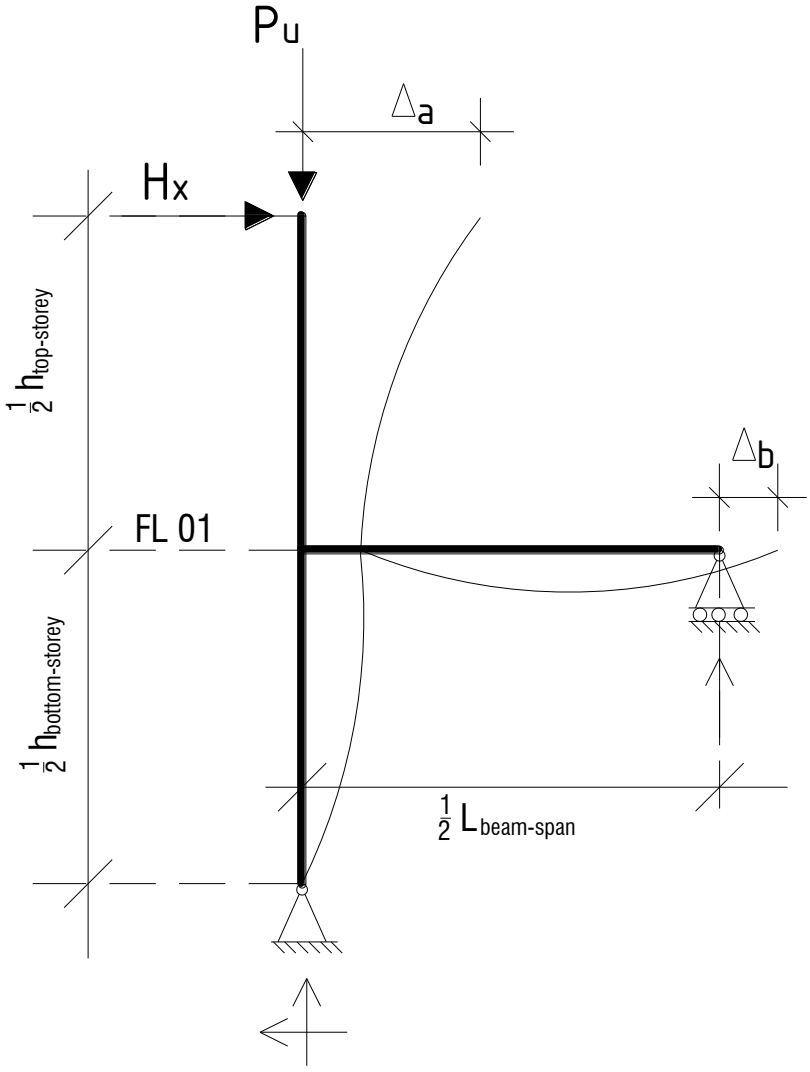

Figure 4-6. Actual boundary condition for exterior beam-column connection

4.5. Design of Prototype RC Building

A nine-story special moment-resisting RC office building was design according to current specifications to serve as prototype model. One of the building exterior beam-column joints was selected for experimental study. This section includes a review of special moment-resisting frames, design of nine-story office building as prototype, and design of the test specimen.

4.5.1. Special Moment Resisting Frames

The current earthquake-resistant design philosophy allows damage during earthquake in some predetermined structural components to provide higher displacement capacity. RC frames can be design as ordinary, intermediate, and special for different seismic demands. Special moment-resisting frames (SMRF) are used in high seismic regions since they exhibit relatively lateral displacement capacities without significant loss of stiffness and strength. SMRF are designed based on the "strong column, weak beam" philosophy since frames in which beams fail first exhibit larger displacement capacities than those in which column fails before beams as shown in Fig. 4-7. The design requirements for SMRF are presented in ACI318-14 (2014).

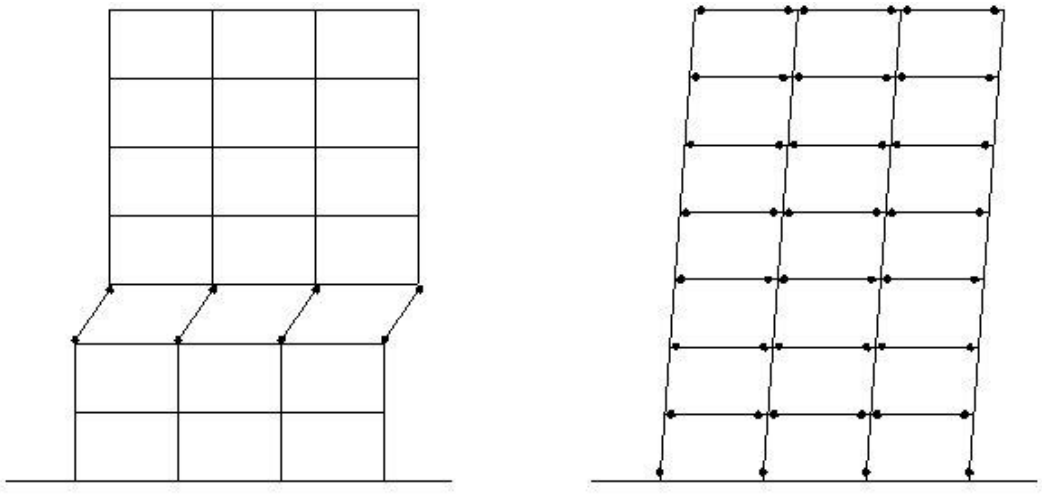

(a) Columns failure before beams (b) Beams failure before columns

Figure 4-7. Collapse mechanism for moment-resisting frames

4.5.2. Design of Nine-Story Special Moment-Resisting RC Building

A five-bay by five-bay nine-story office building (Fig. 4-8, Fig. 4-9, and Table 4-1) was considered in the present study. The building was assumed to constructed in Los Angeles, CA (Latitude 34.052235 N and Longitude 118.243683), which is considered a high seismic zone. "Special moment-resisting" RC frames were selected as the building lateral load resisting system. The floor plan was assumed to be the same for all levels.

ASCE 7-10 (2010) and ACI318-14 (2014) were selected as the main design codes. SAP2000 was used as the design software. Tables 4-2 to 4-5 present a summary of design requirements and Table 4-6 presents the final size of structural elements (beam and column). The specific concrete strength for all elements was 5000 *psi* (34.47 *MPa*).

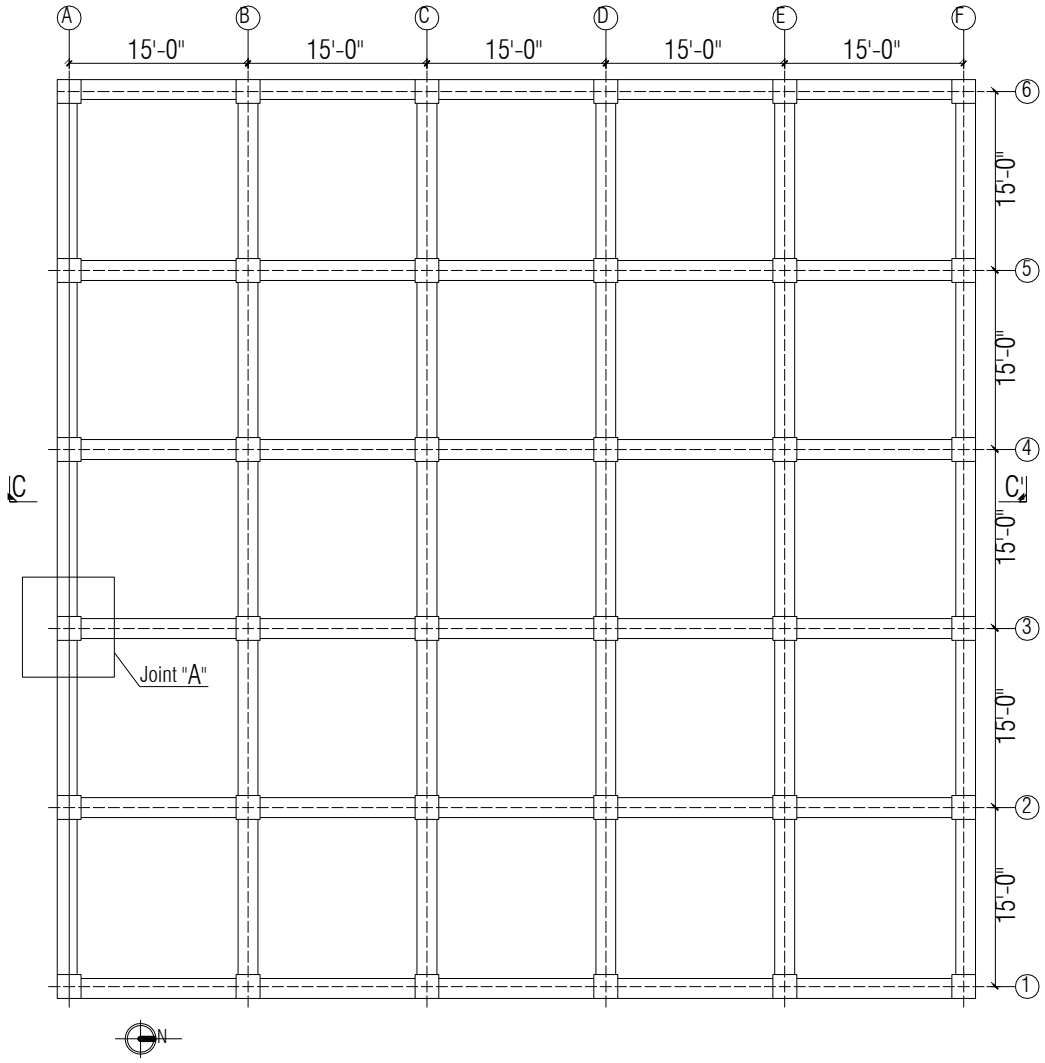

Figure 4-8. Plan view of nine-story RC building

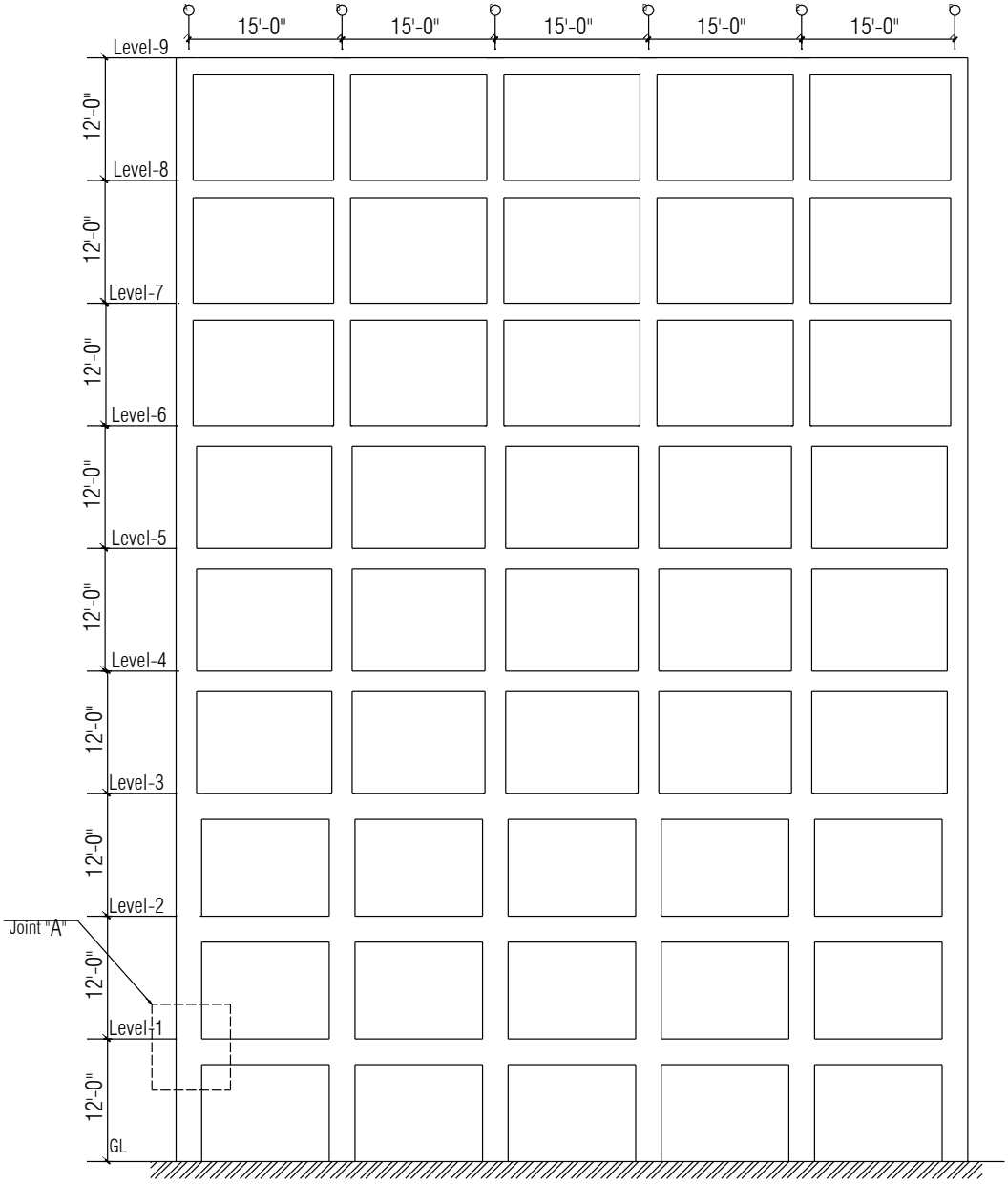

Figure 4-9. Elevation of nine-story building

Table 4-1. Configuration of proposed nine-story RC building

Description	Size/Dimension	Unit
No. of Story	9	
No. of Bay along X-axis	5	
No. of Bay along Y-axis	5	
Span Length c/c (Both ways)	15	*ft*
Floor Height	12	*ft*
Slab thickness	5	*In.*

Table 4-2. Dead and Live loads for proposed nine-story RC building

Load Type	Load	Unit
A. Floor Load		
Floor Finish (FF)	30	*psf*
Partition Wall (PW)	15	*psf*
Superimposed Dead Load (SD)	15	*psf*
Live Load (LL)	50	*psf*
B. Roof Load		
Floor Finish (FF)	50	*psf*
Live Load (LL)	20	*psf*
C. Exterior Wall Load (Stud walls with brick veneer)		
Exterior Line Load (LD)	0.48	*k/ft*
Exterior Line Load (LD) for roof	0.20	*k/ft*

Table 4-3. Seismic analysis of Nine-Story RC building

Type/Category	Symbol	Type/Value
Soil site class		D
Seismic risk category		ll
Seismic design category	SDC	D
Response modification coefficient	R	8
The importance factor	I_e	1
Peak ground acceleration	PGA	0.92g
Spectral response acceleration parameter		
	S_{DS}	1.622g
	S_{D1}	0.853g
	S_S	2.433g
	S_1	0.853g
Deflection amplification factor	C_d	5.5
Over strength factor	Ω_o	3
Redundancy factor	ρ	1

Table 4-4. Displacement requirements

Story Level	Displacement (*in.*)			
	Analysis Result	Story Displacement	Amplified Displacement	Allowable Displacement
9	2.98	0.20	1.10	2.88
8	2.78	0.36	1.96	2.88
7	2.42	0.45	2.48	2.88
6	1.97	0.40	2.22	2.88
5	1.57	0.44	2.43	2.88
4	1.12	0.41	2.27	2.88
3	0.71	0.29	1.59	2.88
2	0.42	0.27	1.47	2.88
1	0.15	0.15	0.85	2.88

Table 4-5. Load combinations

Load No.	Load combination
1	1.4 DL
2	1.2 DL + 1.6 LL
3	1.2 DL + 1.0 LL + 1.0 EQX
4	1.2 DL + 1.0 LL - 1.0 EQX
5	1.2 DL + 1.0 LL + 1.0 EQY
6	1.2 DL + 1.0 LL - 1.0 EQY
7	0.9 DL + 1.0 EQX
8	0.9 DL - 1.0 EQX
9	0.9 DL + 1.0 EQY
10	0.9 DL - 1.0 EQY

DL = Dead load; LL = Live load; EQX = Earthquake load in X direction, EQY = Earthquake load in Y direction

Table 4-6. Final dimension of structural elements for story RC building

Element Type	Floor Level	Dimension (*in.* × *in.*)
Column	Ground floor to 3rd floor level	30 × 30
	3rd floor level to 6th floor level	24 × 24
	7th floor level to 9th floor level	20 × 20
Beam	Ground floor to 3rd floor level	20 × 30
	3rd floor level to 6th floor level	20 × 24
	7th floor level to 9th floor level	20 × 20

4.5.3. Design of Prototype Beam-Column Connection

The building was designed for all possible load combinations meeting the requirement of the codes. Subsequently, Joint A (Fig. 4-8 and Fig. 4-9) was selected for the experimental study. This section includes the design parameters and the detailing of Joint A.

ASTM A706 Grade 60 deformed reinforcement was used for all members. The column design axial load, *P*, was 272 *kips* (1210 *kN*). Seismic detailing was based on ACI 318 (2014) for special moment-resisting frames. The detailing of the prototype beam-column specimen is shown in Fig. 4-10.

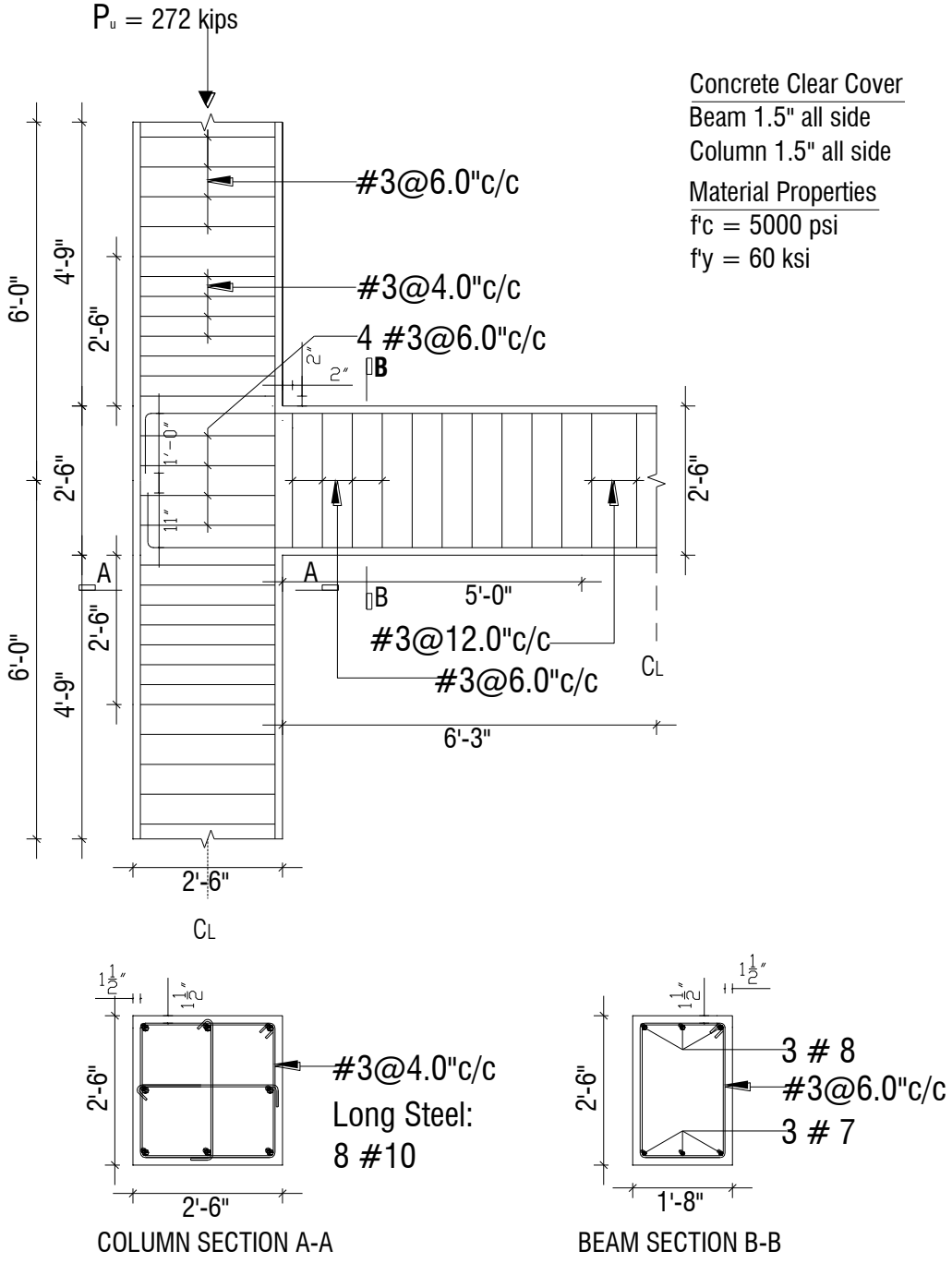

Figure 4-10. Detailing of prototype exterior beam-column joint

4.5.4. Design of Half-Scale Beam-Column Specimen

A half- model of the prototype beam-column specimen was selected for testing in the present study. The scaling of test model was generally based on the

procedure proposed by Krawlnkler and Piotr (1982). However, some of the design parameters such as concrete cover and confinement cannot be directly scaled down. To successfully simulate the structural behavior of the selected exterior beam-column specimen and to relate the findings to the actual nine-story building, confinement of the test model was selected to be the same as that for the prototype specimen.

Mander's model (Mander et al., 1998) was used to match the confinement of the prototype and the test model sections (Fig. 4-11and 4-12). Note that due to the spacing limitation for the beam stirrups, the confinement properties (specially the residual stress and the strain capacity) of the half-scale beam was slightly higher than those for the prototype beam. Flexural capacity of columns in special moment-resisting frames should be at least 20% stronger than that of the beams. Moment-curvature analysis of the test model section (Fig. 4-13) shows that this requirement is met. The detailing of the test model is shown in Fig. 4-14.

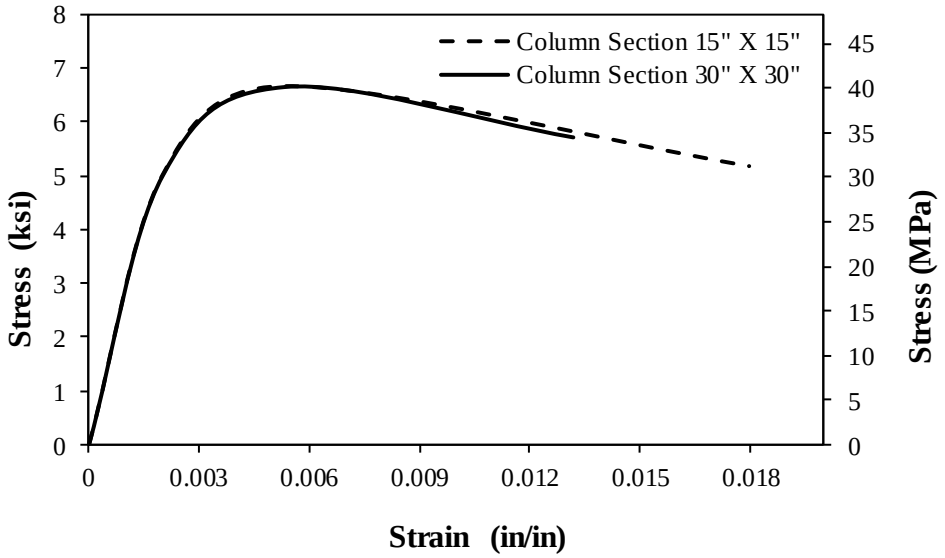

Figure 4-11. Confined concrete stress-strain relationship for prototype and half-scale columns

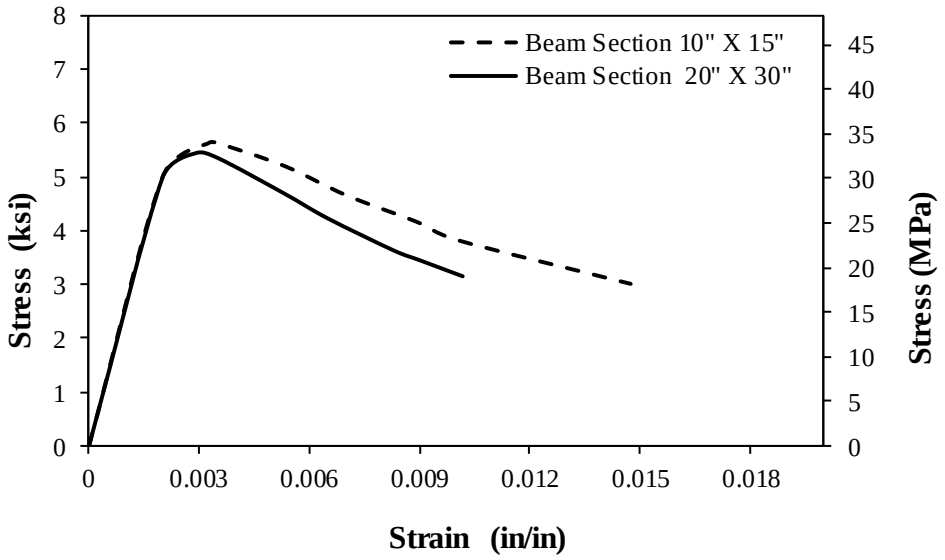

Figure 4-12. Confined concrete stress-strain relationship for prototype and half-scale beams

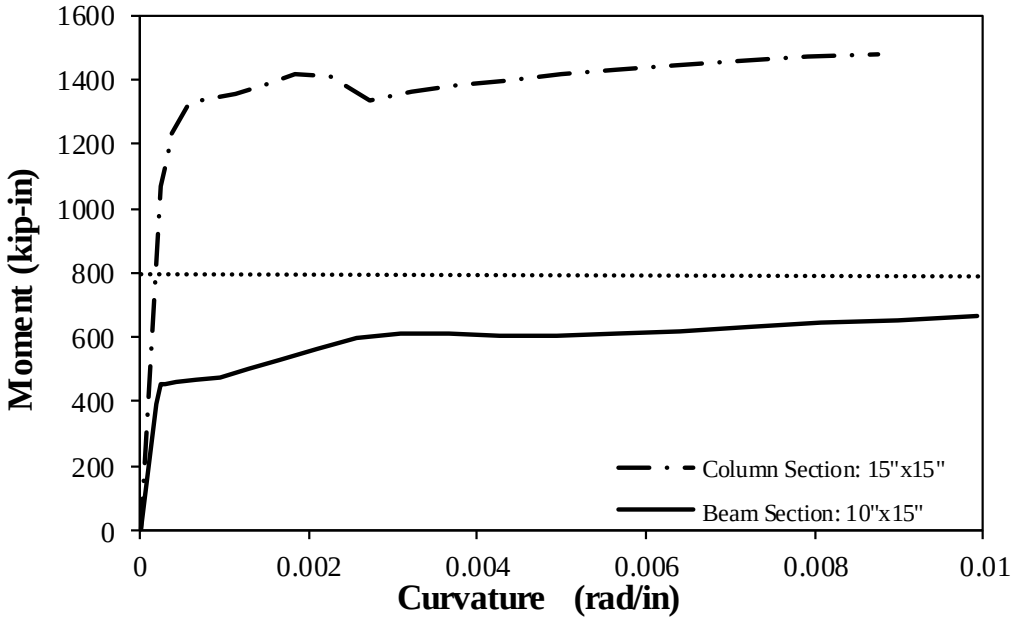

Figure 4-13. Moment–curvature relationships for beam and column of test model

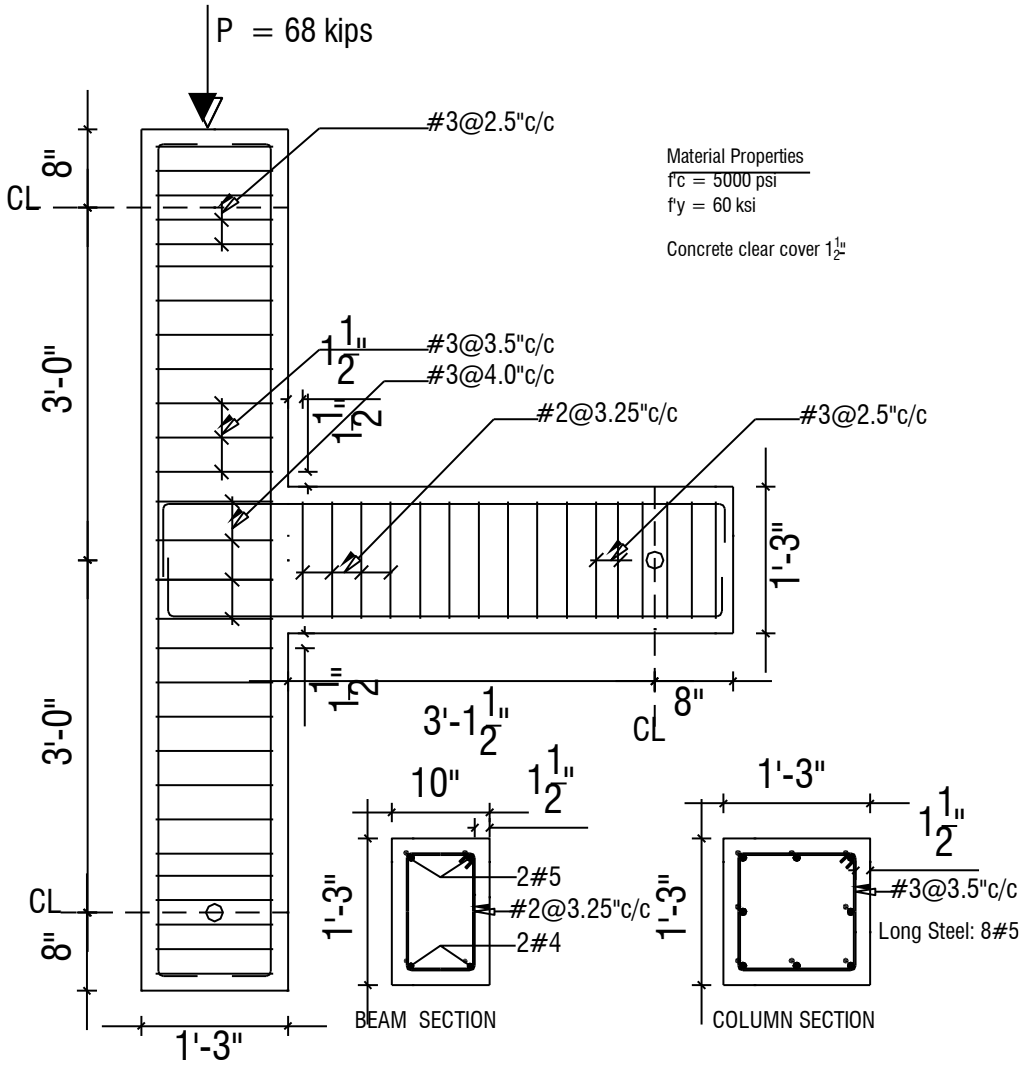

Figure 4-14. Detailing of test beam-column model

4.6. Experimental Program

The half-scale beam-column specimen was constructed and tested the Lohr Structural Laboratory at South Dakota State University (SDSU) to investigate the performance of the special moment-resisting building designed based on the current codes. The detail of test program is described in this section.

4.6.1. Material Properties

Ready mix concrete with a target compressive strength of 5000 *psi* (34.47 *MPa*) was used to cast the members. Eight ASTM A706 Grade 60 No. 5 bars were

used as the column longitudinal reinforcement and the column was transversely reinforced with No. 3 stirrups at 3.5 *in.* (88.9 *mm*) on center. For the beam, 2-No. 5 and 2-No. 4 bars (both ASTM A706 Grade 60 were used the top and bottom of the section, respectively. To match the confinement of the scaled model beam with that of the prototype, No. 2 deformed steel wire stirrups (with a diameter of 0.25 *in.* (6.35 *mm*) conforming to ASTM A496) spaced 3.25 *in.* (82.5 *mm*) were used as transverse reinforcement. Typical properties of the deformed bars and wires used in the test model are presented in Table 4-6 and Table 4-7.

Table 4-7. Typical properties of reinforcing steel bars

Property	Value
Grade	60
ASTM Type	A706
Yield Stress, f_y (*ksi*)	60
Modulus of Elasticity, E_s (*ksi*)	29,000
Expected Yield Stress, f_{ye} (*ksi*)	68
Ultimate Tensile Strength, f_u (*ksi*)	95
Expected Yield Strain, ε_{ye} (*in.*)	0.0023
Ultimate Strain, ε_u (*in./in.*)	0.09

Table 4-8. Typical properties of deformed wire

Property	Value
ASTM Type	A496
Yield Stress, f_y (*ksi*)	75
Modulus of Elasticity, E_s (*ksi*)	29,000
Ultimate Tensile Strength, f_u (*ksi*)	85

4.6.2. Pretest Load and Displacement Relationship

A pretest pushover analysis was performed to estimate the yield and ultimate displacements of the beam-column joint (Fig. 4-15). OpenSees (2013) was used for the analytical study. It was found that the longitudinal reinforcement of the beam will fail first indicating that a large displacement will be achieved. The yield and the ultimate displacements based on the pretest analysis were 0.24 in. (6.1 *mm*) and 2.75 *in.* (69.85 *mm*), respectively.

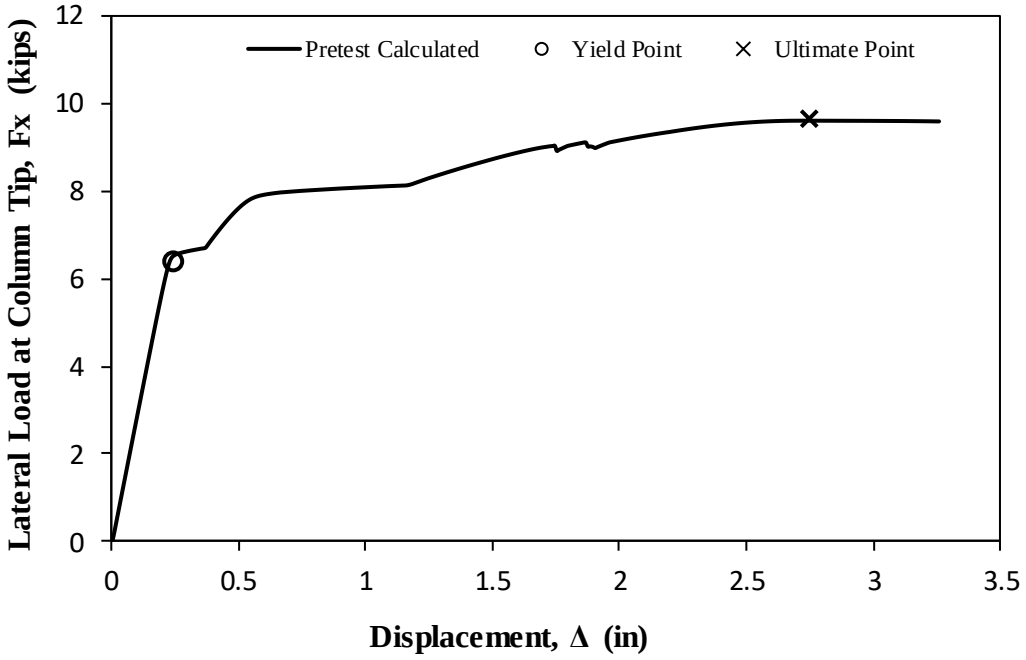

Figure 4-15. Pretest lateral force-displacement relationship for beam-column test model

4.6.3. Construction of Test Specimen

Figure 4-16 shows the steel cage and the formwork. Bar spacers were used to provide clear cover of 1.5 *in.* (38 *mm*). The slump of the ready mix concrete was 4.5 *in.* measured according to ASTM standard C143 (2012) (Fig. 4-17). Figures 4-18 to 4-20 shows the construction stages of the test specimen. Sixteen standard concrete cylinders (6 by 12 *in.*) were collected for strength testing according to ASTM Standard C617-12 (2012).

Figure 4-16. Steel cage and formwork

Figure 4-17. Slump of ready mix concrete

Figure 4-18. Concrete pouring for beam-column test specimen

Figure 4-19. Curing of beam-column test specimen

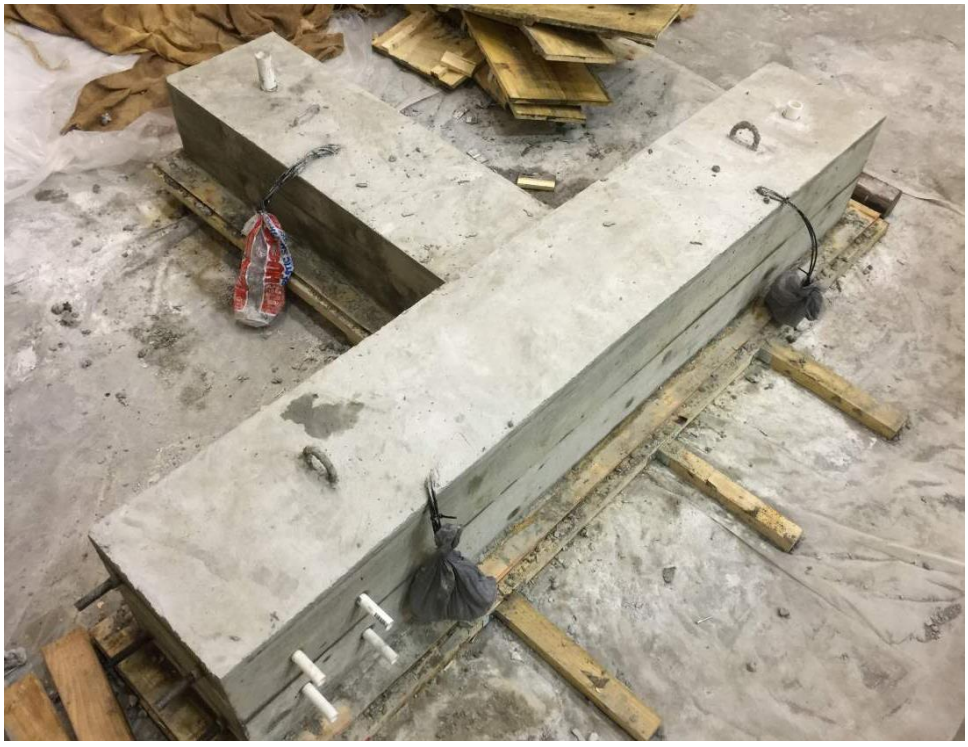

Figure 4-20. Beam-column test specimen

4.6.4. Test Setup

Figures 4-21 and 4-22 show the test setup designed for the beam-column specimen. As was discussed before, previous experimental studies failed to simulate the actual boundary condition of beam-column specimens in which both column and beam should be free to sway under lateral loads. In an attempt to accurately model the actual boundary conditions, a rocker and a roller were respectively designed for the column base and the free end of the beam (Fig. 4-23). The rocker was made using a heavy-duty steel shaft passing through a vertically slotted support and a steel pipe installed at the column base (Fig. 4-23b). The beam end support was the same as that of the column base but a long slotted hole was provided in the support (beam reaction chair) to allow the specimen to move in the direction of the lateral loading (Fig. 4-23c). The roller was restrained with a 1.5-*in.* (38.7-mm) threaded rod to prevent uplift.

Figure 4-222 also shows the axial load setup in which the column 68-kip axial load was applied by post-tensioning the rods using two 100-ton hollow-core jacks. All setup components were design based on the capacity of the specimen according to the allowable stress design (ASD) method of AISC (2011).

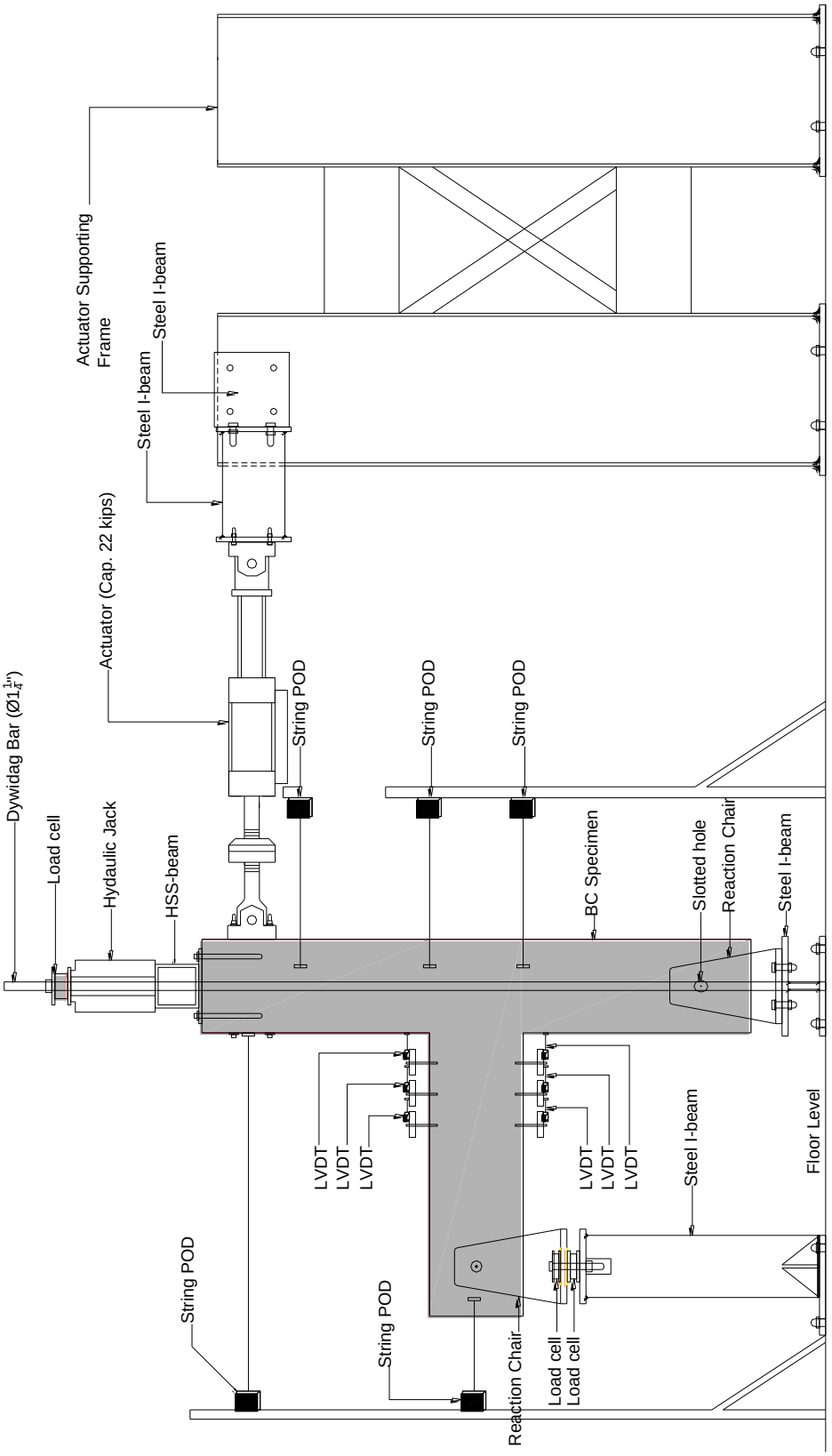

Figure 4-21. Test setup for beam-column specimen

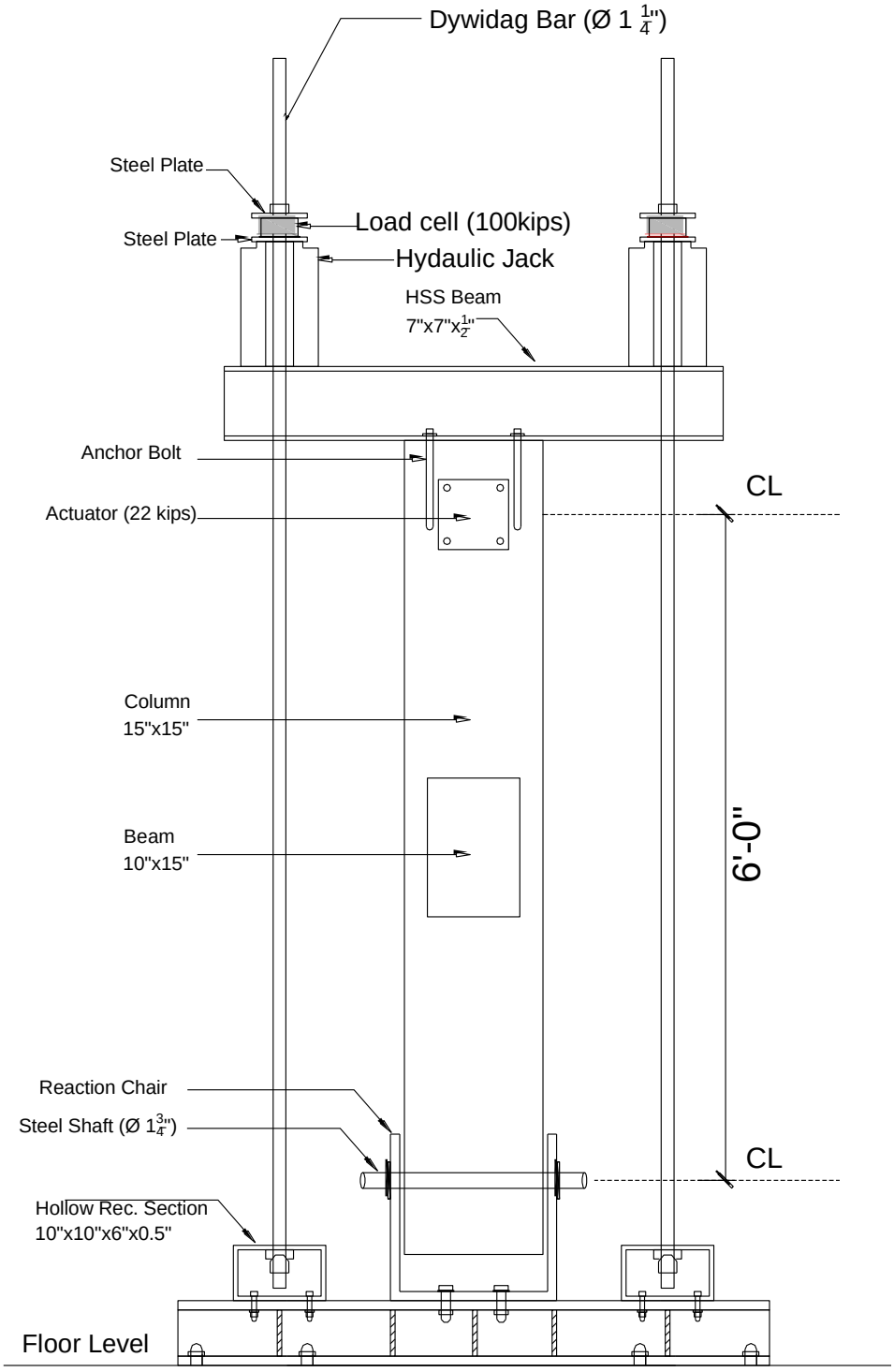

Figure 4-22. Axial load test setup for beam-column specimen

(a) Complete test setup

(b) Reaction chair under beam

(c) Reaction chair under column

Figure 4-23. Photograph of test setup for beam-column specimen

4.6.5. Instrumentations

The test specimen was instrumented with strain gauges, load cells, and displacement measurement devices. Sixteen strain gauges were installed at different locations (Fig. 4-24 and 4-25) of the beam-column specimen to measure the strains. Of which, six strain gauges were installed on the top and the bottom of the longitudinal

reinforcing steel bars of the beam, six strain gauges were installed on the column longitudinal bars of column at both inner and outer face of the joint, and the remaining on the transverse reinforcement.

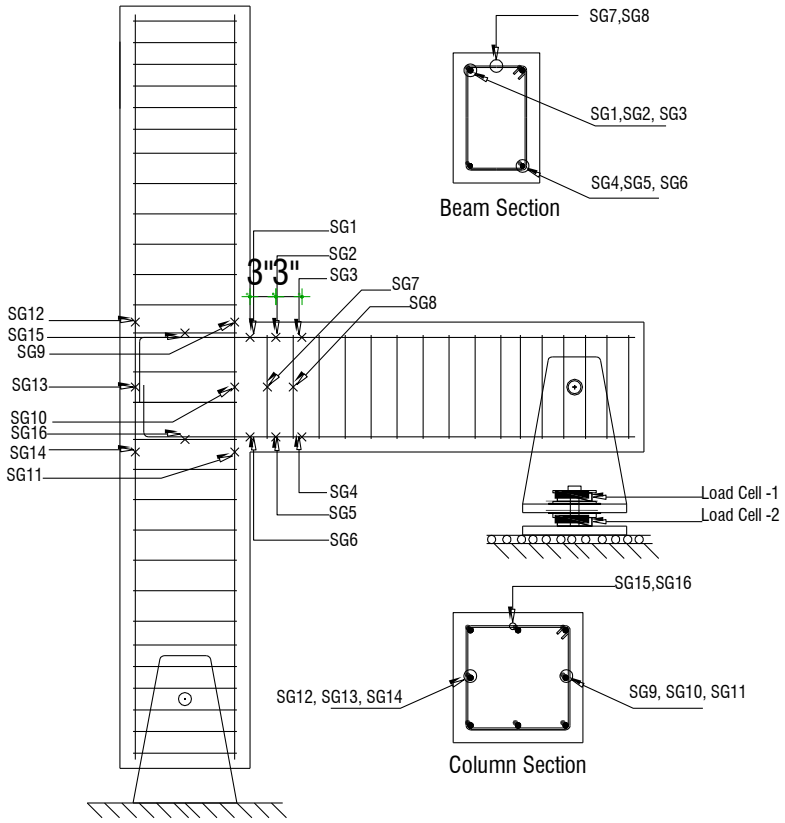

Figure 4-24. Location of strain gauges in beam-column specimen

Figure 4-25. Installation of strain gauges in beam-column specimen

Six linear variable displacement transducers (LVDT) were installed at the top and the bottom of the beam to measure the beam rotation and curvature (Fig. 4-26). Furthermore, four string POTs were installed in different locations of the specimen (Fig. 4-26) to measure the lateral displacements as well as the joint rotations.

An actuator with ±5 *in*. (±127 *mm*) stroke was used at the top of column to apply lateral displacements.

Two 100-*kip* (444.8- *kN*) load cells were used at the top of the hydraulic jacks to measure the axial load applied to the column. Two other load cells each with a 50-*kip* (222.4 *kN*) capacity were used at the beam end roller to measure either the compressive or tensile reactions.

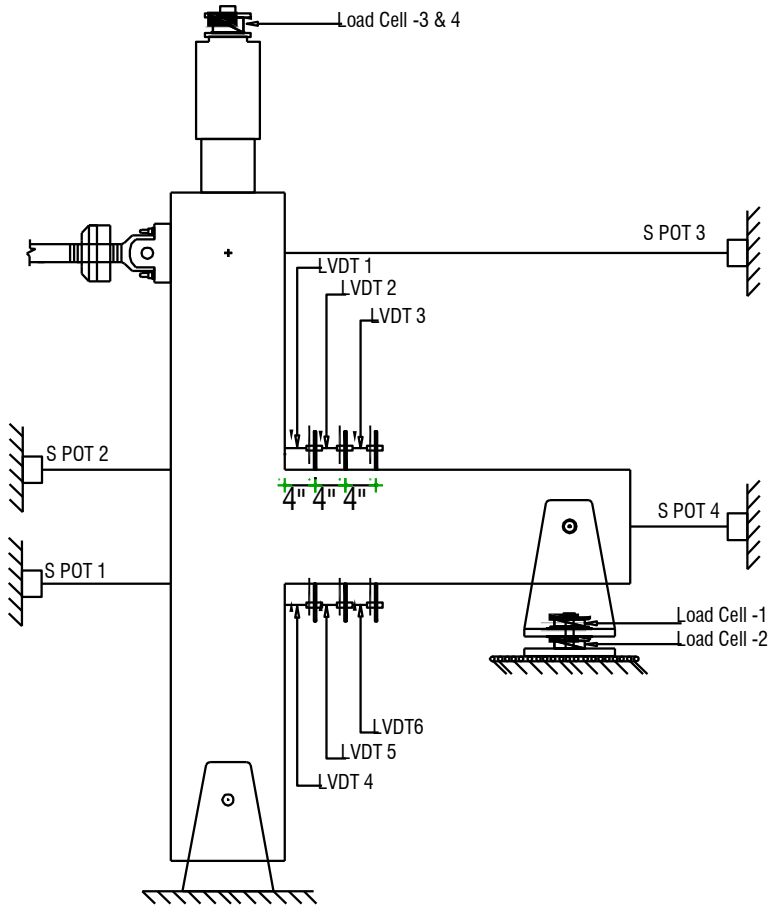

Figure 4-26. Installation of LVDT, String POT, and Load Cell in beam-column specimen

4.6.6. Loading Protocol

A displacement-based loading protocol (Fig. 4-27) conforming to the ACI simulated seismic loading protocol (ACI 374.2R-13, 2013) was selected for the testing of the beam-column specimen. Two full cycles were completed for each target displacement. Two loading rates were utilized in the experiment: a displacement of 0.03 *in./sec* (0.76 *mm/sec*) up to 2 times the expected yield displacement to capture the yield point, and a displacement rate of 0.15 *in./sec* (3.8 *mm/sec*) at higher displacements. Drift ratio is defined as the ratio of the column tip displacement at the actuator centerline to the column height from the pin to the actuator centerline (Fig. 4-21). The column height was 72 *in.* (1828.8 *mm*)

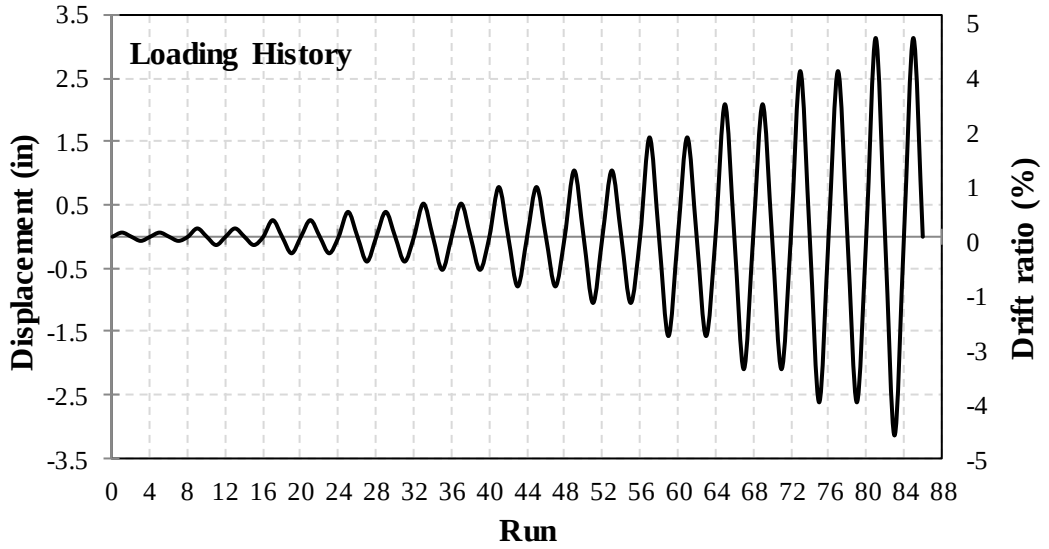

Figure 4-27. Complete displacement-based loading protocol for beam-column specimen

4.7. Experimental Results

4.7.1 Compressive Strength of Concrete

A summary of the compressive strength of concrete cylinders tested according to ASTM Standard C39-12 (2012) is presented in Table 4-9. Note that the reported strengths are for both the beam and the column.

Table 4-9. Compressive strength of concrete

Age (day)	Concrete Strength, f_c' (*psi*)
3	4075
14	4825
28	5110
Beam-Column Test Day	5415

Note: Three samples were tested for each day. The average data was reported.

4.7.2. Strength of Reinforcing Bar

Reinforcing steel bars and wires were tested according to ASTM Standard A370-12 (2012). A summary of the measured mechanical properties is reported in Table 4-10 and 4-11. Figure 4-28 to 4-30 shows the stress-strain behavior of reinforcing steel bars.

Table 4-10. Measured mechanical properties for ASTM A706 steel bars

Property	Bar Size		
	No. 3	No. 4	No. 5
Grade	60	60	60
Yield Stress, f_y	78.77 *ksi* (543.1 *MPa*)	77.25 *ksi* (532.6 *MPa*)	76.85 *ksi* (529.9 *MPa*)
Ultimate Tensile Strength, f_u	117.8 *ksi* (812.2 *MPa*)	118.25 *ksi* (815.3 *MPa*)	113.27 *ksi* (781.0 *MPa*)
Strain at Peak Stress, ε_u	0.0659 *in./in.*	0.0597 *in./in.*	0.0742 *in./in.*
Strain at fracture	0.119 *in./in.*	0.125 *in./in.*	0.139 *in./in.*

Table 4-11. Measured mechanical properties for ASTM A496 deformed wires

Property	Bar Size
	No. 2
Grade	60
Yield Stress, f_y	70.0 *ksi* (482.6 *MPa*)
Ultimate Tensile Strength, f_u	107.2 *ksi* (739.1 *MPa*)
Strain at Peak Stress, ε_u	0.0632 *in./in.*
Strain at fracture	0.146 *in./in.*

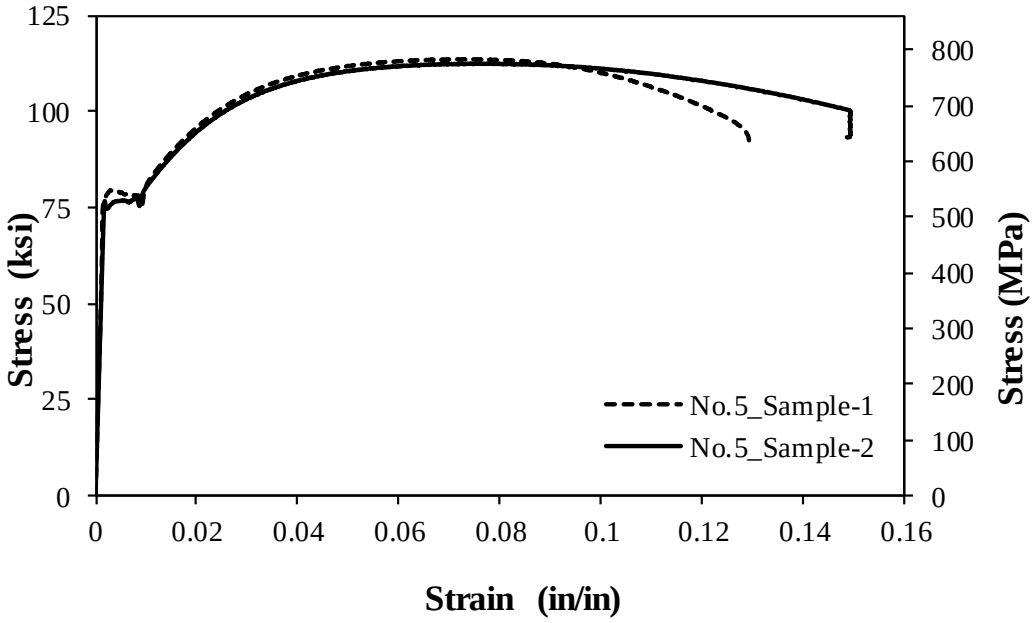

Figure 4-28. Measured stress-strain relationship for No. 5 deformed reinforcing steel bar

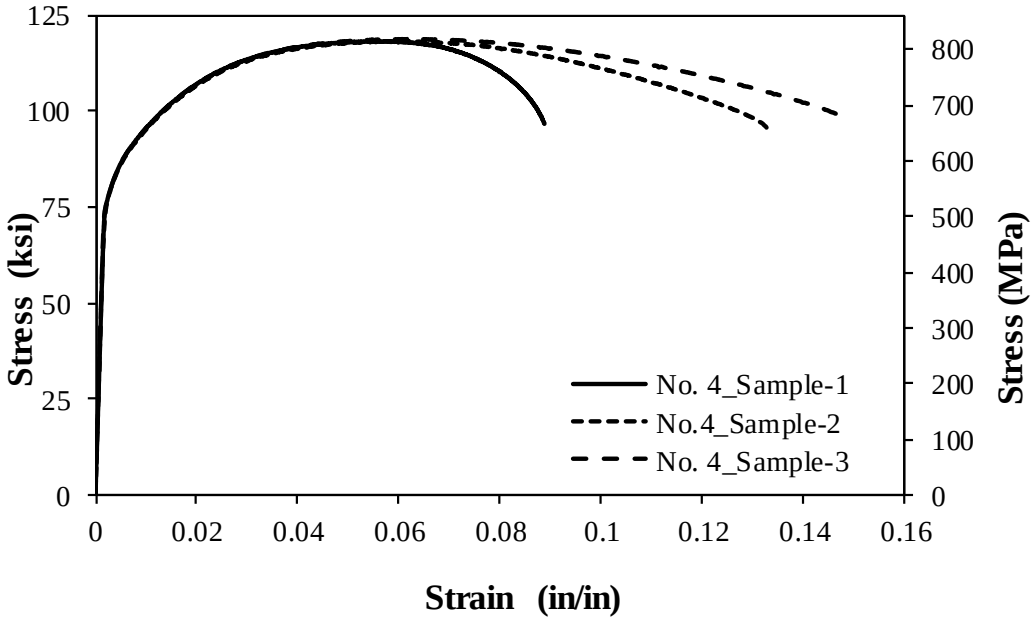

Figure 4-29. Measured stress-strain relationship for No. 4 deformed reinforcing steel bar

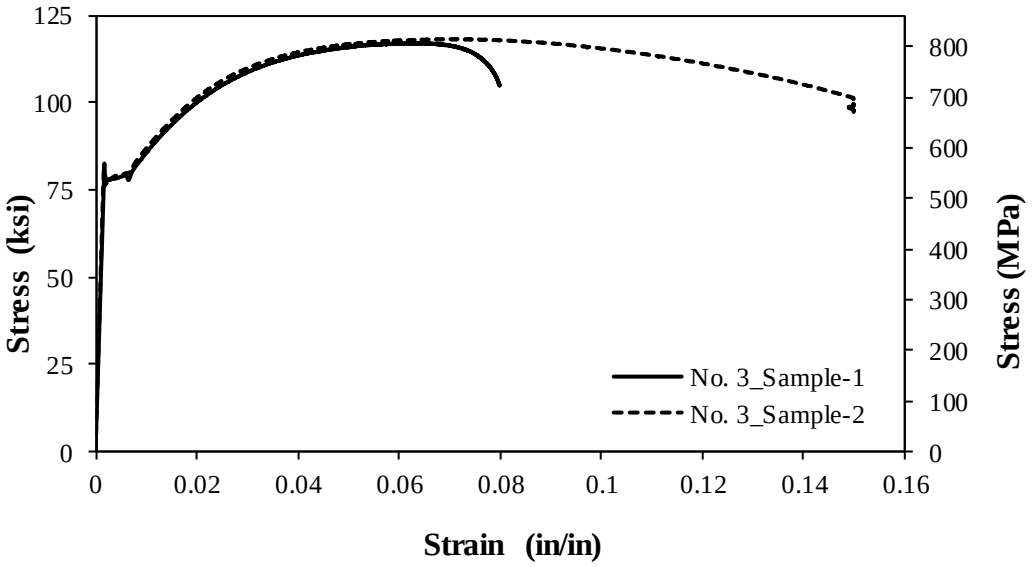

Figure 4-30. Measured stress-strain relationship for No. 3 deformed reinforcing steel bar

4.7.3. Observed Damage

The damages and crack pattern were monitored throughout the test. The specimen withstand more than 20 full cycles before reinforcement fracture at the bottom of the beam at 2.53 *in.* (3.51% drift ratio). Figures 4-31 to 4-36 show the damage of the beam-column specimen at different drift ratios. During applying the column axial load before the lateral load testing, a few cracks formed on the beam (Fig. 4-31a) due to vertical reaction at the beam free end (roller support). The reaction was cancelled out by adjusting the actuator displacement prior to testing. The initial cracking slightly decreased the specimen stiffness in the push direction (defined as the direction in which the beam bottom reinforcement is in tension) but the overall effect of these cracks was insignificant since reinforcement did not yield.

The first crack was formed on the beam at a drift ratio of 0.34% during the second cycle of 0.36% drift ratio. More cracks were observed at 1.46% drift ratio mainly in the plastic hinge region (0.5*h*, where *h* is the depth of beam). Cracks were also observed outside the plastic hinge region at higher drift ratios. Beam concrete

cover spalled at the column interface at a drift ratio of 2.19% (Fig. 4-34b). However, there was no concrete cover spalling for columns in the entire test. Only one crack was observed on the column at 3.5% drift ratio (Fig. 4-35b). The first tensile reinforcement yielded at SG 1 (Fig. 4-31a) at 0.19% push drift ratio during the first cycle of 0.36%-drift ratio. This reinforcement fractured at 3.5% drift ratio during the second cycle of 3.64%- drift ratio.

It can be concluded from the damage states that the special moment-resisting beam-column specimen designed based on the current codes performed adequately since all damage was concentrated in the beam and the column had minimal damage. The “strong column, weak beam” philosophy was confirmed in this experiment.

(a) Drift ratio 0.09%

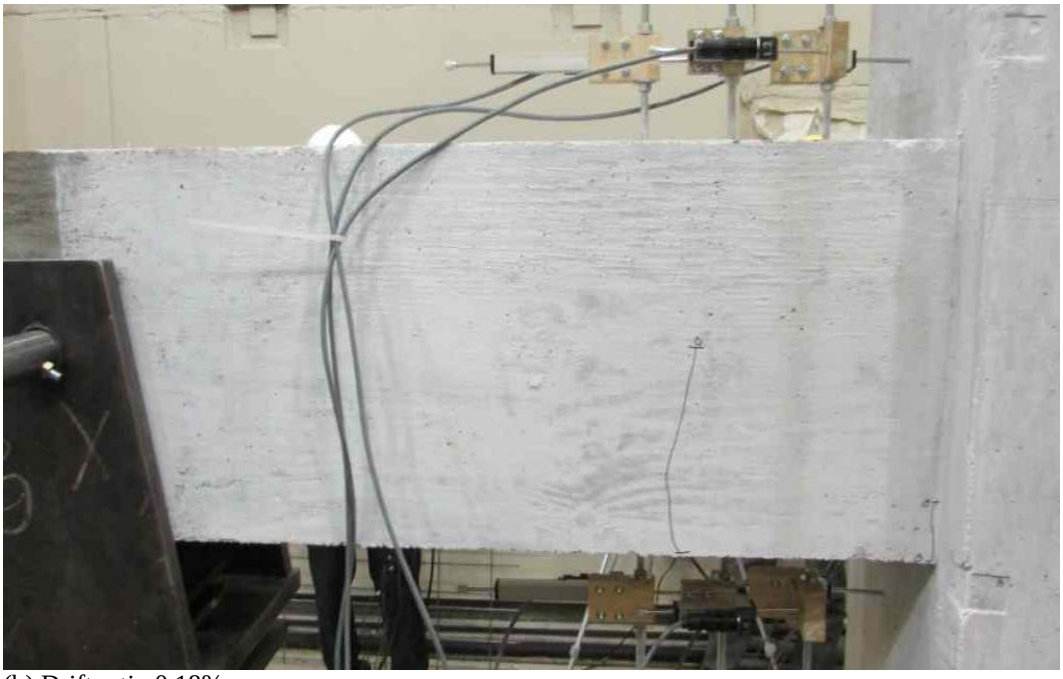

(b) Drift ratio 0.18%

Figure 4-31. Cracks pattern for beam-column joint at 0.09 and 0.18% drift ratio

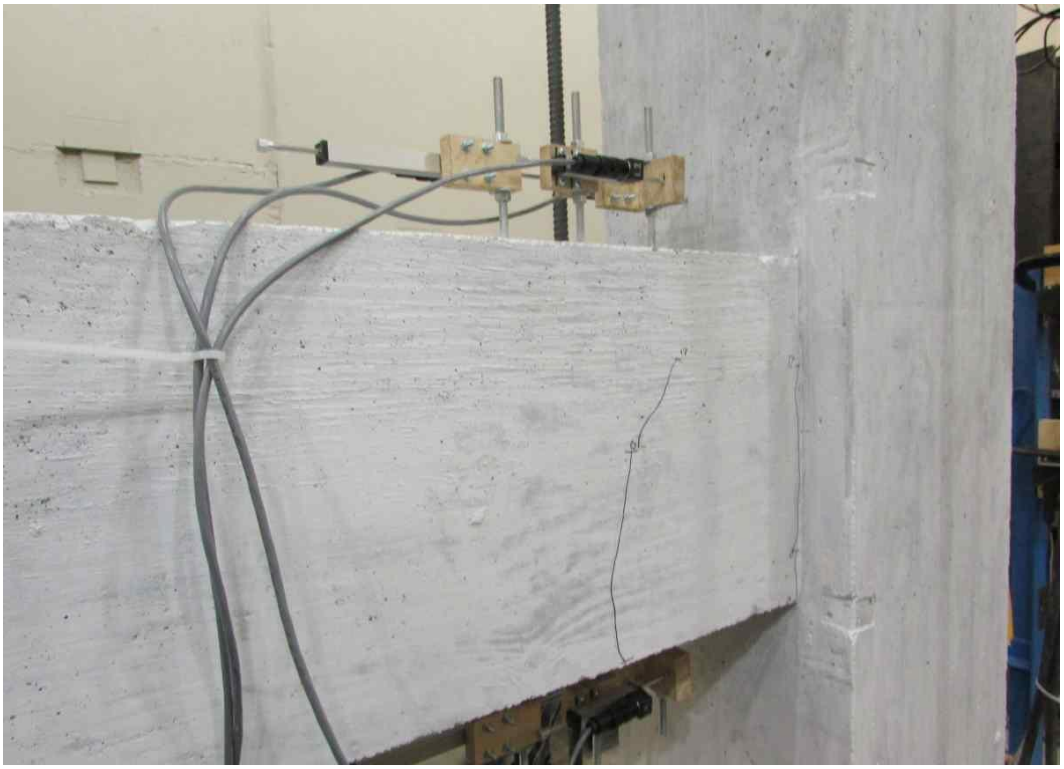

(a) Drift ratio 0.36%

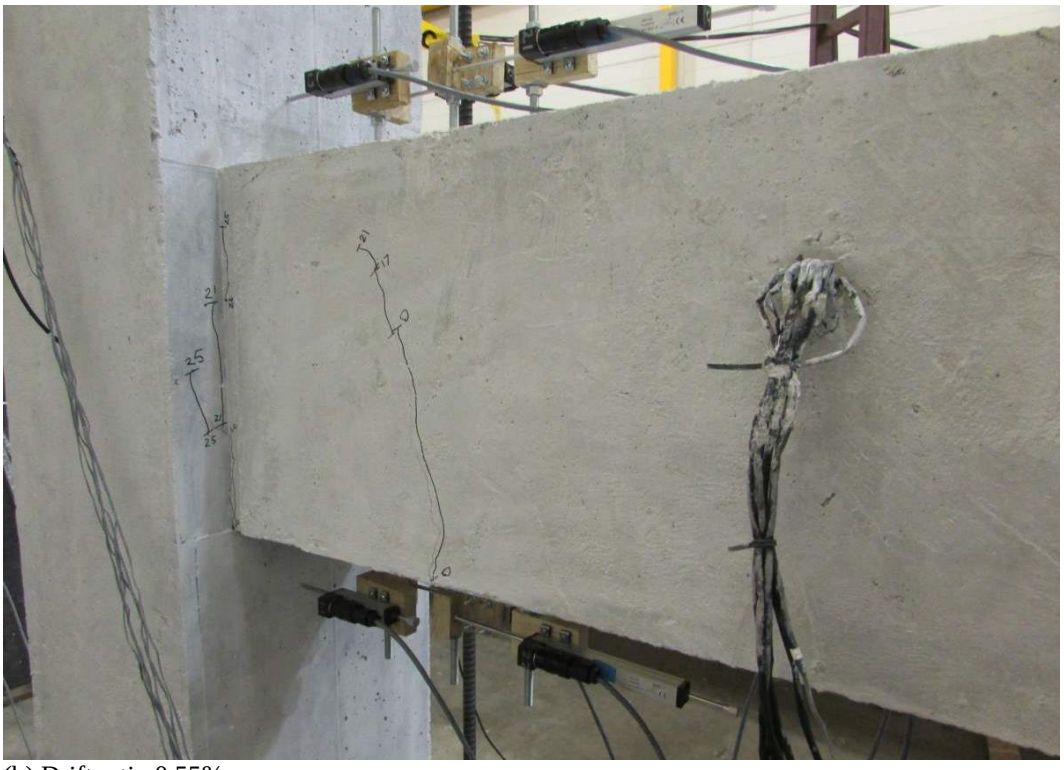

(b) Drift ratio 0.55%

Figure 4-32. Cracks pattern for beam-column joint at 0.36 and 0.55% drift ratio

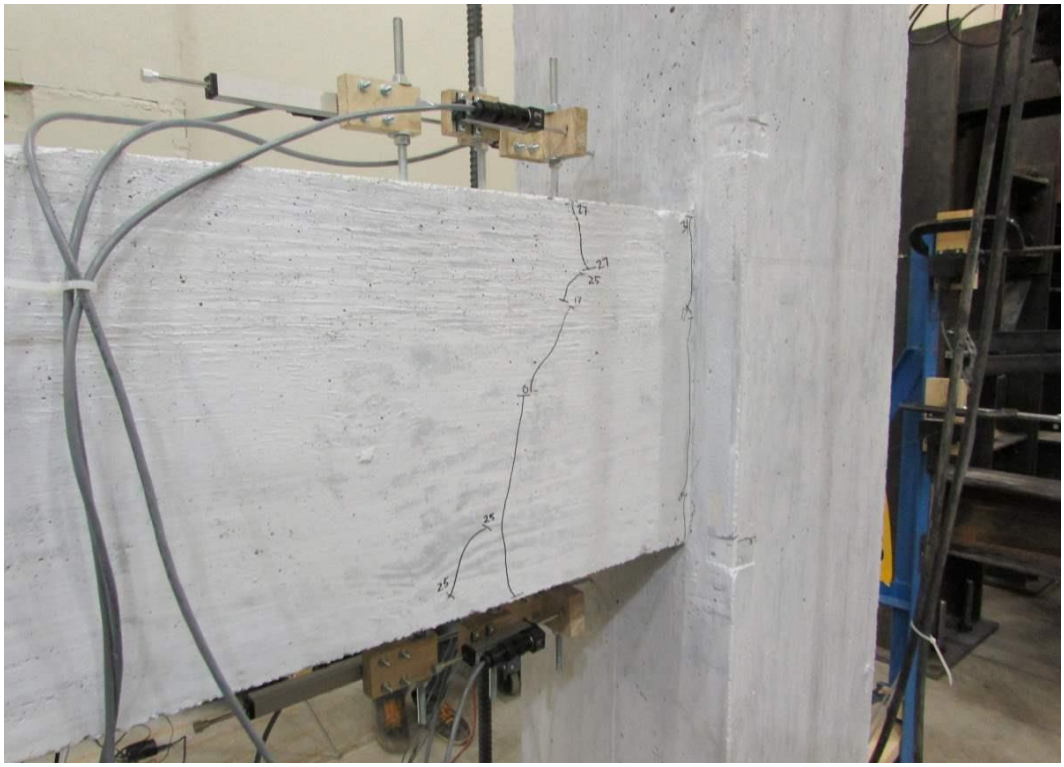

(a) Drift ratio 0.73%

(b) Drift ratio 1.09%

Figure 4-33. Cracks pattern for beam-column joint at 0.73 and 1.09% drift ratio

(a) Drift ratio 1.46%

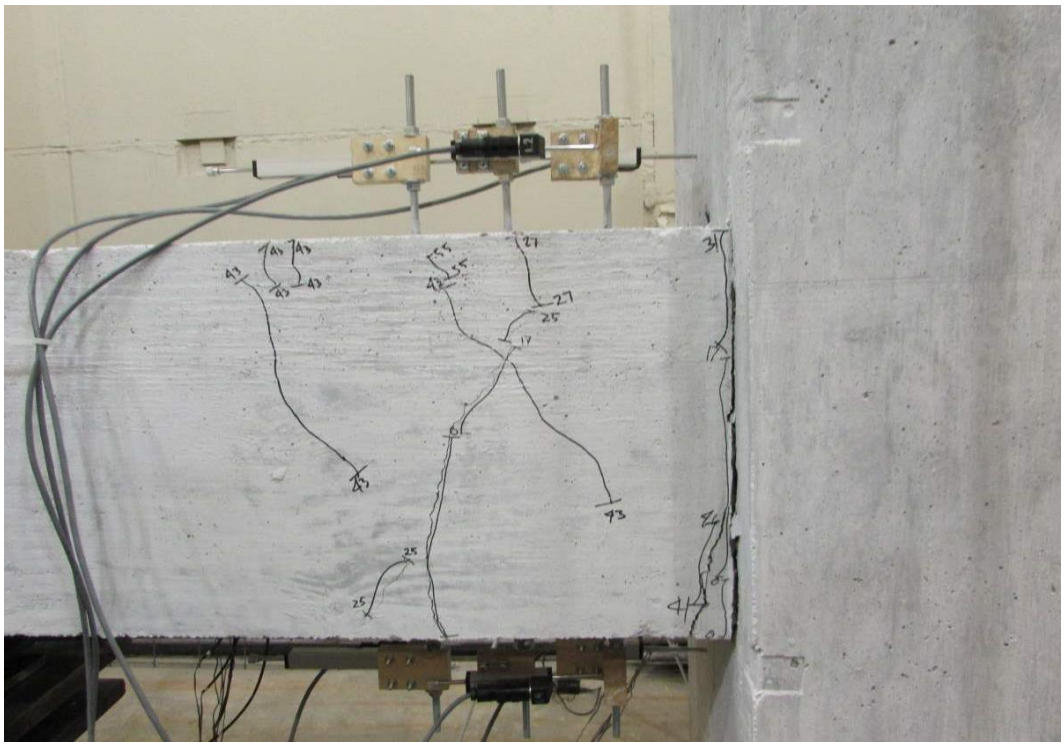

(b) Drift ratio 2.19%

Figure 4-34. Cracks pattern for beam-column joint at 1.46 and 2.19% drift ratio

(a) Drift ratio 2.90%

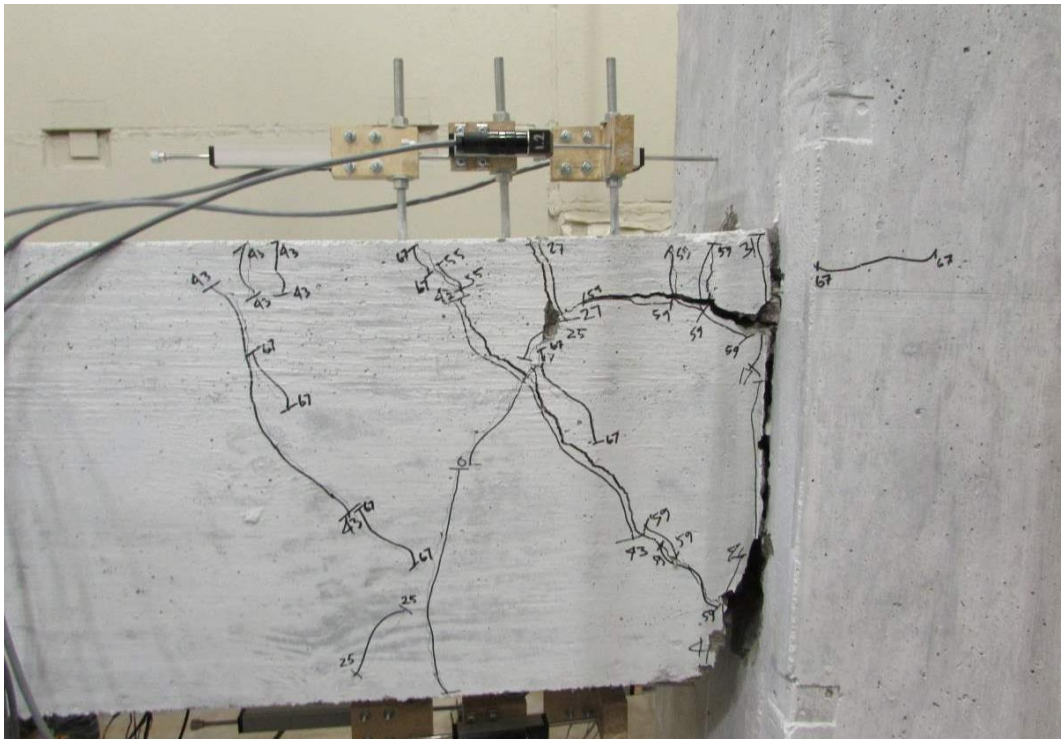

(b) Drift ratio 3.64% (failure)

Figure 4-35. Cracks pattern for beam-column joint at 2.9 and 3.64% drift ratio

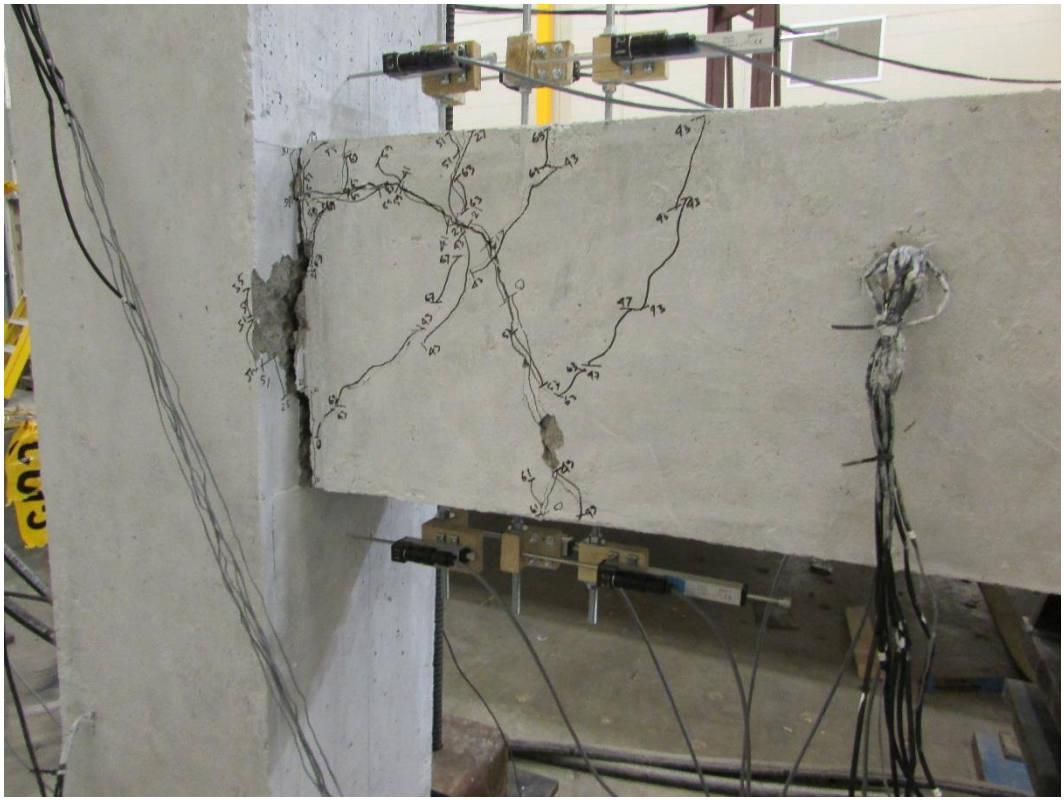

(a) East-Side

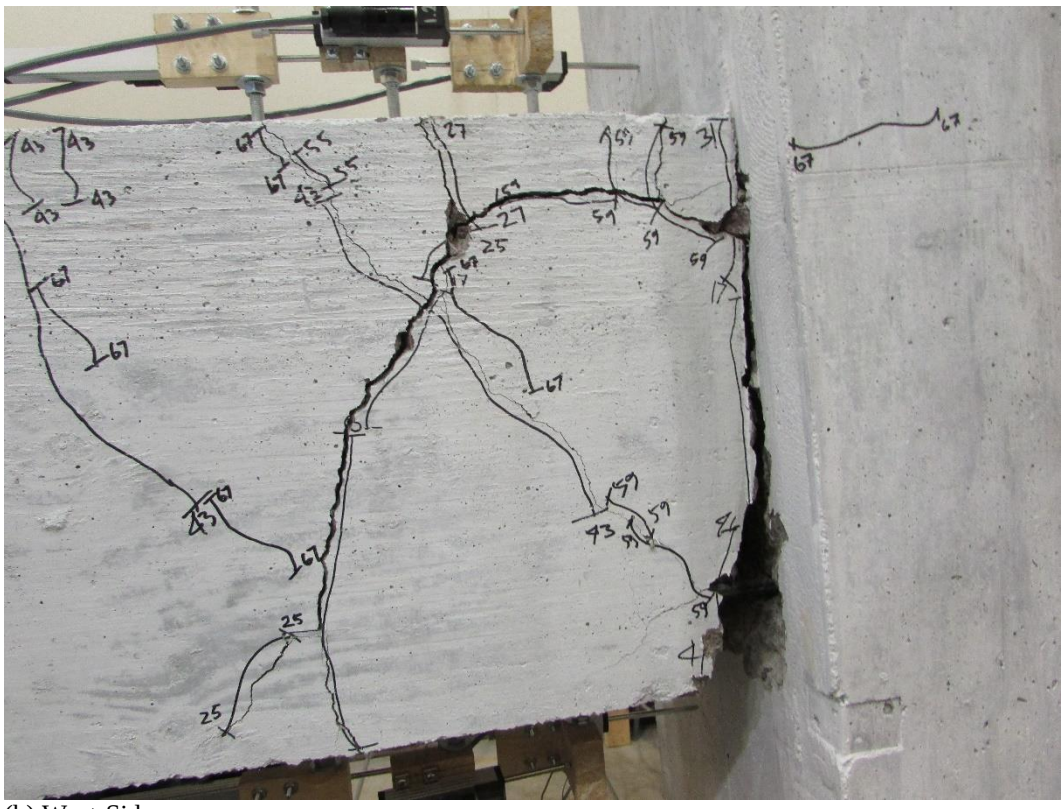

(b) West-Side

Figure 4-36. Cracks pattern for beam-column joint after testing

4.7.4. Force-Displacement Relationship

Figure 4-37 shows the measured force-displacement relationship of the test specimen. The force was the actuator force and the displacement was based on the string POT No. 3 (Fig. 4-26). The maximum lateral force in the push and pull direction was 7.98 (35.5) and 12.63 *kips* (56.2 *kN*), respectively. Note that the pull lateral strength was 58% higher than that in the push since the total area of the beam top reinforcement was 56% higher than that for the bottom reinforcement. The yield displacement and the yield force in the push direction was 0.13 *in.* (3.3 *mm*) and 5.63 *kips* (25 *kN*), respectively (Fig. 4-38). Similarly, the yield displacement and the yield force in the pull direction was 0.45 *in.* (11.4 *mm*) and 6.90 *kips* (30.7 *mm*), respectively. The ultimate displacement of the beam-column specimen was 2.53 *in.* (64.26 *mm*) at a lateral force of 12.63 *kips* (56.2 *kN*).

According to ASCE (2010), the allowable story drift ratio for this RC SMRF building is 2%. The drift ratio capacity of the beam-column specimen was 3.5% in the push direction and 3.59% in the pull direction. Therefore, this joint has at least 75% reserved capacity beyond the allowable drift ratio.

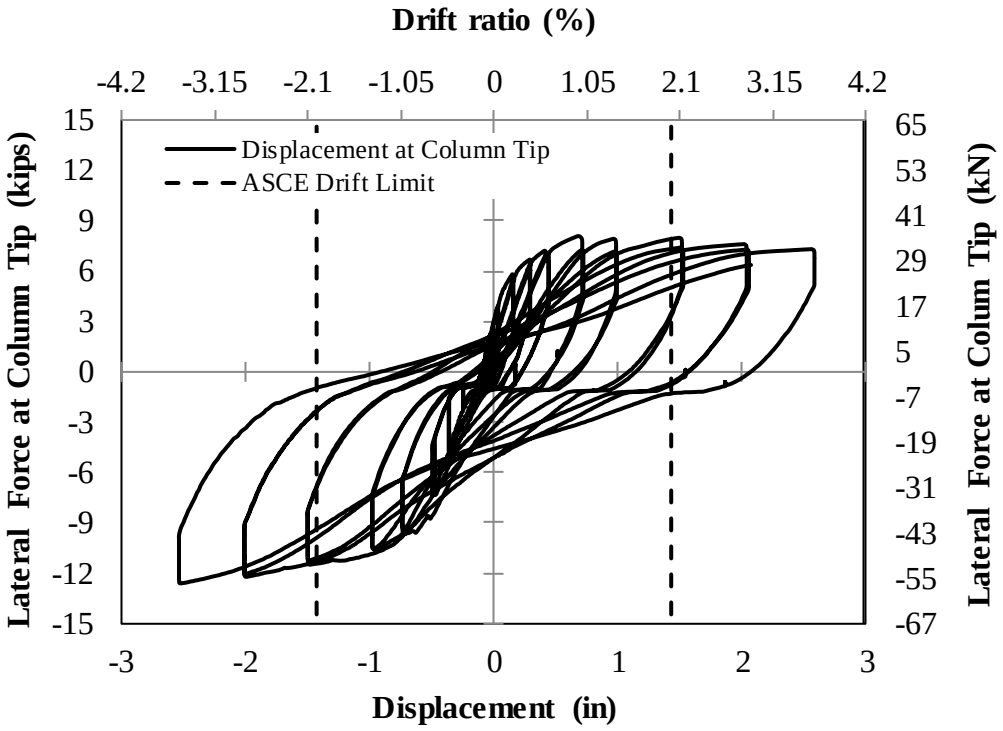

Figure 4-37. Lateral force-displacement relationship of beam-column specimen

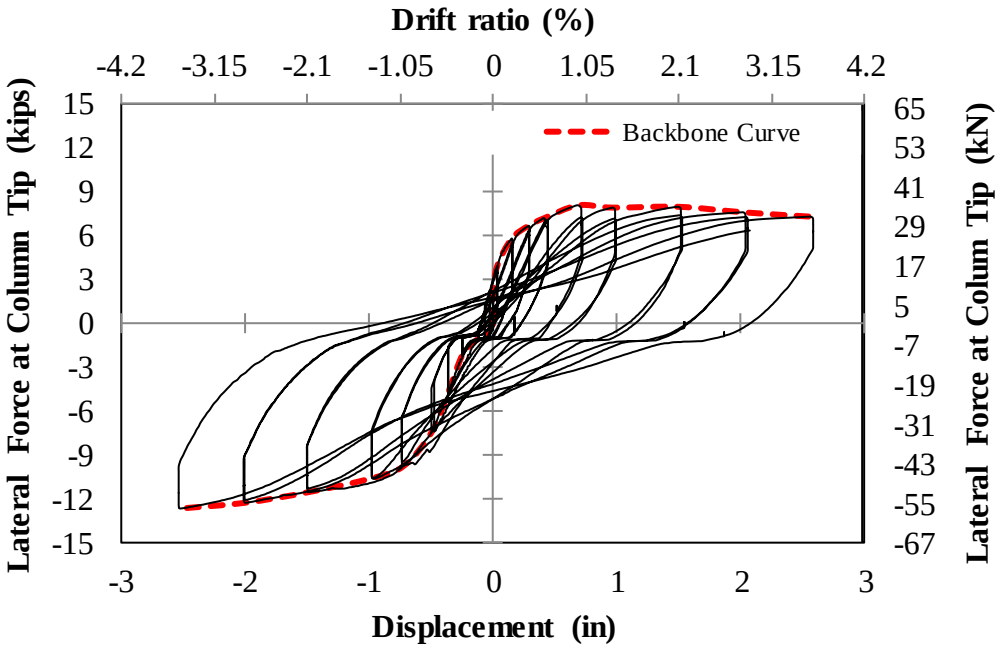

(a) Force-Displacement Envelope of Beam-Column Specimen

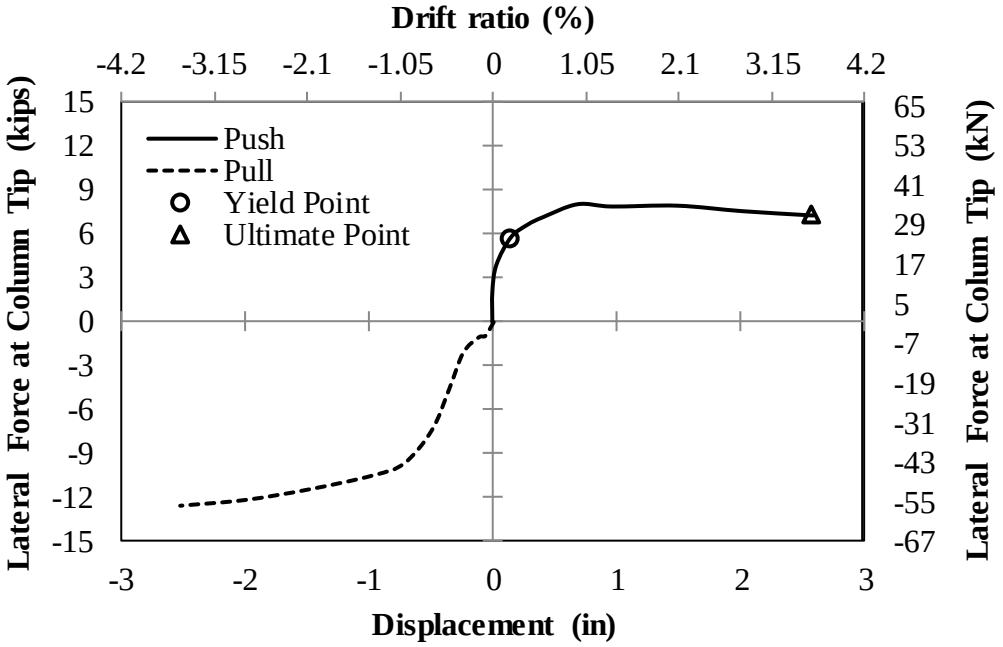

(b) Force-Displacement Envelope of Beam-Column Specimen

Figure 4-38. Force-displacement envelope for half-scale exterior beam-column joint

The beam roller support horizontal displacements (Fig. 4-39) and the joint rotations at the column face (Fig. 4-40) were measured using string POTs 1 and 2 (Fig. 4-26). The maximum measured horizontal displacement of the roller was 1.29 *in*. (32.77 *mm*). The beam roller support reaction was also calculated from the

measured lateral load and the equilibrium equations (Fig. 4-41). It can be seen that there is a good correlation between the measured and the calculated (from statics) responses.

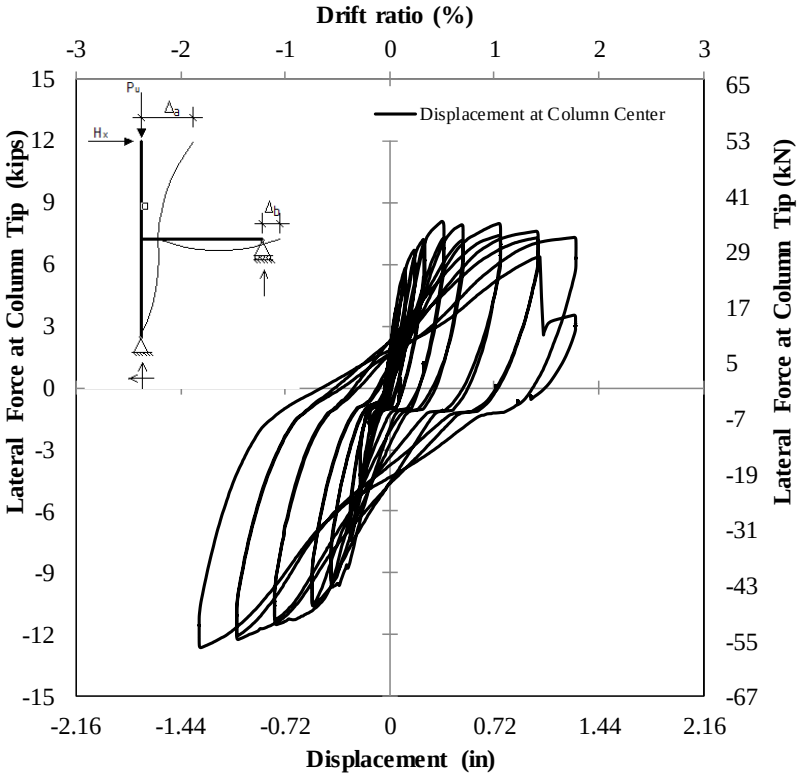

Figure 4-39. Horizontal displacement of beam roller support

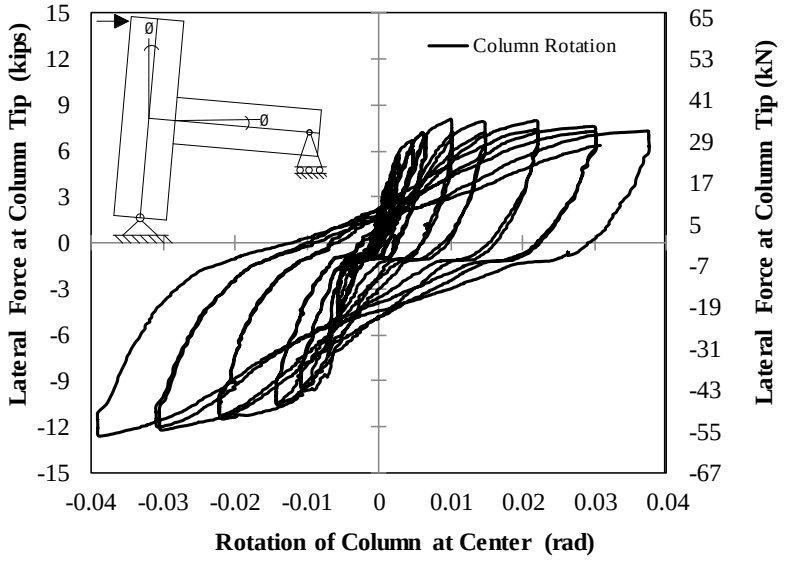

Figure 4-40. Column face rotation

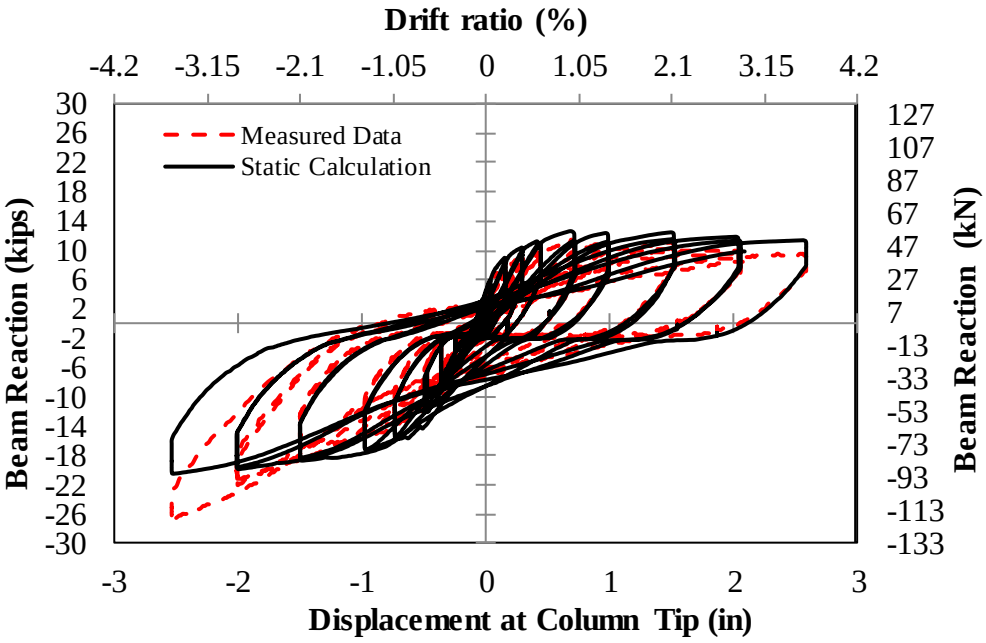

Figure 4-41. Beam end reaction for beam-column specimen

4.7.5. Moment-Curvature Relationship

Plastic rotations were measured in the beam plastic hinge region. Figure 4-42 shows the beam rotation measured at the column interface at each cycle. The curvature was also measured at three different locations of the beam from column face using the measured rotations (Fig. 4-43). It can be seen that that the beam curvature is higher close to the column interface indicating concentration of plasticity.

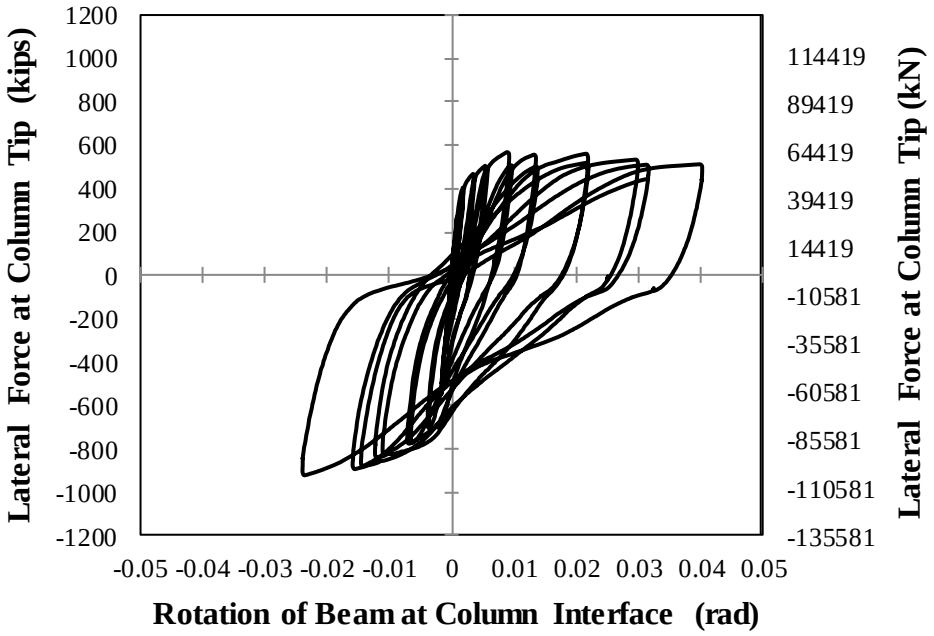

Figure 4-42. Moment - rotation relationship for beam at column interface

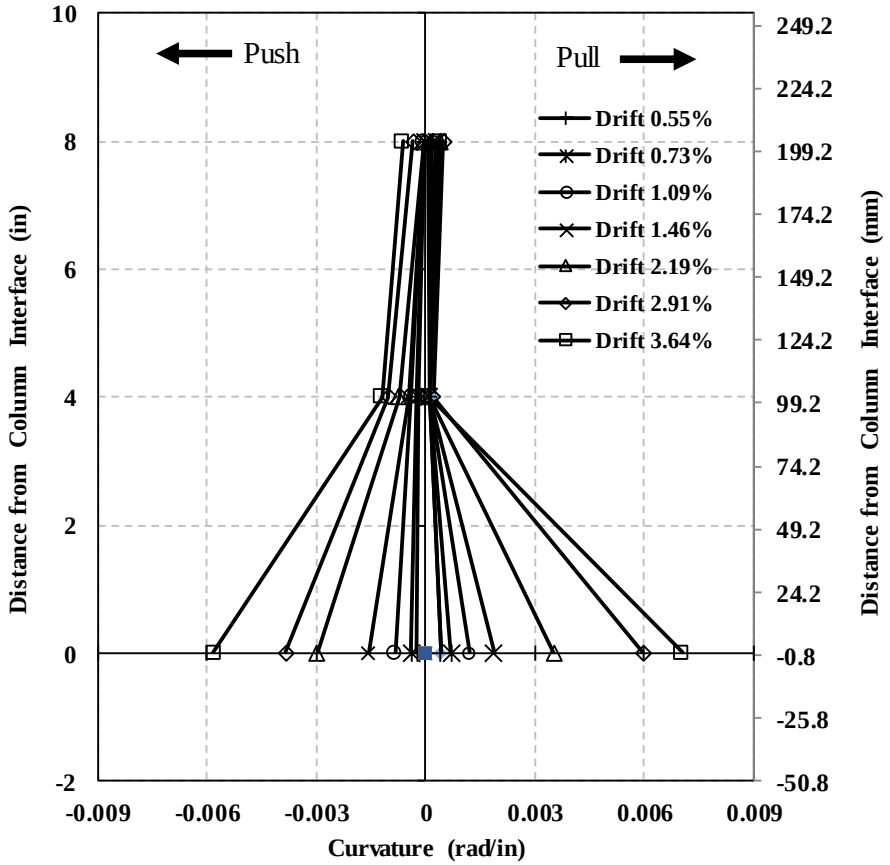

Figure 4-43. Curvature profile for beam at different drift ratio

4.7.6. Strain Profile

Strains were measured for both longitudinal and transverse reinforcing bars of the beam and column. The test data showed that the column longitudinal reinforcing bars and the column transverse steel reinforcement did not yield during the cyclic loading. All column bar strains were significantly lower than the yield strain. Therefore, the column damage will be minimal during severe earthquakes if RC frames are designed as SMRF. Nevertheless, the beam bottom longitudinal bars yielded then fractured. Figure 4-44 shows the strain profile of the beam longitudinal top and bottom reinforcement. The test data showed that the beam stirrups yielded close the beam-column interface but did not failed during the test.

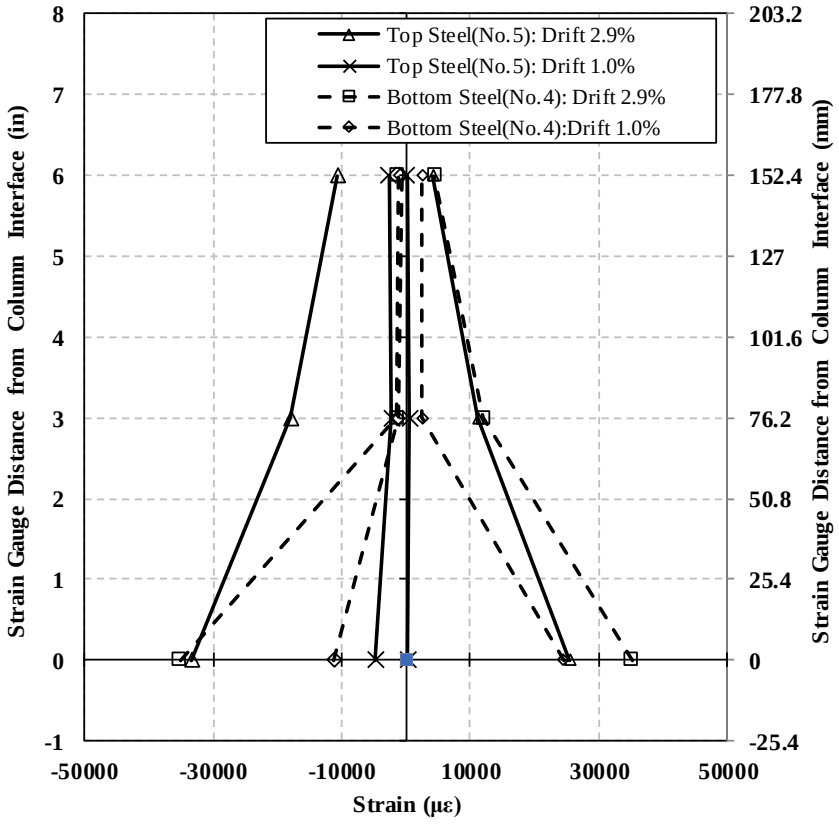

Figure 4-44. Strain profile for beam longitudinal reinforcement

4.7.7. Residual Displacements

In cyclic hysteresis, residual displacement is the displacement at the intersection of the unloading curves with zero forces. Figure 4-45 shows the residual drift versus the peak drift of the beam-column specimen. The residual drift is the ratio of the residual displacement to the column height, which was 72 *in*. (1828.8 *mm*). The specimen exhibited large residual displacements. Figure 4-46 shows the damage of the beam-column specimen at zero forces subsequent to peak drifts simulating the specimen damage after an earthquake.

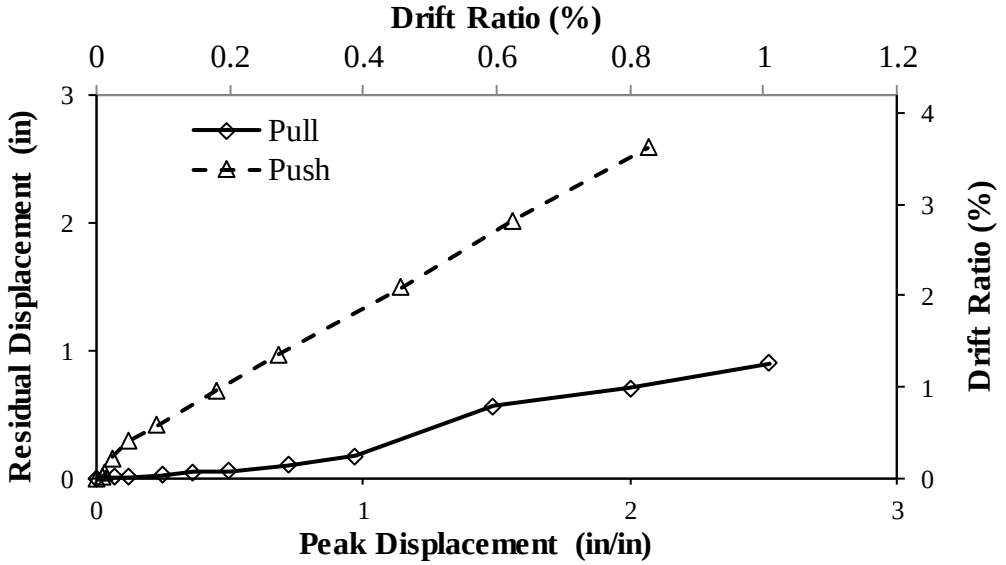

Figure 4-45. Residual displacement of beam-column joint

(a) After drift ratio of 0.73% (east side)

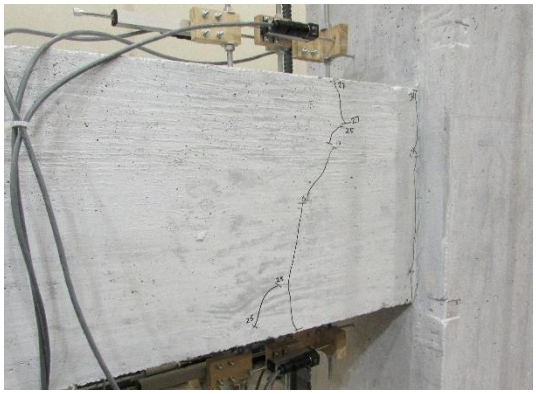

(b) After drift ratio of 0.73% (west side)

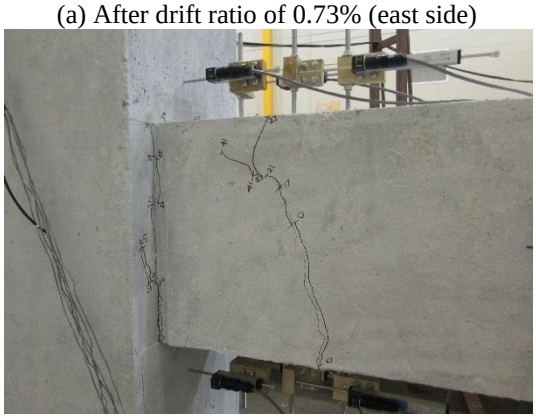

(c) After drift ratio of 1.09% (east side)

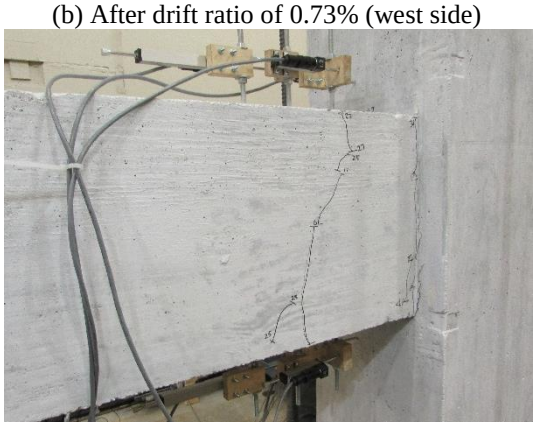

(d) After drift ratio of 1.09% (west side)

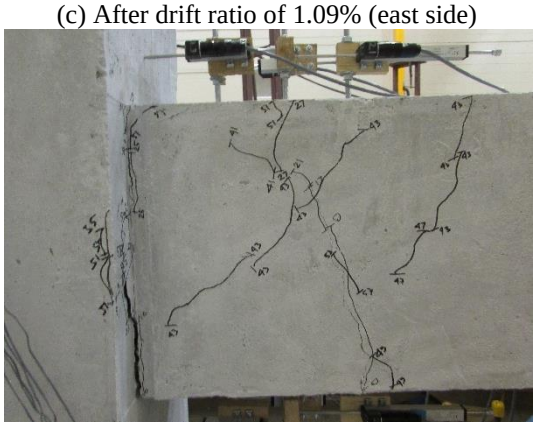

(e) After drift ratio of 2.19% (east side)

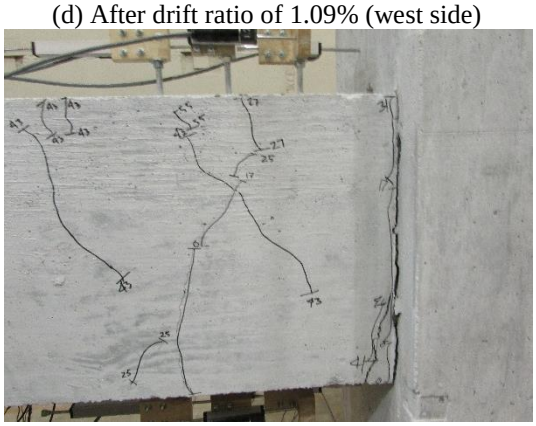

(f) After drift ratio of 2.19% (west side)

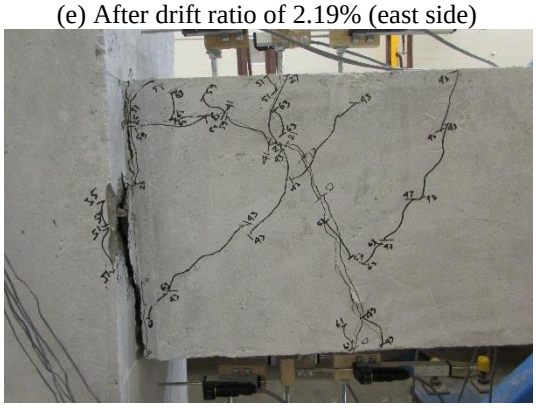

(g) After drift ratio of 2.91% (east side)

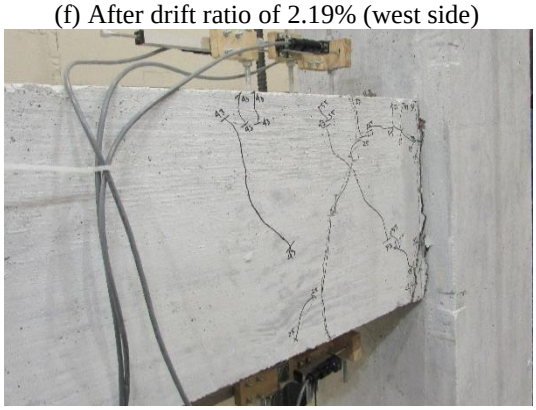

(h) After drift ratio of 2.91% (west side)

Figure 4-46. Damage of beam-column specimen at zero forces

4.8. Conclusions

The main objective of the present study was to investigate the structural behavior of a half-scale exterior beam-column joint of a nine-story special moment-resisting reinforced concrete building. A new boundary condition was incorporated to simulate the actual beam-column behavior. The following conclusions can be made based on the experimental data:

- Column longitudinal and transverse reinforcement did not yield under the cyclic loading and the column damage was insignificant. Therefore, beam-column joints of special moment resisting frames (SMRF) designed using current codes are sufficient to resist the joint shear stresses and to show minimal damage.
- Almost all cracks were formed in the beam. The beam longitudinal reinforcing bars yielded then fractured at a high drift ratio. Therefore, "strong-column, weak-beam" design philosophy can be achieved using current codes.
- The drift ratio of the beam-column connection was 3.5% in the push direction and 3.59% in the pull direction. The specimen exhibited 75% reserved capacity beyond the ASCE allowable drift ratio.

Overall, it can be concluded that special moment-resisting frames designed based on current codes are sufficient and exhibit larger displacements through yielding of the beam reinforcement. Damage of columns and joint regions is expected to be minimal.

4.9. References

1. American Concrete Institute (ACI) Committee 318 (2014). “Building code requirements for structural concrete and commentary,” ACI 318-14, ACI, Farmington Hills, MI.
2. American Concrete Institute (ACI) Committee 374 (2013). “Guide for testing reinforced concrete structural elements under slowly applied simulated seismic loads,” ACI 374.2R-13, ACI, Farmington Hills, MI.
3. AISC (2011). “Specification for structural steel buildings,” American Institute of Steel Construction, Inc., One East Wacker Drive, Suite 700, Chicago, Illinois 60601-1802
4. ASTM Standard C39-12 (2012). "standard test method for compressive strength of cylinder concrete specimens," ASTM International, West Conshohocken, PA.
5. ASTM Standard C143 (2012). "standard test method for slump of hydraulic-cement concrete," ASTM International, West Conshohocken, PA. doi:10.1520/C0143_C0143M-12
6. ASTM Standard C617-12 (2012). "standard practice for capping cylindrical concrete specimens," ASTM International, West Conshohocken, PA.
7. ASTM Standard A706/A706M-09b (2009),” Standard specification for low-alloy steel deformed and plain bars for concrete Reinforcement,” ASTM International, West Conshohocken, PA.
8. ASTM Standard E8/E8M-11 (2011). “Standard test methods for tension testing of metallic materials,” ASTM International, West Conshohocken, PA.

9. ASTM Standard A-496 (2007), “Standard specification for steel wire, deformed, for concrete reinforcement,” ASTM International, West Conshohocken, PA
10. ASTM International. A*370*-12 (2012). “Standard Test Methods and Definitions for Mechanical Testing of Steel Products,” ASTM International, West Conshohocken, PA, DOI: 10.1520/A0370-12a."
11. ASCE Standard (2010). “Minimum design loads for buildings and other structures,” American Society of Civil Engineers (ASCE), 1801 Alexander Bell Drive, Reston, Virginia 20191.
12. Alva, G.M.S. and de Cresce El, A.L.H. (2013). “Moment–rotation relationship of RC beam-column connections: Experimental tests and analytical model,” Engineering Structures, *56*, pp.1427-1438.
13. Durrani, A. J., & Wight, J. K. (1985). "Behavior of interior beam-to-column connections under earthquake-type loading," Paper presented at the Journal Proceedings.
14. Ehsani, M., Moussa, A., and Valenilla, C. (1987). "Comparison of inelastic behavior of reinforced ordinary-and high-strength concrete frames," Structural Journal, 84(2), 161-169.
15. Ehsani, M., and Wight, J. (1985). "Exterior reinforced concrete beam-to-column connections subjected to earthquake-type loading," Paper presented at the Journal Proceedings.
16. Filippou, F. C., D’Ambrisi, A., and Issa, A. (1999). "Effects of reinforcement slip on hysteretic behavior of reinforced concrete frame members," Structural Journal, 96(3), 327-335.

17. Fujii, S., and Morita, S. (1991). "Comparison Between Interior and Exterior R/C Beam-Column Joint Behavior," Special Publication, 123, 145-166.
18. Haach, V. G., El, A. L. H. D. C., and El Debs, M. K. (2008). "Evaluation of the influence of the column axial load on the behavior of monotonically loaded R/C exterior beam–column joints through numerical simulations," Engineering Structures, 30(4), 965-975.
19. Hwang, S.-J., Lee, H.-J., Liao, T.-F., Wang, K.-C., and Tsai, H.-H. (2005). "Role of hoops on shear strength of reinforced concrete beam-column joints," ACI Structural Journal-American Concrete Institute, 102(3), 445-453.
20. IEBC Standard (2012). "International existing building code," International code council, Inc., Country Club Hills, IL
21. Joh, O., Goto, Y., and Shibata, T. (1991). "Influence of Transverse Joint and Beam Reinforcement and Relocation of Plastic Hinge Region on Beam Column Joint Stiffness Deterioration," Special Publication, 123, 187-224.
22. Krawinkler, Helmut, and Piotr D. Moncarz (1982). "Similitude requirements for dynamic models," Special Publication, 73, pp. 1-22
23. Li, B., Tran, C.T.N. and Pan, T.C. (2009). "Experimental and numerical investigations on the seismic behavior of lightly reinforced concrete beam-column joints," Journal of structural engineering, 135(9), pp.1007-1018.
24. Mander, J., Priestley, M., & Park, R. (1988) "Observed stress-strain behavior of confined concrete," Journal of structural engineering, 114(8), 1827-1849
25. OpenSees. (2013). “Open System for Earthquake Engineering Simulations,” Version 2.4.1, Berkeley, CA, Available online: http://opensees.berkeley.edu

26. Paulay, T., Park, R., and Preistley, M. (1978). "Reinforced concrete beam-column joints under seismic actions," Paper presented at the Journal Proceedings.
27. Quintero-Febres, C. G., & Wight, J. K. (2001). "Experimental study of reinforced concrete interior wide beam-column connections subjected to lateral loading," Structural Journal, 98(4), 572-582.
28. SAP2000 (2016). “Integrated finite element analysis and design of structures,” CSI, Berkeley California
29. Scott, R. H. (1996). "Intrinsic mechanisms in reinforced concrete beam-column connection behavior," ACI Structural Journal," 93(3), 336-346.
30. Tsonos, A.G. (1999). "Lateral load response of strengthened reinforced concrete beam-to-column joints," *ACI Structural Journal*, *96*, pp.46-56.
31. Tsonos, A. G. (2007). "Cyclic load behavior of reinforced concrete beam-column subassemblages of modern structures," ACI Structural Journal, 104(4), 468.
32. Youssef, M.A., Alam, M.S. and Nehdi, M. (2008). "Experimental investigation on the seismic behavior of beam-column joints reinforced with superelastic shape memory alloys," Journal of Earthquake Engineering, 12(7), pp.1205-1222.
33. Zhou, H. (2009). "Reconsideration of seismic performance and design of beam-column joints of earthquake-resistant reinforced concrete frames," Journal of structural engineering, 135(7), 762-773.

CHAPTER 5. ANALYTICAL STUDIES

5.1. Introduction

Analytical studies were carried out to investigate the seismic performance of the special moment-resisting reinforced concrete beam-column test specimen as well as reinforced concrete bridge columns confined with rubber. The detail of analytical studies are reported herein.

5.2. Analytical Studies of Beam-Column Test Specimen

Robust analytical tools are required to accurately analyze and design structural components, assess damage, and estimate their capacities. Analytical modeling methods were proposed in this section to reproduce the overall response of the half-scale beam-column specimen tested under cyclic loading as discussed in the previous section. OpenSees (2013) was used for the analysis of the test model. Calculated results are compared with those measured in the test. Table 5-1 presents the main parameters of the beam-column test specimen.

Table 5-1. Parameters for half-scale beam-column test model

Parameter	Column	Beam
Length	72 *in.* (1828.8 *mm*)	45 *in.* (1143 *mm*)
Width	15 *in.* (381 *mm*)	10 *in.* (254 *mm*)
Depth	15 *in.* (381 *mm*)	15 *in.* (381 *mm*)
Size of longitudinal reinforcement	No. 5	Top: No. 5 Bottom: No. 4
Total number of longitudinal reinforcement	8	Top: 2 Bottom: 2
Diameter of longitudinal reinforcement	0.625 *in.* (15.9 *mm*)	Top: 0.625 *in.* (16 *mm*) Bottom: 0.5 *in.* (13 *mm*)
Size of transverse reinforcement	No. 3	No. 2
Diameter of transverse reinforcement	0.375 *in.* (6 *mm*)	0.25 *in.* (6 *mm*)
Type of transverse reinforcement	Ties	Stirrup
Spacing	3.5 *in.* (76 *mm*)	3.25 *in.* (83 *mm*)
Clear concrete cover	1.5 *in.* (38 *mm*)	1.5 *in.* (38 *mm*)
Axial load	68 *kips* (302.5 *kN*) ($5.6 f'_c.A_g$)	

5.2.1. Description of Beam-Column Specimen Analytical Model

A three-dimensional finite element fiber-section model was constructed in OpenSees (Fig. 5-1). Each section includes steel fibers, cover concrete fibers, and core concrete (confined) fibers as shown in the figures. The support under the column was considered as a pin (rocker) to allow rotation. The beam end support was considered as a roller to allow horizontal movement. The column axial load of 68 *kips* (302.5 *kN*) was applied at the top of the column (Node 3). The compressive strength of concrete at the test-day of the beam-column specimen was 5415 *psi* (37.4 *MPa*) as present in Table 5-2.

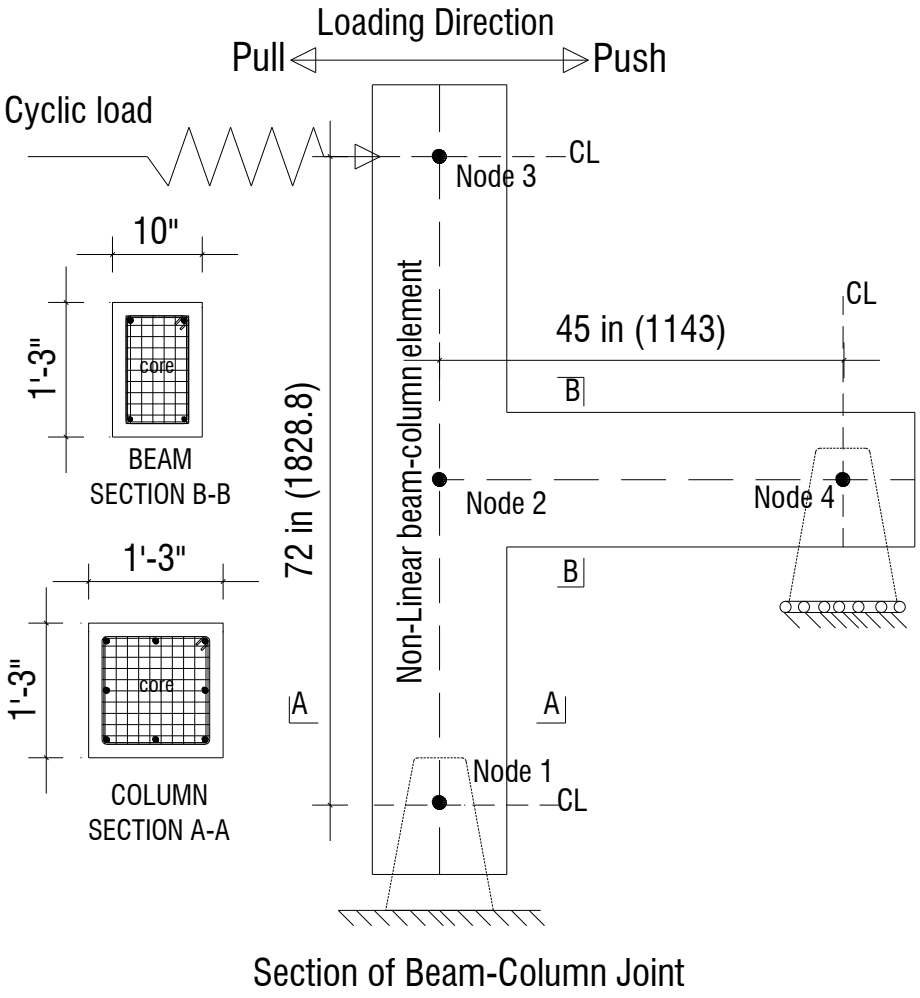

Figure 5-1. Beam-column joint analytical model

Table 5-2. Model parameters for unconfined concrete used in beam-column joint

Parameter	Value
Concrete compressive strength, f_c'	5.4 *ksi* (37.2*MPa*)
Strain at peak stress, ε_o	0.002 *in./in.*
Modulus of Elasticity, E_c	4194.4 *ksi* (28916.6 *MPa*)

A nonlinear force-based element, "forceBeamColumn", with five integration points was used for all beam and column elements. Steel fibers were modeled using "ReinforcingSteel" material model. The measured mechanical properties of steel was used in the analysis (Table 5.3). The compressive strength of concrete, 5415 *psi* (37.4 *MPa*), was used for the unconfined concrete fibers, which were modeled using "Concrete02". Mander's model (Mander et al., 1988) was used to determine the

confined concrete fiber parameters, which was also “Concrete02”. Note that concrete confinement properties were different for the beam and column (Table 5-4). The section discretization is schematically shown in Fig. 5-1. The core concrete was discretized with 50 layers in both directions. The concrete cover was discretized with 20 layers in both directions. Steel fibers were modeled with either “ReinforcingSteel” or “Steel02” material models using the measured mechanical properties at all integration points. Steel02 was selected for No. 4 bars because they did not show yielding plateau in the tensile tests (Fig. 4-29). Bond-slip effect was not included in the analysis. However, the P-Δ effect was included.

Table 5-3. Reinforcing steel (Longitudinal steel) material model properties used in beam-column analytical model

Parameter	**No. 4 Bar**	**No. 5 Bar**
Yield Stress, f_y	77.25 *ksi* (532.6 *MPa*)	76.85 *ksi* (529.9 *MPa*)
Ultimate Tensile Strength, f_u	118.25 *ksi* (815.3 *MPa*)	113.27 *ksi* (781.0 *MPa*)
Modulus of Elasticity, E_s	29000 *ksi* (200000 *MPa*)	29000 *ksi* (200000 *MPa*)
Strain at Peak Stress, ε_u	0.0597 *in./in.*	0.0742 *in./in.*
Strain at Fracture	0.125 *in./in.*	0.139 *in./in.*

Table 5-4. Fibers used in beam-column analytical model

Longitudinal Steel Fibers	
Column	Beam
Type: ReinforcingSteel Bar Size: No. 5 f_y = 78.65 *ksi* (529.9 *MPa*) f_{su} = 113.27 *ksi* (781.0 *MPa*) E_s = 29000 *ksi* (200000 *MPa*) ε_{sh} = 0.005 *in./in.* ε_{su} = 0.0742 *in./in.*	Type: Steel02 Bar Size: No. 4 f_y = 77.25 *ksi* (532.6 *MPa*) f_{su} = 118.25 *ksi* (815.3 *MPa*) E_s = 29000 *ksi* (200000 *MPa*) B_s = 0.*02478* Type: ReinforcingSteel Bar Size: No. 5 f_y = 78.65 *ksi* (529.9 *MPa*) f_{su} = 113.27 *ksi* (781.0 *MPa*) E_s = 29000 *ksi* (200000 *MPa*) ε_{sh} = 0.005 *in./in.* ε_{su} = 0.0742 *in./in.*
Unconfined Concrete Fibers	
Column	Beam
Type: Concrete01 f'_{cc} = -5415 *psi* (37.4 *MPa*) ε_{cc} = -0.002 *in./in.* ε_{cu} = -0.005 *in./in.*	Type: Concrete01 f'_{cc} = -5415 *psi* (37.4*MPa*) ε_{cc} = -0.002 *in./in.* ε_{cu} = -0.005 *in./in.*
Confined concrete Fibers (Mander's model)	
Column	Beam
Type: Concrete01 f'_{cc} = -7200 *psi* (49.6 *MPa*) ε_{cc} = -0.005 *in./in.* f'_{cu} = -5870 *psi* (40.5 *MPa*) ε_{cu} = -0.016 *in./in.*	Type: Concrete01 f'_{cc} = -6500 *psi* (44.8 *MPa*) ε_{cc} = -0.004 *in./in.* f'_{cu} = -5000*psi* (34.5 *MPa*) ε_{cu} = -0.011 *in./in.*

5.2.2. Analysis Results

Figure 5-2 shows the calculated and the measured force-displacement relationships of the beam-column specimen. Table 5-5 presents a summary of the analysis results. The calculated lateral force was slightly higher in the pull direction than the measured data. The calculated force-displacement behavior was very close to the measured data up to 2% drift ratio in the push direction. After that, the calculated lateral force was slightly higher than the measured data. However, the ultimate displacements were close to those measured in the test with less than 6% error. Overall, the general trend was reasonably simulated using the proposed modeling method.

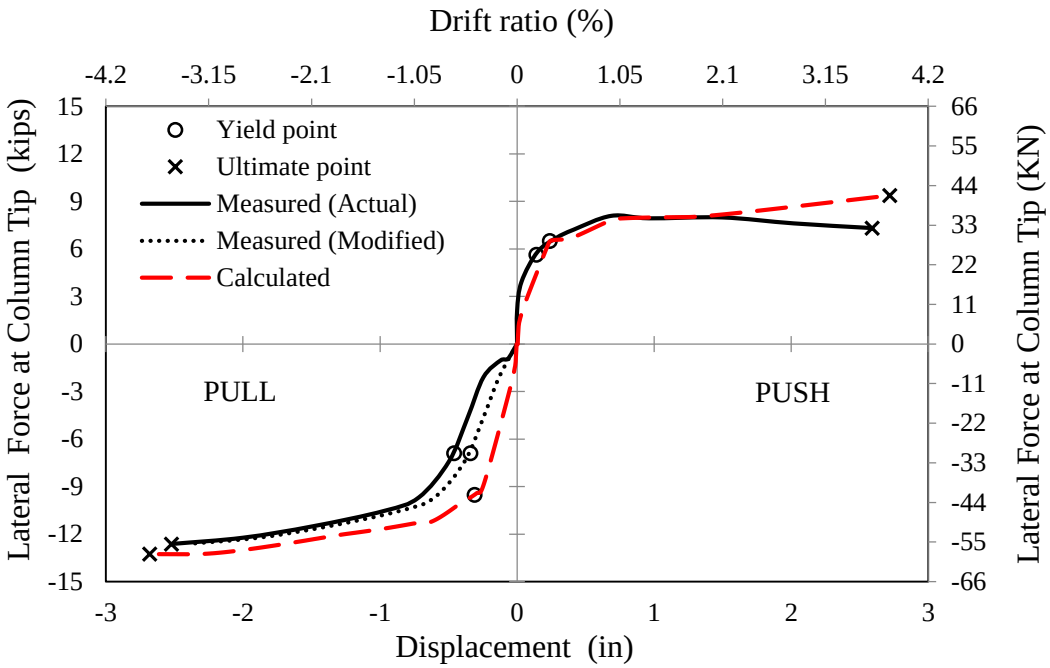

Figure 5-2. Calculated and measured force-displacement relationships for beam-column test model

Table 5-5. Measured and calculated response of beam-column test model

Parameter	**Measured**		**Calculated**	
	Push	Pull	Push	Pull
Yield displacement (*in.*)	0.13	0.45	0.24	0.31
Ultimate displacement (*in.*)	2.59	2.53	2.72	2.69
Maximum lateral force (*kips*)	7.98	12.63	9.38	13.27

Figure 5-3 shows the force-displacement hysteresis of the beam-column test model. Reasonable accuracy was achieved. However, the unloading behavior specially the pinching effect could not be fully reproduced.

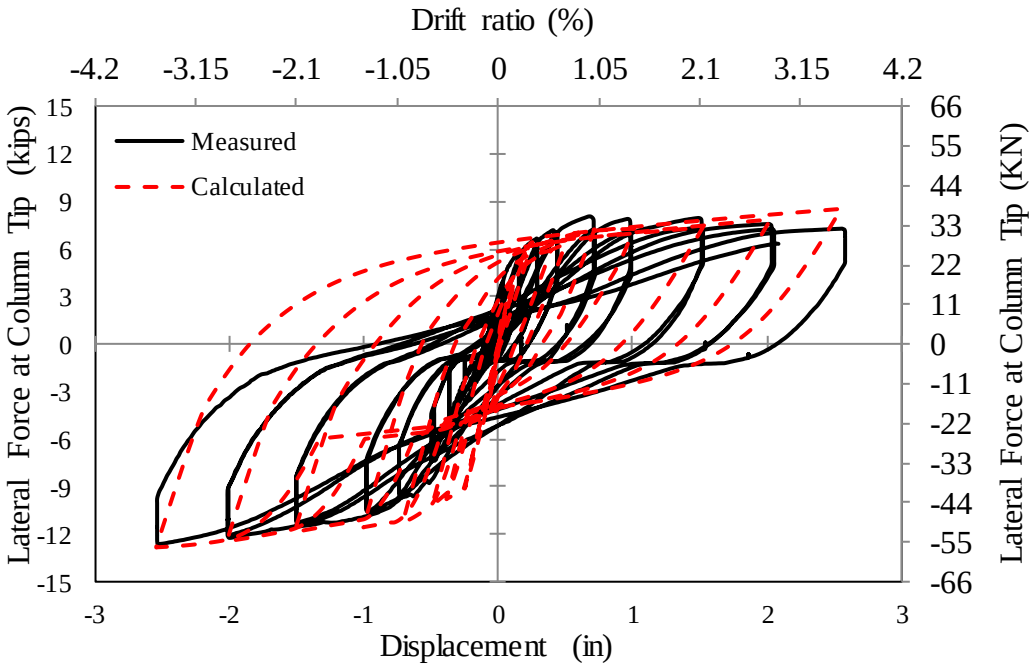

Figure 5-3. Calculated and measured force-displacement hysteresis for beam-column test model

5.3. Analytical Studies of Rubber Confined RC Bridge Columns

In recent years, repair, rehabilitation, and strengthening of existing bridges and buildings have been emphasized to elongate their lifetime. Some of these structures are damaged because of aging and others need strengthening because design codes have changed demanding higher forcers or allowing more stringent capacities. External jackets made of steel, concrete, or fiber-reinforced polymer are usually used to increase the ductility and strength of existing reinforced bridge columns. A new external confinement, rubber-coated concrete, was introduced in Chapter 2. Rubber confined concrete exhibits more than 10% strain capacity, which may be a viable alternative for current methods of repair, rehabilitation, or retrofit. The main purpose of this analytical study was to evaluate the seismic performance of low-ductile bridge columns confined with rubber.

To show the effect of rubber as a new confinement method on the displacement ductility capacity of bridge columns, three columns with different

displacement ductilities (3, 5, and 7) from Tazarv and Saiidi (2016) were selected for analytical studies (Table 5-6).

Table 5-6. Model parameters for conventional steel-confined circular bridge columns

Parameter	Column 1	Column 2	Column 3
Specimen ID	RC-AR4-ALI5-D3	RC-AR4-ALI5-D5	RC-AR4-ALI5-D7
Target Displacement Ductility (μ)	3	5	7
Column diameter	48 *in.* (1219 *mm*)	48 *in.* (1219 *mm*)	48 *in.* (1219 *mm*)
Column height	192 *in.* (4877 *mm*)	192 *in.* (4877 *mm*)	192 *in.* (4877 *mm*)
Size of longitudinal reinforcement	No. 9	No. 9	No. 9
Total number of longitudinal reinforcement	22	22	22
Diameter of longitudinal reinforcement	1.128 *in.* (29 *mm*)	1.128 *in.* (29 *mm*)	1.128 *in.* (29 *mm*)
Size of transverse reinforcement	No. 3	No. 4	No. 6
Diameter of transverse reinforcement	0.375 *in.* (9.5 *mm*)	0.5 *in.* (13 *mm*)	0.75 *in.* (19 *mm*)
Type of transverse reinforcement	Hoop	Hoop	Hoop
Pitch	12 *in.* (305 *mm*)	4 *in.* (305 *mm*)	4 *in.* (305 *mm*)
Clear concrete cover	2 *in.* (51 *mm*)	2 *in.* (51 *mm*)	2 *in.* (51 *mm*)
Axial load index [$P/(f'_c.A_g)$]	5%	5%	5%

5.3.1. Description of Bridge Column Analytical Model

A three-dimensional finite element fiber-section model was constructed in OpenSees (Fig. 5-4). The base of each column (node 1) was considered as fixed support and the axial load, which was 5% of the product of the column gross-section area and the compressive strength of concrete (axial load index), was applied to node 2 of all columns. The compressive strength of concrete at 28 days was taken as 5000 *psi* (34.5 *MPa*), present in Table 5-7.

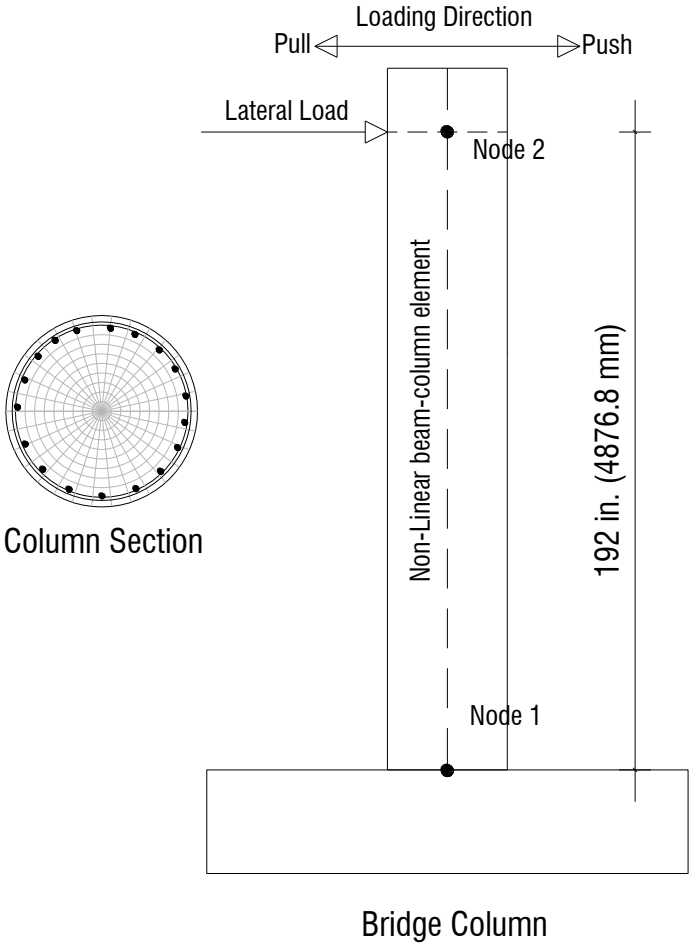

Figure 5-4. Bridge Column Analytical Model

Table 5-7. Conventional concrete properties assumed in bridge columns

Parameter	Value
Concrete compressive strength, f_c'	5 *ksi* (34.5 *MPa*)
Strain at peak stress, ε_o	0.002 *in./in.*
Modulus of Elasticity, E_c	4030.5 *ksi* (27789.3 *MPa*)

Since all bridges meet the current code minimum displacement ductility requirements ($\mu \geq 3$), the combined effect of confinement from rubber and reinforcing steel bars was used in the analytical models (Fig. 5-5 to 5-7). Mander's model (Mander et al., 1988) was used to determine the confinement properties of steel (Table 5-8). The confinement properties of rubber was determined using non-linear stress-strain relationship of rubber confined concrete (Table 5-9), which was descried in chapter 2.

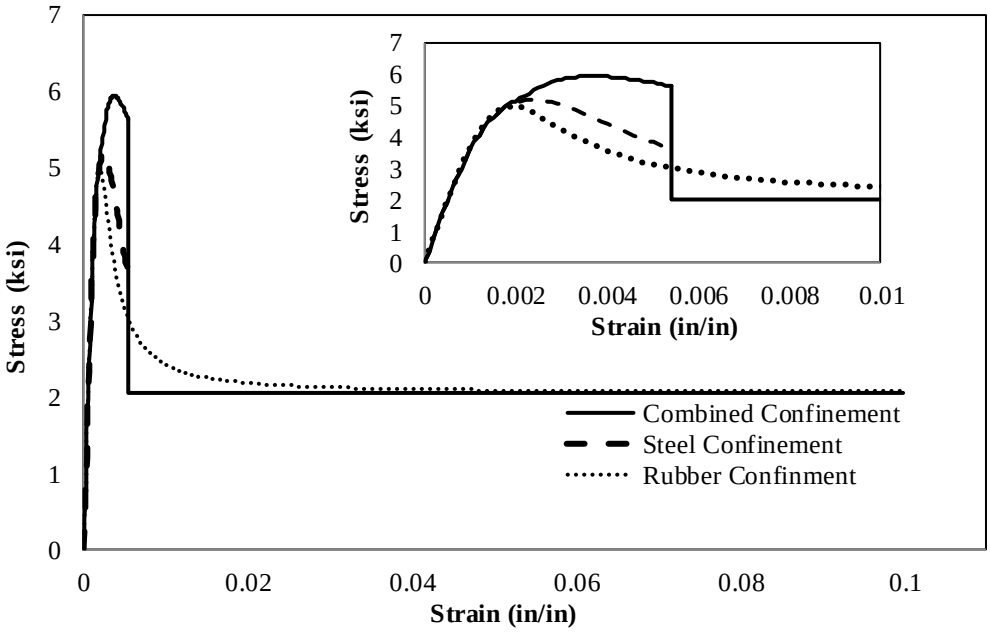

Figure 5-5. Stress-strain relationship for core concrete of low ductile bridge column ($\mu = 3$)

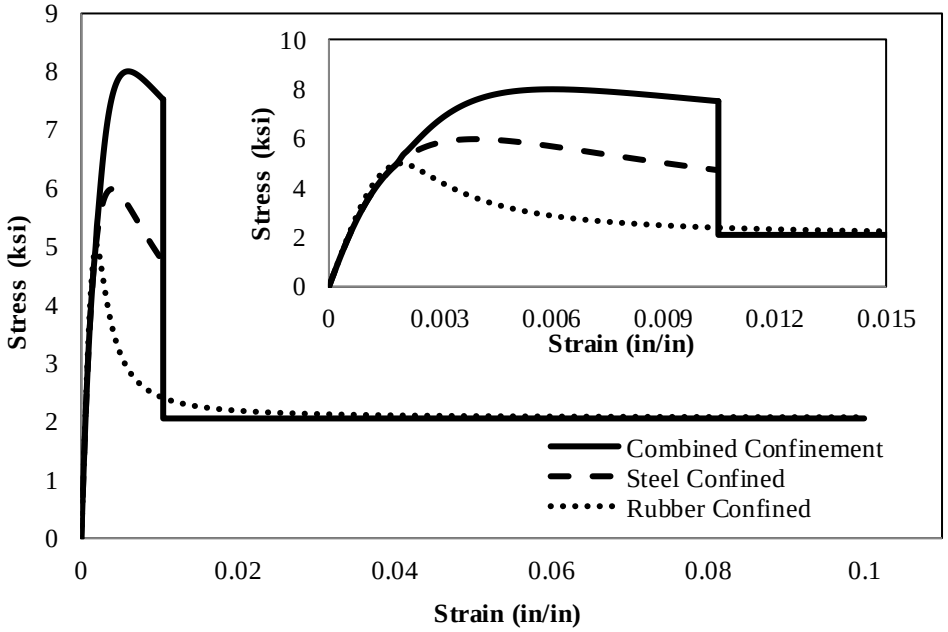

Figure 5-6. Stress-strain relationship for core concrete of moderate ductile bridge column ($\mu = 5$)

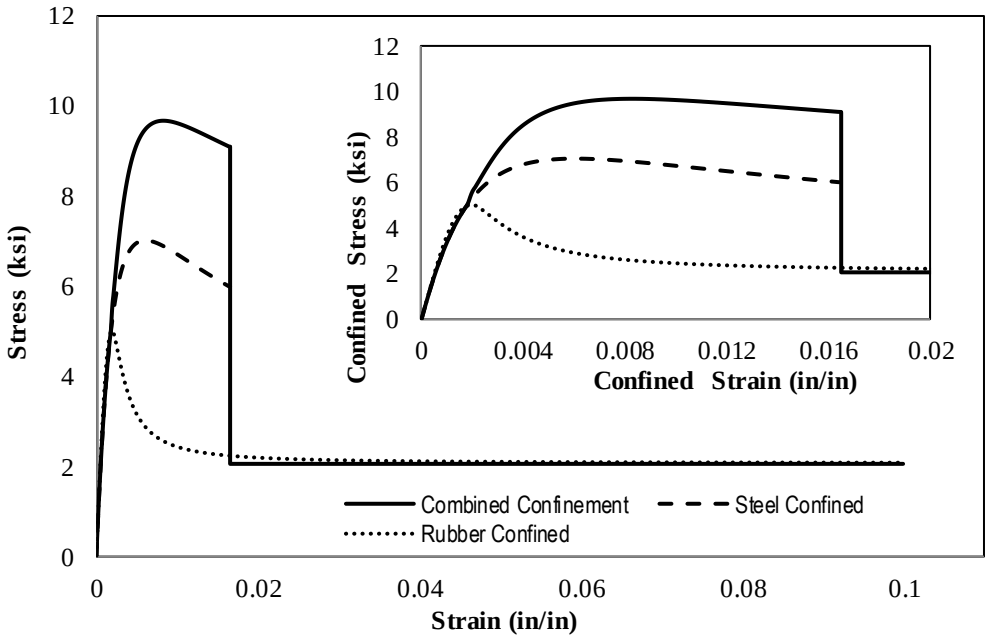

Figure 5-7. Stress-strain relationship for core concrete of high ductile bridge column ($\mu = 7$)

Table 5-8. Reinforcing steel material model properties used in bridge columns

Parameter	Value
Yield Stress, f_y	68 *ksi* (468.8 *MPa*)
Ultimate Stress, f_u	95 *ksi* (655.0 *MPa*)
Modulus of Elasticity, E_s	29000 *ksi* (200000 *MPa*)
Strain hardening stiffness, E_{sh}	1247 *ksi* (8783.9 *MPa*)
Strain at strain hardening, ε_{su}	0.005 *in./in.*
Yield Strain, ε_{ye}	0.0023 *in./in.*
Ultimate Strain, ε_u	0.09 *in./in.*

Table 5-9. Rubber confined concrete properties used in bridge columns

Parameter	Value
Rubber thickness, *t*	0.5 *in.* (12.7 *mm*)
Tensile strength of rubber, f_f	3432 *psi* (23.7 *MPa*)
Modulus of elasticity of rubber, E_f	56000 *psi* (386.1 *MPa*)
Compressive strength of confined concrete, f'_{cc}	5 *ksi* (34.5 *MPa*)
Strain at peak stress, ε_o	0.002 *in./in.*
Ultimate strain, ε_u	0.10 *in./in.*
Residual strength, f'_r	2.05 *ksi* (14.2 *MPa*)

The column element was modeled using a force-based element, "forceBeamColumn", with five integration points. Unconfined concrete fibers were modeled using "Concrete01" (Table 5-10). "Concrete 04" and "ElasticPPGap" material models were used as parallel springs to simulated the combined effect of

steel and rubber on confinement in which "Concrete 04" was used to model the steel confinement and "ElasticPPGap" material model was to simulate the residual strength from rubber confinement.

Table 5-10. Concrete cover and steel fiber properties used in bridge column models

Unconfined Concrete fibers	Steel fibers
Type: Concrete 01 f'_{cc} = -5 *ksi* (34.5 *MPa*) ε_{cc} = -0.002 *in./in.* f'_{cu} = -2.05 *ksi* (14.1 *MPa*) ε_{cu} = -0.005 *in./in.*	Type: ReinforcingSteel f_y = 68 *ksi* (468.8 *MPa*) f_{su} = 95 *ksi* (655.0 *MPa*) E_s = 29000 *ksi* (200000 *MPa*) E_{sh} = 1247 *ksi* (8783.9 *MPa*) ε_{sh} = -0.0125 *in./in.* ε_{su} = 0.09 *in./in.*

The column section discretization is also shown in Fig. 5-4. The core concrete was divided into 30 circumferential by 10 radial fibers, and the cover concrete was divided into 10 circumferential by 10 radial fibers. Steel fibers were modeled using "ReinforcingSteel" material model (Table 5-11). The bond-slip effect was not included but P-Δ effect was considered.

Table 5-11. Core concrete fiber properties used in bridge column models

Confined Concrete fibers: Column ID RC-AR4-ALI5-D3	
Type: Concrete 04 f'_{cc} = -5.40 *ksi* (37.23 *MPa*) ε_{cc} = -0.00238 *in./in.* f'_{cu} = -5.62 *psi* (38.75 *MPa*) ε_{cu} = -0.00539 *in./in.*	Type: ElasticPPGap f'_r = 2.05 *ksi* (14.2 *MPa*) E_c = 4030.5 *ksi* (27789.3 *MPa*)) ε_{su} = 0.1 *in./in.* Initial Gap = -0.00539 *in./in.*
Confined Concrete fibers: Column ID RC-AR4-ALI5-D5	
Type: Concrete 04 f'_{cc} = -7.52 *ksi* (51.85 *MPa*) ε_{cc} = -0.00395 *in./in.* f'_{cu} = -7.51 *psi* (51.78 *MPa*) ε_{cu} = -0.01047 *in./in.*	Type: ElasticPPGap f'_r = 2.05 *ksi* (14.2 *MPa*) E_c = 4030.5 *ksi* (27789.3 *MPa*)) ε_{su} = 0.1 *in./in.* Initial Gap = -0.01047 *in./in.*
Confined Concrete fibers: Column ID RC-AR4-ALI5-D7	
Type: Concrete 04 f'_{cc} = -9.45 *ksi* (65.16 *MPa*) ε_{cc} = -0.00605 *in./in.* f'_{cu} = -9.10 *psi* (62.74 *MPa*) ε_{cu} = -0.01646 *in./in.*	Type: ElasticPPGap f'_r = 2.05 *ksi* (14.2 *MPa*) E_c = 4030.5 *ksi* (27789.3 *MPa*)) ε_{su} = 0.1 *in./in.* Initial Gap = -0.01646 *in./in.*

5.3.2. Analytical Results

Figures 5-8 to 5-10 show the pushover relationship for the three bridge columns and Table 5-12 presents a summary of the results. The column failure was identified as a displacement in which the core concrete fails, the reinforcement factures, or the lateral load-carrying strength drops 20% with respect to the peak. The displacement ductility capacity was calculated based on AASHTO method (AASHTO Seismic Guide Specification, 2014). It can be seen that the displacement ductility capacity of the low-ductile column was doubled when a rubber jacket was used (increased from 3 to 6). This is because core concrete failure will be eliminated when concrete is confined with rubber. Columns with high ductilities will also benefit from rubber jacketing. However, the effect is not as profound as the low-ductile columns mainly because their core is already well-confined with steel.

Overall, the analytical studies showed that the proposed confinement method is a viable technique to retrofit, rehabilitate, or repair bridge columns with low ductilities. This method includes spraying rubber onsite, which can be easily done with minimal onsite activities.

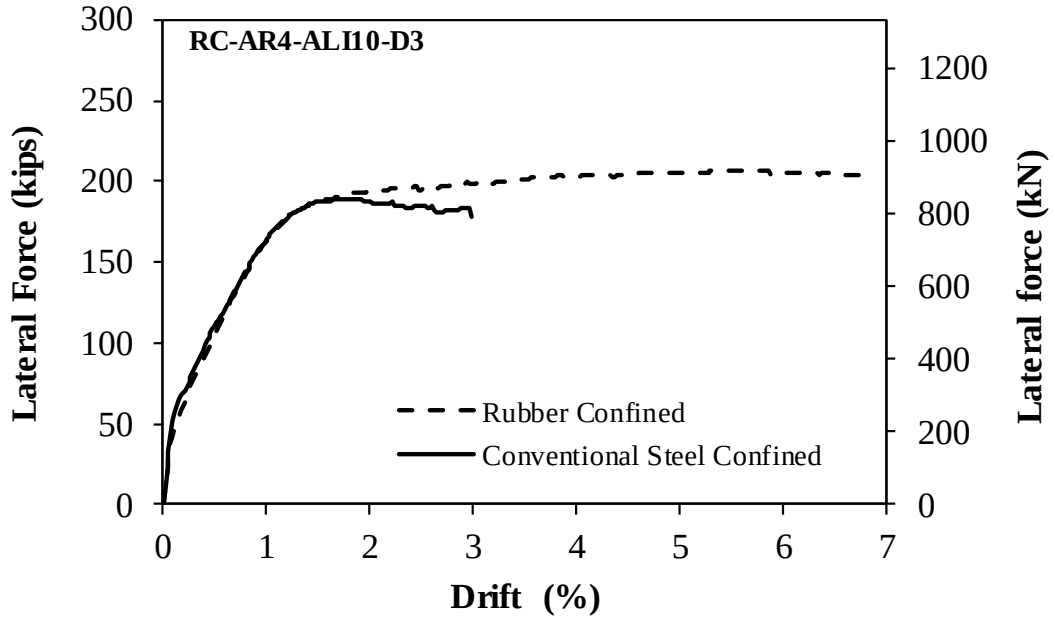

Figure 5-8. Force-displacement relationship of low ductile bridge column ($\mu = 3$)

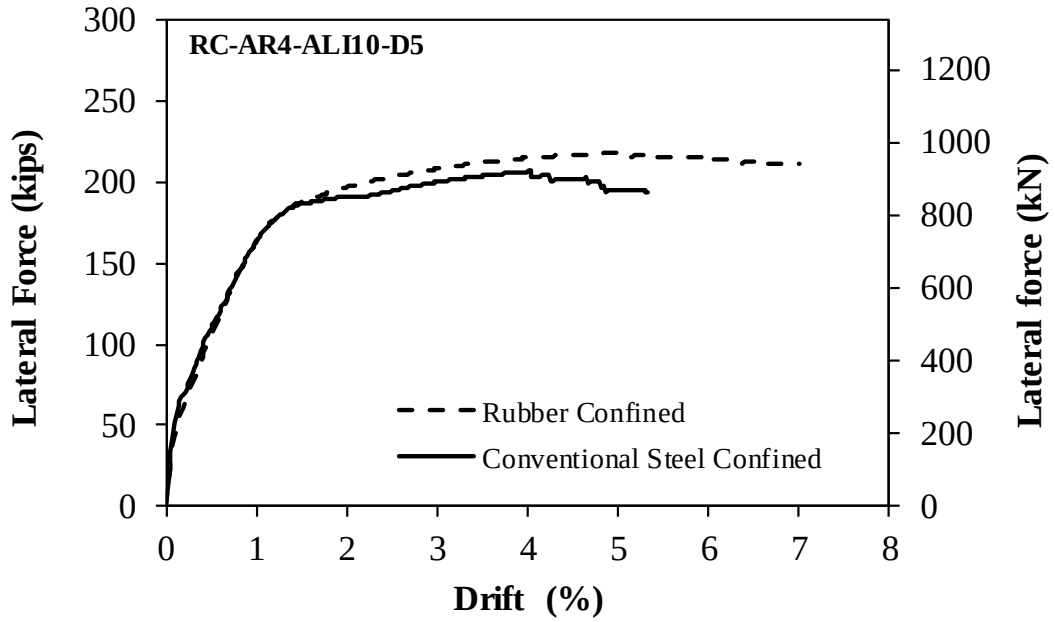

Figure 5-9. Force-displacement relationship of moderate ductile bridge column ($\mu = 5$)

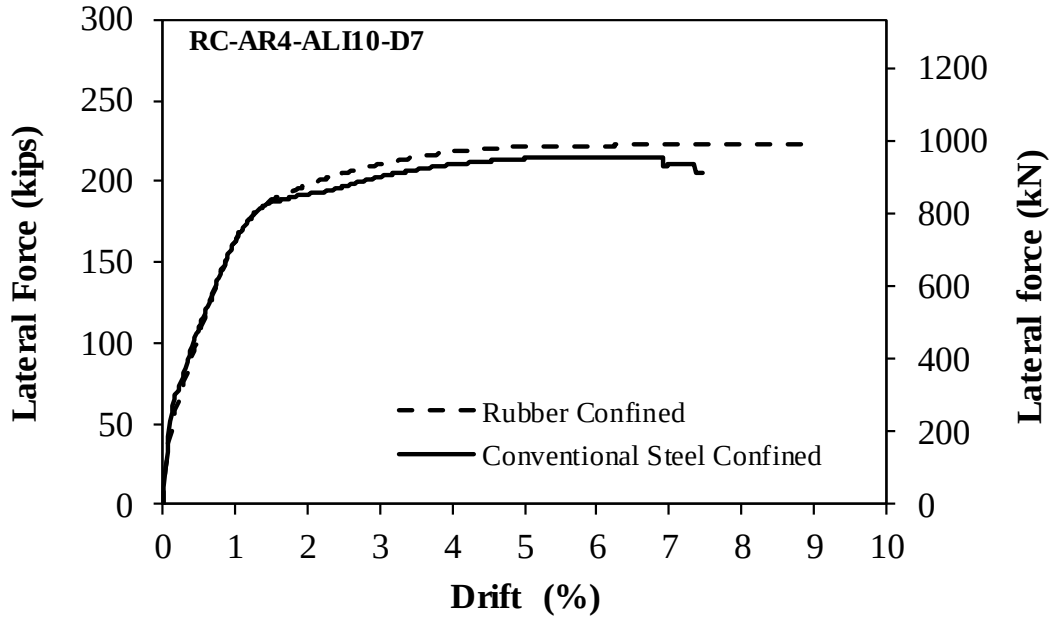

Figure 5-10. Force-displacement relationship of high ductile bridge column ($\mu = 7$)

Table 5.12. Displacement ductility capacity of bridge columns with and without rubber confinement

Column ID	Conventional Steel-Confined	Rubber confinement
RC-AR4-ALI5-D3	3.08	6.05
RC-AR4-ALI5-D5	4.98	5.98
RC-AR4-ALI5-D7	7.05	7.44

5.5. References

1. AASHTO. (2014). “AASHTO Guide Specifications for LRFD Seismic Bridge Design,” Washington, DC: American Association of State Highway and Transportation Officials.
2. Mander, J., Priestley, M., and Park, R. (1988). "Observed stress-strain behavior of confined concrete," Journal of structural engineering, 114(8), 1827-1849.
3. OpenSees. (2013). “Open System for Earthquake Engineering Simulations,” Version 2.4.1, Berkeley, CA, Available online: http://opensees.berkeley.edu.

4. Tazarv, M. and Saiidi, M.S. (2016). “Seismic Design of Bridge Columns Incorporating Mechanical Bar Splices in Plastic Hinge Regions,” Engineering Structures, DOI: 10.1016/j.engstruct.2016.06.041, Vol. 124, pp. 507-520.

CHAPTER 6. SUMMARY AND CONCLUSIONS

6.1. Summary

The main objective of the present study was to investigate the feasibility of new materials and innovative detailing for concrete structures. Three different topics were included in this study.

First, the use of rubber as external jackets for concrete to increase the ductility was proposed. Eighteen rubber confined concrete cylinders and 12 conventional concrete cylinders were prepared and tested under uniaxial compressive loads. Ready mix concrete with a target strength of 5000 *psi* was used in this experiment. Non-linear and simplified stress-strain models were developed for rubber confined concrete based on the measured data. The stress-strain relationship of the rubber confined concrete was compared with other types of confinement and materials such as steel-confined concrete, FRP-confined concrete, and steel-confined Engineered Cementitious Composite (ECC). Finally, the seismic performance of bridge columns confined with steel or rubber was investigated.

In the second study, conventional deformed steel bars without any reduction of the section area enclosed in steel pipes were experimentally investigated as external energy dissipaters. This type of external energy dissipater, entitled as buckling

restrained reinforcement (BRR), was also new. Nine BRR were tested to investigate their compressive behavior and anti-buckling efficiency. ASTM A706 Grade 60 deformed steel bars were used in BRR. Two different diameters and various lengths were included to optimize the performance of BRR. Grade 1026, carbon steel tube with different tube diameters and wall thicknesses were used as confining tubes. Non-shrink grout was used as filler material. A self-reacting setup was design to for testing of BRR. Load cells were used to capture the compressive loads and String POTs were used to measure the displacements. Both monotonic and cyclic loading were applied.

The seismic performance of a modern beam-column specimen including actual boundary conditions was experimentally investigated in the third part of this thesis. A nine-story special moment-resisting reinforced concrete office building was design according to current specifications to serve as prototype model. One of the building exterior beam-column joint was selected for experimental study. The RC frame was design as special moment resisting frame (SMRF). ASCE 7-10 and ACI318-14 were used for the design of the building. SAP2000 was used as design software. A half- model of the prototype beam-column specimen was tested under cyclic loading. ASTM A706 Grade 60 deformed reinforcing bars were used as longitudinal reinforcement for the beam and column. ASTM A706 Grade 60 deformed reinforcing bars also used as transverse reinforcement of the column. However, ASTM A496 deformed wires were used as transverse reinforcement in the beam. Confinement of the half-scale beam-column specimen was matched with that of the prototype beam-column specimen. A new test setup was developed to simulate the actual boundary conditions of the beam-column specimens in which both column and beam were free to sway under lateral loads. An axial load was applied at the

column top during test using hydraulic jacks and post-tensioning rods pump. Several strain gauges, displacement measurement devices, and load cells were used to measure strains, displacements, rotations, curvature, and load. A 22-kip actuator was used to apply lateral displacement at the top of the column in horizontal direction. The specimen was tested under a cyclic loading protocol to failure. Analytical studies were also carried out by OpenSees to develop and validate the proposed analytical model.

6.2. Conclusions

6.2.1. Rubber Confined Concrete

Based on the experimental investigation and analytical studies, the following conclusions can be drawn:

- The peak stress and the strain corresponding to the peak stress of rubber confined concrete were approximately same as those of unconfined conventional concrete.
- The residual strength of rubber confined concrete was lower than other confining methods such as steel confinement or FRP-confined concrete. However, rubber confined concrete exhibits very large strain capacity exceeding the strain capacity of reinforcing steel bar in tension.
- The proposed material model for rubber confined concrete can accurately simulate this material behavior.
- Displacement ductility capacity of low-ductile bridge columns can be doubled using rubber as an external jacket.

6.2.2. Buckling Restrained Reinforcement (BRR)

The proposed detailing for BRR showed good anti-buckling behavior. The following conclusions can be drawn based on the experimental investigation:

- The axial gap between the tube and the support plays a significant role to control the compressive behavior of BRR.
- BRR exhibits a very large compressive strength before buckling when the axial gap is less than $0.5d_b$.
- The compressive strain at the peak stress can exceed 5% with the proposed BRR, which will be sufficient in most practical cases since the strain of compressive reinforcement in a concrete section is usually controlled by the core concrete strains.
- Short BRRs show larger compressive stresses and strain capacities with the same tube properties than longer BRRs.
- BRR with thicker tubes achieve higher stresses and strain capacities compared to thinner tubes.

6.2.3. Beam-Column Connection

The following conclusion can be made based on the experimental data:

- Column longitudinal and transverse reinforcement is not expected to yield under cyclic loading such as earthquake, and the column damage will be insignificant if they are designed based on the current code special moment resisting frames (SMRF) requirements.
- Almost all cracks were formed in the beam. The beam longitudinal reinforcing bars yielded then fractured at a high drift ratio. Therefore, beams

are weaker than columns in modern SMRFs ensuring achieving large displacement capacities.

- The maximum lateral force in the push and pull direction was 7.98 (35.5) and 12.63 *kips* (56.2 kN), respectively. The ultimate displacement of the beam-column specimen was 2.53 *in* (64.26 *mm*) at a lateral force of 12.63 *kips* (56.2 *kN*).
- The drift ratio of tested beam-column connection was 3.5% in the push direction and 3.59% in the pull direction. The test result showed that this joint had 75% higher capacity in the push direction compared to the ASCE design guideline for buildings (ASCE 7-10, 2010) allowable drift ratio, which was 2% for this frame. Similarly, the joint shown 80% reserved drift capacity in the pull direction.
- The proposed analytical modeling method for the exterior beam-column joint showed a reasonable accuracy.